BOSTON UNIVERSITY

COLLEGE OF ENGINEERING

DISSERTATION

MODELING AND SIMULATION OF TRANSIENT ENHANCED DIFFUSION BASED ON INTERACTIONS OF POINT AND EXTENDED DEFECTS

by

ALP H. GENCER

B.S., Boğaziçi University, 1993
M.S., Boston University, 1995

Submitted in partial fulfillment of the
requirements for the degree of
Doctor of Philosophy
1999

ACKNOWLEDGEMENTS

First and foremost I would like to express my thanks to my professor, Prof. Scott Dunham, whose knowledge made this thesis possible in the first place. His deep knowledge in the field of process and device modeling, and his curiosity to learn more has always kept him and me at the cutting edge. Without his forward looking vision and strive for perfection this piece of work would not be as good as I liked it to be. I am also grateful to him to allow me to spend time with my family and work remotely when my life took a turn with the birth of my daughter.

I am also thankful to Prof. Theodore Moustakas for passing on his deep knowledge on semiconductor physics to me, for encouraging me to join BU, and supporting me with a teaching assistantship in my first year, for giving valuable suggestions as a member of my proposal and dissertation committee. I also would like to express my thanks to Prof. Daniel Cole, for serving on my dissertation committee and providing a long list of suggestions and corrections. Finally, I am also thankful to Prof. Karl Ludwig for bringing a physicist's aspect to this work.

During the years I spent at BU's Process Modeling Lab, I met several people. It was a great fun working with all of them. In particular, I would like to thank Anu Agarwal for her encouraging me to join the group, Soumya Banerjee and Mitra Navi for being great friends, and Srinivasan Chakravarthi and Brendon Murphy for working with me all the time. I also want to express my special thanks to Fred Wittel, who not only thought me how to be a great scientist and helped me in surviving my first year with the group, but also showed me how to be a good dad.

I also would like to express my thanks to my parents for providing me the education that made this thesis a reality. I am more than thankful to my parents-in-law, who provided constant support in every manner they could and put me through this work. Without their support, I would not find the courage, power and opportunity to complete my Ph.D. work.

Finally, I would like to express my love to my wife Ayşen and my daughter Aylin. Without them, I certainly wouldn't be the person who I am today.

MODELING AND SIMULATION OF TRANSIENT ENHANCED DIFFUSION BASED ON INTERACTIONS OF POINT AND EXTENDED DEFECTS

(Order No.   )

ALP H. GENCER

Boston University, College Of Engineering, 1999

Major Professor: Scott T. Dunham,

Professor of Electrical Engineering

ABSTRACT

As device sizes in VLSI technology get smaller, the importance of predictive process modeling increases. One of the biggest challenges in predictive process modeling today lies in modeling of Transient Enhanced Diffusion (TED). TED is the greatly enhanced diffusion of dopants in silicon seen during annealing of the damage created by the ion implantation of the dopants. As one moves to smaller thermal budgets, TED is often the primary source of diffusion and thus determines the final junction depth.

It is known that TED is caused by the excess interstitial concentration that persists due to ion implantation. But how this excess interstitial concentration evolves over time and affects the diffusion of dopants remains unclear. Our work attempts to understand the physical processes occurring during ion implant annealing, express them in a mathematical model, integrate this model into a diffusion equation solver and quantitatively match the experimental observations.

To this end, we have developed a solid physical model (KPM) for the evolution of extended defects ({311} defects and dislocation loops) which are observed under TED conditions. We have also developed different versions of KPM that have applicability under different circumstances, and have different levels of computational efficiency. We believe that the range of models developed will give the user the ability to make a compromise between accuracy and computational time.

We have applied KPM to {311} defects that are observed under non-amorphizing implant conditions and we were able to get a good agreement. We have then used this model to predict TED behavior based on marker layer experiments and we found a good match. To extend the model to dislocation loops, we assumed that dislocation loops form by unfaulting of {311} defects as observed experimentally. We accounted for this transformation in our model and we were able to obtain a good match to the experimental data without any modifications in the {311} defect model.

Our work also involved in developing a computer software that is capable of solving the models that we have postulated. To this end, we have developed DOPDEES, a one-dimensional multi purpose partial differential equation initial value solver. To enable faster technology transfer, we have also developed Process Modeling Modules (PMM) which consists a set of scripts that encapsulate the models that we have developed in a ready to use form.

Contents

List of Figures

Chapter 1

Understanding TED

1.1 Introduction

One of the most important challenges in VLSI technology today is to shrink device sizes to their limits, since both the speed and the yield (fraction of devices which work) increase as devices get smaller. However, as devices get smaller and junctions get shallower, some phenomena begin to get more and more important and the validity of current process simulators becomes questionable. Predictive process simulation plays a major roles in today's Technology CAD (TCAD), and hence, we need improvements in current process simulators.

As one tries to fabricate shallower junctions, one moves to smaller thermal budgets during processing with the hope of having less diffusion of dopants. But, one component of the diffusion, called Transient Enhanced Diffusion (TED), remains. TED is the greatly enhanced diffusion of dopants in silicon seen during annealing of the damage created by the ion implantation of the dopants. It is often the case that for today's processing parameters TED is the only significant component of diffusion. Thus, the need for accurate models that can account for the behavior seen during TED emerges.

Our work aims at obtaining a physical model that can be applied to the behavior of dopants under TED conditions. Although there are numerous articles on experimental observations concerning TED in the literature [2, 9, 29, 30, 31, 36, 40], little fundamental modeling has been done [13, 19, 34, 45]. Our work has the following unique features:

- Our work relies on a physical model of diffusion and interaction of dopant atoms and point defects, rather than on an empirical approach.

- The work is based on the evolution of the size distribution of extended defects during TED.

- It also includes deactivation of dopants and incorporation of point defects in dopant clusters or precipitates.

Having accounted for the primary physical processes that are occurring during TED, our goal was to arrive at a meaningful, and yet computationally efficient model that can be incorporated into a diffusion equation solver. It is noteworthy to mention that a physical model can be incorporated into any diffusion equation solver, since it is independent of the properties of the solver, like the number of dimensions.

1.2 Experimental data on TED

1.2.1 Early work on TED

Early work on TED concentrated on experimental observations, measuring the extent of TED. After the invention of rapid thermal annealing (RTA), first observations of TED were reported: even for very short times of annealing there was a considerable amount of dopant diffusion.

Most of the early papers [2, 36, 49] deal with dopant implants into silicon. A (high) dose of boron, phosphorus or arsenic was implanted into silicon, and after an RTA step the final profile was measured to determine the extent of TED. Angelucci *et al.* observed that boron and phosphorus show TED to a large extent, but arsenic shows little TED, and antimony shows almost no TED [3, 2]. To show this, Angelucci formed uniform layers of the dopants, patterned the sample, created a damage by silicon implantation and annealed at various times and temperatures. For B and P, the Si-implanted regions showed a large increase in junction depth, whereas for As and Sb, the difference was minimal.

The enhancement/retardation of diffusion during oxidation, nitridation and oxynitridation indicates that boron and phosphorus diffuse primarily via pairing with interstitials and antimony and arsenic diffuse primarily via pairing with vacancies [18]. It has been observed that boron and phosphorus show enhanced diffusion during oxidation, and during oxidation interstitial-type stacking faults grow. Therefore, oxidation must be injecting interstitials and boron and phosphorus must have an interstitial dominated diffusion mechanism. Similarly, antimony diffusion is enhanced during nitridation, but retarded during oxidation. Therefore antimony must be diffusing primarily via vacancies.

Combining the knowledge on primary diffusion mechanisms of individual dopants with the observations on TED for different dopants, we may conclude that TED is related to interstitial assisted diffusion. Indeed, after an ion implantation, there is a high super-saturation of interstitials due to the damage of the implant, and thus, this result is quite logical.

If we look at the time behavior of TED, we can observe that the enhancement is nearly independent of the ion-implant damage for initial times (Fig. 1.1); and after some period (duration of TED) the enhancement goes away [2, 39], such that we are left with normal diffusion which is many orders of magnitude smaller. This means that for early stages of TED the excess interstitial concentration is approximately fixed, and after some time it drops to its equilibrium value.

Another seemingly anomalous observation is that the amount of TED is larger at lower temperatures [36, 39], as demonstrated in Fig. 1.2. This can be explained in the following fashion: Although the diffusion of dopants is faster at higher temperatures, the duration of TED lasts shorter at higher temperatures, so that the overall junction movement gets smaller as the temperature is increased.

Hence, the following conclusions are in order:

- TED is caused by excess interstitial concentration that persists after ion implantation.

- The excess interstitial concentration remains approximately fixed during TED, and then drops to its equilibrium value.

- At higher temperatures the excess interstitial concentration disappears more rapidly, i.e. the duration of TED is shorter.

All of the above qualitative observations will help us to build our model.

2
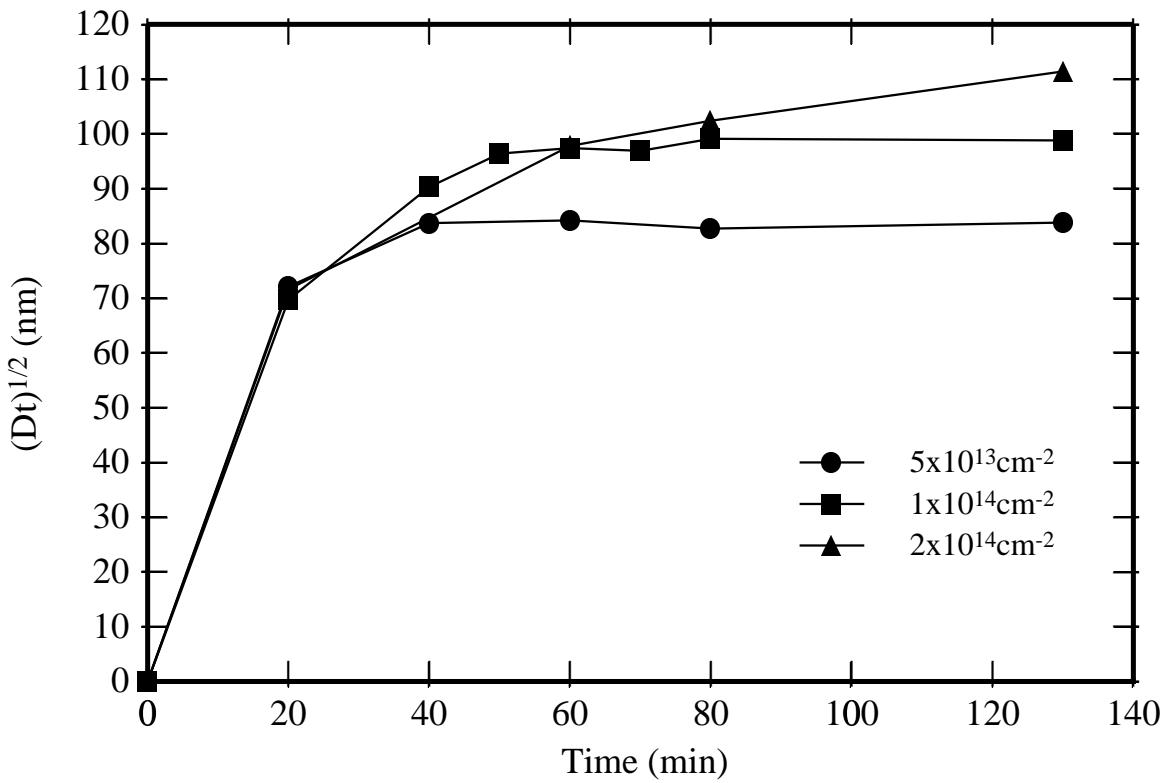
Figure 1.1: Time dependence of TED. Implantation of $5 \times 10^{13} - 2 \times 10^{14}\,\mathrm{cm}^{-2}$ Si at $200\,\mathrm{keV}$, and diffusion at $800°$C. Data from Packan [39].
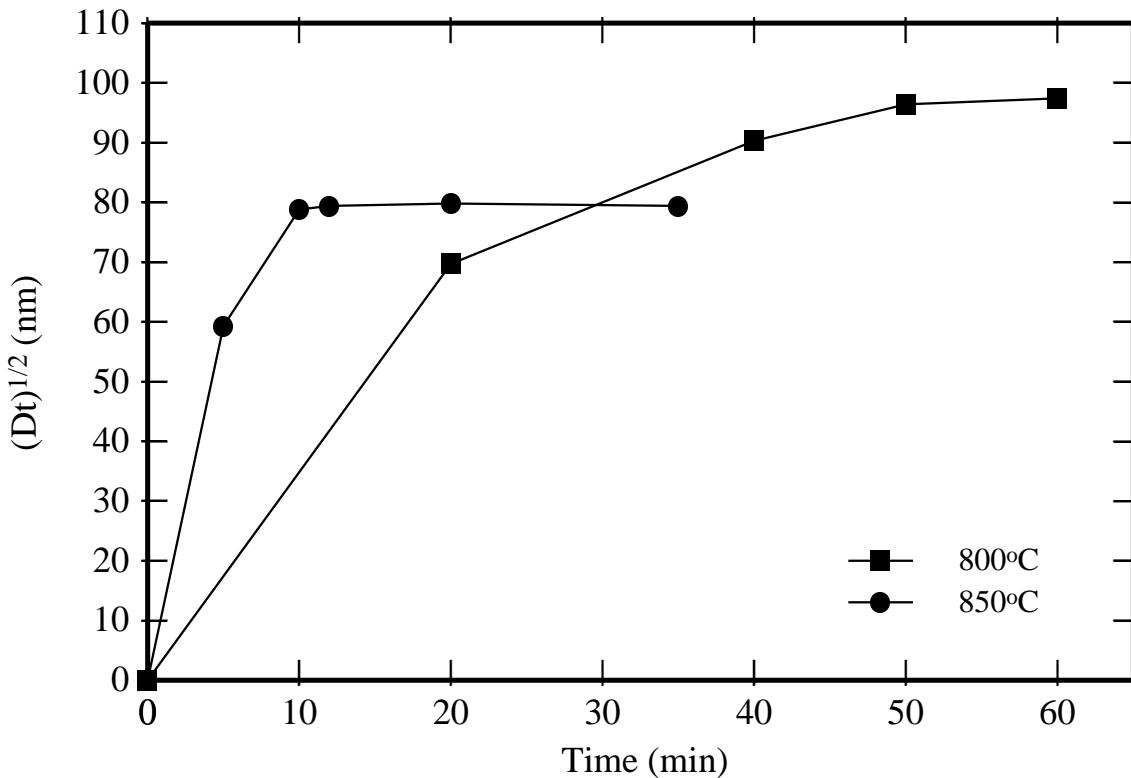
Figure 1.2: Temperature dependence of TED. Implantation of $1 \times 10^{14}\,\mathrm{cm}^{-2}$ Si at $200\,\mathrm{keV}$, and diffusion at $800°$Cand $850°$C. Data from Packan [39].
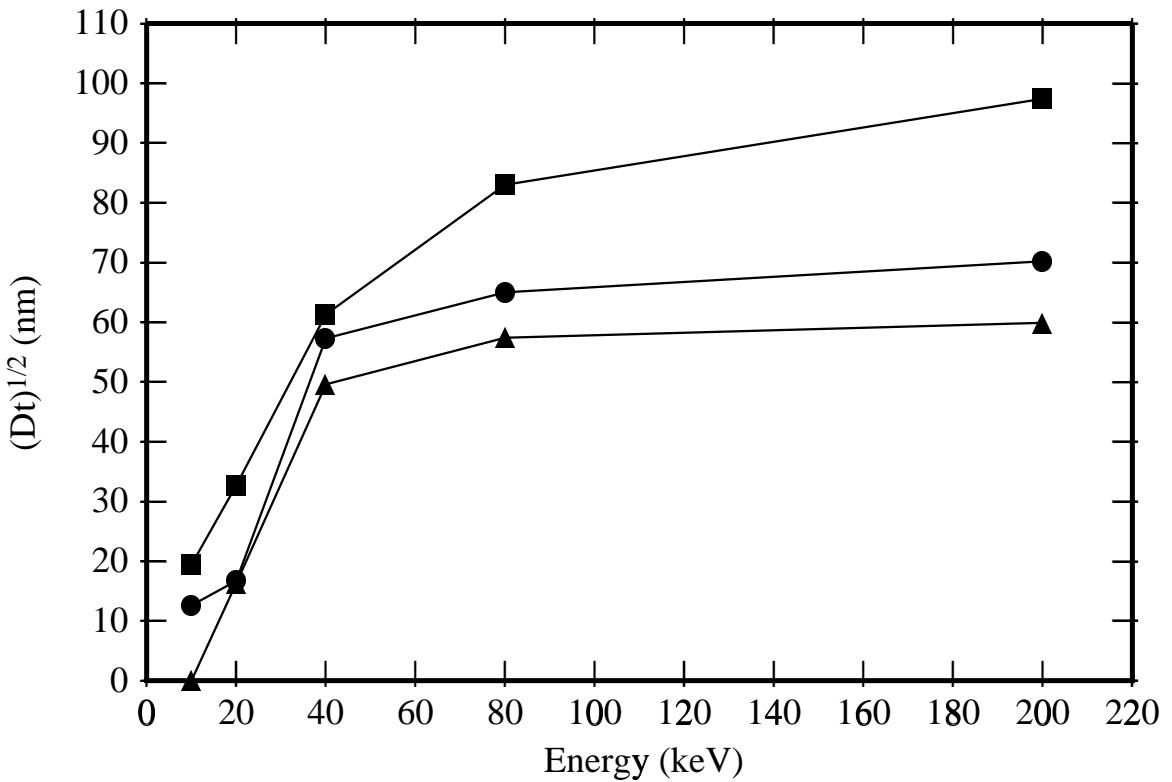
Figure 1.3: Energy dependence of TED. Implantation of $1 \times 10^{12}\,\text{cm}^{-2}$ Si at 10–200 keV, and diffusion at 800–1000°C. Data from Packan [39].

1.2.2 Separating the enhancement from the damage dose

In order to gain more insight into the mechanism of TED, experiments devoted to this topic have been done [30, 31, 40, 44]. Since in the experiments discussed in the previous section it was impossible to separate the enhancement from the damage dose, researchers designed experiments for this purpose. They put a tracer dose of the dopant (usually boron or phosphorus) deep into silicon. The damage is usually created by implanting silicon into the same sample. Thus, the damage dose is controlled independently from the dopant dose. This enables us to investigate regions where the material is intrinsic, and the dopant is far from its solid solubility limit.

Since amorphization and solid phase epitaxial regrowth is a complex process itself, experiments aimed at avoiding additional unknowns used implant doses below the amorphization threshold. The amorphization of silicon with silicon implants occurs usually at doses above $2 \times 10^{14}\,\text{cm}^{-2}$, which also depends on the implant energy.

The experiments confirm the results mentioned in the above subsections and add some more interesting aspects to the picture. First of all, the amount of TED increases with increasing silicon implant energy [39] (Fig. 1.3. This is a bit surprising, since, although the amount of total damage generated increases with implant energy, the net interstitial excess is nearly independent from the implant energy, only the position of the peak of damage depending on implant energy. Looking at the time behavior at different implant energies, we can conclude that the initial enhancement is about the same in all cases, only the duration of TED is longer for deeper implants [39].

The reason behind this observation is very simple if one assumes the primary sink for the excess
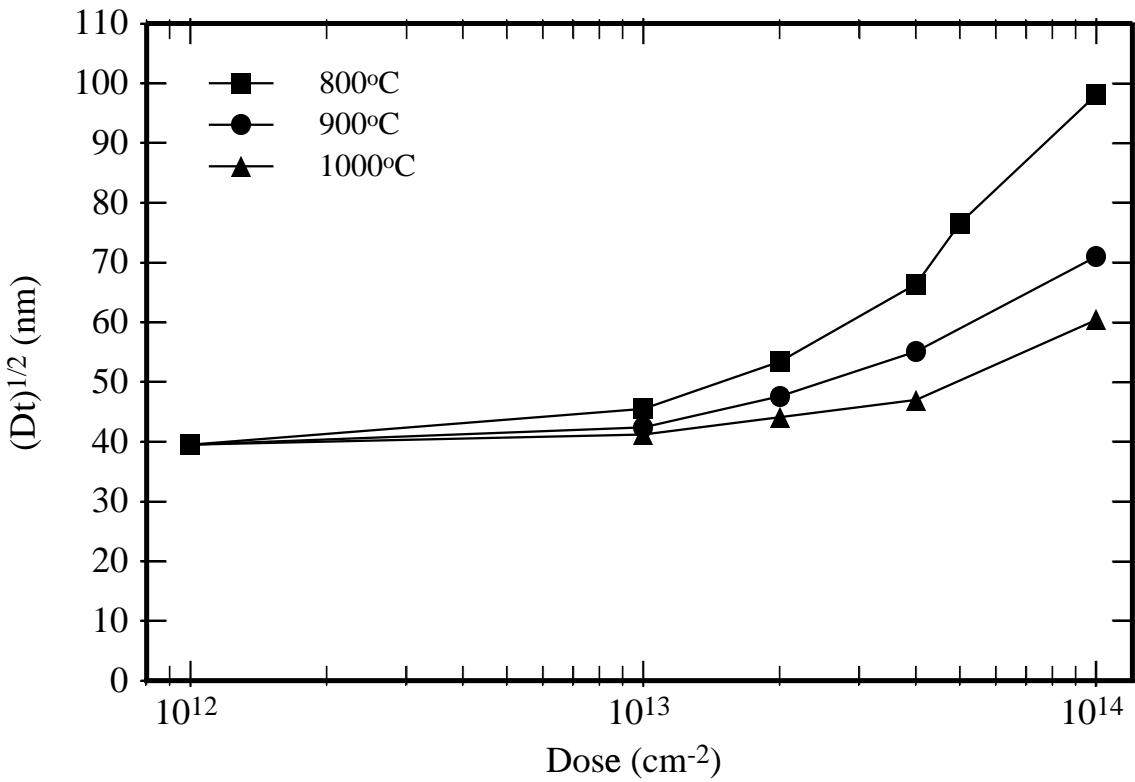
Figure 1.4: Dose dependence of TED. Implantation of $1 \times 10^{12} - 1 \times 10^{14}\,\mathrm{cm}^{-2}$ Si at $200\,\mathrm{keV}$, and diffusion at 800–$1000\,°\mathrm{C}$. Data from Packan [39].

interstitials to be the surface: The farther away the damage from the surface is, the harder it will be to get rid of it. Although interstitial-vacancy (I/V) recombination might play a role in being a sink for interstitials, other experiments indicate that it is fast, such that product of concentration of interstitials and concentration of vacancies ($C_I C_V$) drops to its equilibrium value in the very early stages of TED, which leaves us the surface as the primary sink.

One other interesting observation is that the dependence of TED on the silicon implant dose is non-linear [40] (Fig. 1.4). Even for silicon implant doses as low as $1 \times 10^{12}\,\mathrm{cm}^{-2}$ substantial dopant movement is observed. This behavior is one of the biggest challenges in TED and still no fully satisfactory explanation has been found.

Another observation is the fact that increasing the dopant implant dose decreases TED [31]. It might be expected that the dopants, too, are "using up" interstitials. It has been observed that a constant ratio of the marker layer dose to the damage dose gives an almost constant diffusion enhancement.

Hence, the following conclusions are in order:

- Higher energy damage implants result in more profile movement.

- Surface is the primary sink for excess interstitials.

- TED increases sub-linearly with increasing damage dose.

- TED decreases with increasing dopant maker layer dose.

1.2.3 The source of the interstitials

As mentioned in section 1.2.1, the excess interstitial concentration remains approximately fixed during TED, and then drops to its equilibrium value. This tells us that there must be a mechanism that stores the interstitials created by the implant damage and then releases them during TED, acting as a "source" of interstitials. In fact, if such a meta-stable state for interstitials didn't exist, they would rapidly diffuse to the surface and TED would be over in a very short time.

Recent experiments revealed the actual source of the interstitials during TED [10, 17]. Eaglesham *et al.* created the damage by implanting Si into Si and then annealed the samples at various temperatures. They then performed plan-view and cross sectional Transmission Electron Microscopy (TEM) on the samples. They clearly saw the defects that store excess interstitials.

These defects are the so-called "rod-like" or "{311}" defects. The atomic structure of {311} defects has been only recently resolved [50]. It is believed that interstitials form chains along <110> direction and these chains come together to form a {311} plane. This defect can get very long (about 1μm) in the <110> direction, hence is given the name "rod-like" defects.

The fact that the time needed for dissolution of {311} defects is equal to the duration of TED [17] is an excellent indicator that {311} defects are the source of the interstitials during TED.

1.2.4 Interactions involving dislocation loops and boron-interstitial clusters

Studies concentrating on formation and evolution of dislocation loops generated by Si implantation have been published [7, 35, 52]. It has been observed that the growth rate of dislocation loops is constant in time, as it would be predicted by a bulk-diffusion mechanism. A quantitative model, which predicts the loop evolution correctly, has also been developed [7].

Experiments by the same group also report interactions between {311} defects and dislocation loops [33]. Results clearly show that the distribution of trapped interstitials between {311} defects and dislocation loops is dependent on the implant dose. Interestingly, the amount of trapped interstitials in {311} defects seems to saturate around $2 \times 10^{13}\,\mathrm{cm}^{-2}$ at 700°C.

Implantation of boron into silicon at very low doses and energies produces no visible {311} defects, but substantial TED is observed [57]. The threshold for {311} formation is estimated to be $5 \times 10^{12}\,\mathrm{cm}^{-2}$ for silicon implants and $1 \times 10^{14}\,\mathrm{cm}^{-2}$ for boron implants. The question whether below these doses tiny interstitial clusters exist or not remains unanswered.

Recent observations by Cowern *et al.* [9, 10], suggest that in systems where B is present in large doses, excess interstitials help boron atoms to form boron clusters and are themselves incorporated into these clusters (so-called boron interstitial clusters, BICs), thereby reducing the number of mobile boron atoms. Although the BICs are not visible even with high resolution TEM, the diffusion profiles indicate that boron is becoming immobile where it is present at high doses.

Chapter 2

Models of Importance for TED

2.1 Coupled diffusion of dopants and point defects

Since TED is an immediate result of enhancement of dopant diffusion due to presence of point defects (mainly interstitials) in excess of their equilibrium values (i.e. existence of a point defect super-saturation), the first thing we will investigate is the effect of point defects on dopant diffusion. In this section, we present various diffusion models and discuss their applicability to TED. In the following equations, B represents our dopant, I represents interstitials and V represents vacancies. C denotes the concentration and D denotes the diffusivity of a certain species indicated by the subscript.

2.1.1 Fermi diffusion model

In the most simplistic view, dopant diffusion can be described by the "Fermi" diffusion model, in which the effect of point defects on dopant diffusion is completely ignored:

$$\frac{\partial C_{\mathrm{B}}}{\partial t} = \vec{\nabla} \cdot D_{\mathrm{B}} \vec{\nabla} C_{\mathrm{B}} \tag{2.1}$$

where D_{B} is a function of the Fermi level:

$$D_{\mathrm{B}} = D_{\mathrm{B}}^0 + D_{\mathrm{B}}^+ (p/n_i) + D_{\mathrm{B}}^- (n/n_i) \tag{2.2}$$

This model is only valid under equilibrium conditions when both interstitials and vacancies at their equilibrium levels. Obviously, TED is a total deviation from this assumption, so we can't use this model under TED conditions. However, diffusivity of dopants is determined using the "Fermi" model, so the parameters in the more sophisticated diffusion models should relate to D_{B} as defined above.

2.1.2 Pair diffusion with a single point defect

Dopants are known to be diffusing via pairing with point defects [18]. We want to build up the theory that leads to the pair diffusion of dopants. For this purpose we start by assuming the dopant diffuses

only via pair formation with interstitials:

$$B + I \Leftrightarrow BI \tag{2.3}$$

In this chemical reaction, the forward rate will be proportional to the $C_B C_I$ product, and the reverse rate will be proportional to C_{BI}. The net forward reaction rate can be written as:

$$k_{BI}(K_{BI}C_B C_I - C_{BI}) \tag{2.4}$$

where K_{BI} is the equilibrium constant and has units of cm^3 (inverse concentration). In equilibrium, C_{BI} will be equal to $K_{BI}C_B C_I$. The system results in the following continuity equations:

$$
\begin{aligned}
\frac{\partial C_B}{\partial t} &= -k_{BI}(K_{BI}C_B C_I - C_{BI}) \\
\frac{\partial C_I}{\partial t} &= \vec{\nabla} \cdot D_I \vec{\nabla} C_I - k_{BI}(K_{BI}C_B C_I - C_{BI}) \\
\frac{\partial C_{BI}}{\partial t} &= \vec{\nabla} \cdot D_{BI} \vec{\nabla} C_{BI} + k_{BI}(K_{BI}C_B C_I - C_{BI})
\end{aligned}
\tag{2.5}
$$

If we assume that pairing is fast (that is k_{BI} is very large), then the pairing reaction will always be in equilibrium, and we can reduce the continuity equations to two by eliminating the terms associated with this reaction:

$$
\begin{aligned}
\frac{\partial (C_B + C_{BI})}{\partial t} &= \vec{\nabla} \cdot D_{BI} \vec{\nabla} C_{BI} \\
\frac{\partial (C_I + C_{BI})}{\partial t} &= \vec{\nabla} \cdot D_I \vec{\nabla} C_I + \vec{\nabla} \cdot D_{BI} \vec{\nabla} C_{BI}
\end{aligned}
\tag{2.6}
$$

with $C_{BI} = K_{BI}C_B C_I$. Note that $C_B + C_{BI} = C_B^T$, the total concentration of our dopant in silicon. This is the value reported by Secondary Ion Mass Spectrometry (SIMS). Similarly $C_I + C_{BI} = C_I^T$, the total interstitial concentration. If we assume that $C_{BI} \ll C_B$ and $C_{BI} \ll C_I$, then $C_B \approx C_B^T$ and $C_I \approx C_I^T$. This approximations will be valid under equilibrium and oxidation enhanced diffusion (OED) conditions. We can then eliminate C_{BI} from the above equations:

$$
\begin{aligned}
\frac{\partial C_B}{\partial t} &= \vec{\nabla} \cdot D_{BI} \vec{\nabla} (K_{BI}C_B C_I) \\
\frac{\partial C_I}{\partial t} &= \vec{\nabla} \cdot D_I \vec{\nabla} C_I + \vec{\nabla} \cdot D_{BI} \vec{\nabla} (K_{BI}C_B C_I)
\end{aligned}
\tag{2.7}
$$

which can be modified into:

$$
\begin{aligned}
\frac{\partial C_B}{\partial t} &= \vec{\nabla} \cdot D_{BI}K_{BI}C_I^* \vec{\nabla} \left(C_B \frac{C_I}{C_I^*} \right) \\
\frac{\partial C_I}{\partial t} &= \vec{\nabla} \cdot D_I \vec{\nabla} C_I + \vec{\nabla} \cdot D_{BI}K_{BI}C_I^* \vec{\nabla} \left(C_B \frac{C_I}{C_I^*} \right)
\end{aligned}
\tag{2.8}
$$

If $C_I = C_I^*$, then the diffusivity of the dopant should be equal to D_B in the "Fermi" model. Thus we can say that $D_B = D_{BI}K_{BI}C_I^*$.

$$
\begin{aligned}
\frac{\partial C_B}{\partial t} &= \vec{\nabla} \cdot \frac{D_B}{C_I^*} \vec{\nabla} (C_B C_I) \\
\frac{\partial C_I}{\partial t} &= \vec{\nabla} \cdot D_I \vec{\nabla} C_I + \vec{\nabla} \cdot \frac{D_B}{C_I^*} \vec{\nabla} (C_B C_I)
\end{aligned}
\tag{2.9}
$$

8

It is evident that the dopant will diffuse not only because there is a gradient in C_B, but also because there is a gradient in C_I and vice versa.

2.1.3 Pair diffusion with both point defects

If we assume that the dopant can pair both with vacancies and interstitials, we can write two possible groups of reactions. In each case the rightmost column gives the net forward rate of the reactions. First, we have dopant/point defect pairing reactions:

$$
\begin{array}{rcll}
B+I & \Leftrightarrow & BI & k_{BI}(K_{BI}C_BC_I - C_{BI}) \\
B+V & \Leftrightarrow & BV & k_{BV}(K_{BV}C_BC_V - C_{BV})
\end{array}
\tag{2.10}
$$
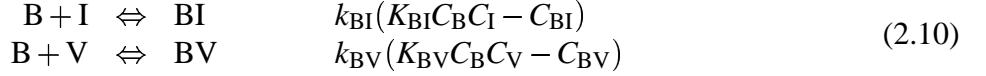
And then we have the direct and indirect recombination reactions:

$$
\begin{array}{rcll}
I+V & \Leftrightarrow & \emptyset & k_R(C_IC_V - C_I^*C_V^*) \\
BI+V & \Leftrightarrow & B & k_R(C_{BI}C_V - K_{BI}C_BC_I^*C_V^*) \\
BV+I & \Leftrightarrow & B & k_R(C_{BV}C_I - K_{BV}C_BC_I^*C_V^*) \\
BI+BV & \Leftrightarrow & 2B & k_R(C_{BI}C_{BV} - K_{BI}K_{BV}C_B^2C_I^*C_V^*)
\end{array}
\tag{2.11}
$$
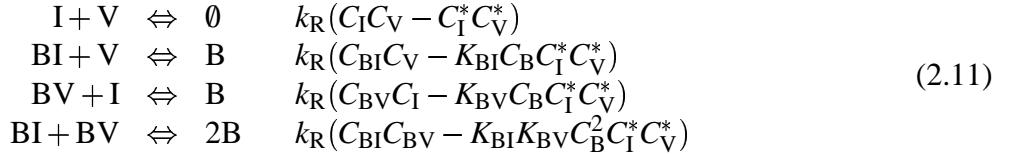
Note that the rate constant for each of the recombination reactions is assumed to be k_R, which is a simplification. In fact, if we assume diffusion limited processes, the reaction rates for the four reactions should be $4\pi a(D_I+D_V)$, $4\pi a(D_{BI}+D_V)$, $4\pi a(D_I+D_{BV})$ and $4\pi a(D_{BI}+D_{BV})$, respectively. For the purposes of this reaction set, we can assume that $D_{BI} = D_I$ and $D_{BV} = D_V$. This is not a bad assumption since both point defects and pairs are fast diffusers. This assumption makes all the four rates equal.

If we assume that pairing is fast, so that $C_{BI} = K_{BI}C_BC_I$ and $C_{BV} = K_{BV}C_BC_V$, we may combine the recombination reactions into a single, effective one. Note that none of the recombination reactions will effect total dopant concentration (C_B^T):

$$
\begin{array}{rcl}
k_R(C_IC_V - C_I^*C_V^*) & = & k_R(C_IC_V - C_I^*C_V^*) \\
k_R(C_{BI}C_V - K_{BI}C_BC_I^*C_V^*) & = & k_RK_{BI}C_B(C_IC_V - C_I^*C_V^*) \\
k_R(C_{BV}C_I - K_{BV}C_BC_I^*C_V^*) & = & k_RK_{BV}C_B(C_IC_V - C_I^*C_V^*) \\
k_R(C_{BI}C_{BV} - K_{BI}K_{BV}C_B^2C_I^*C_V^*) & = & k_RK_{BI}K_{BV}C_B^2(C_IC_V - C_I^*C_V^*)
\end{array}
\tag{2.12}
$$

which gives:

$$
k_R^{\text{eff}} = k_R(1 + K_{BI}C_B)(1 + K_{BV}C_B)
\tag{2.13}
$$

The continuity equations reduce to:

$$
\begin{array}{rcl}
\dfrac{\partial(C_B + C_{BI} + C_{BV})}{\partial t} & = & \vec{\nabla} \cdot D_{BI}\vec{\nabla}C_{BI} + \vec{\nabla} \cdot D_{BV}\vec{\nabla}C_{BV} \\[2ex]
\dfrac{\partial(C_I + C_{BI})}{\partial t} & = & \vec{\nabla} \cdot D_I\vec{\nabla}C_I + \vec{\nabla} \cdot D_{BI}\vec{\nabla}C_{BI} - k_R^{\text{eff}}(C_IC_V - C_I^*C_V^*) \\[2ex]
\dfrac{\partial(C_V + C_{BV})}{\partial t} & = & \vec{\nabla} \cdot D_V\vec{\nabla}C_V + \vec{\nabla} \cdot D_{BV}\vec{\nabla}C_{BV} - k_R^{\text{eff}}(C_IC_V - C_I^*C_V^*)
\end{array}
\tag{2.14}
$$

with $C_{BI} = K_{BI}C_BC_I$ and $C_{BV} = K_{BV}C_BC_V$. We can denote the diffusivity of the dopant atom due to the interstitialcy mechanism under equilibrium conditions ($C_I = C_I^*$) by D_B^I. Similarly, diffusivity of the

9

dopant due to the vacancy mechanism when $C_V = C_{V*}$ can be denoted by D_B^V. Note that $D_B^I + D_B^V = D_B$, the total diffusivity of the dopant under equilibrium conditions. This gives the following set of continuity equations:

$$
\begin{aligned}
\frac{\partial C_B^T}{\partial t} &= \vec{\nabla} \cdot D_B^I \vec{\nabla} \left(C_B \frac{C_I}{C_I^*} \right) + \vec{\nabla} \cdot D_B^V \vec{\nabla} \left(C_B \frac{C_V}{C_V^*} \right) \\
\frac{\partial C_I^T}{\partial t} &= \vec{\nabla} \cdot D_I \vec{\nabla} C_I + \vec{\nabla} \cdot D_B^I \vec{\nabla} \left(C_B \frac{C_I}{C_I^*} \right) - k_R^{\text{eff}} (C_I C_V - C_I^* C_V^*) \\
\frac{\partial C_V^T}{\partial t} &= \vec{\nabla} \cdot D_V \vec{\nabla} C_V + \vec{\nabla} \cdot D_B^V \vec{\nabla} \left(C_B \frac{C_V}{C_V^*} \right) - k_R^{\text{eff}} (C_I C_V - C_I^* C_V^*)
\end{aligned}
\tag{2.15}
$$

2.1.4 Pair diffusion with a single point defect, including Fermi level effects

The preceding set of of equations ignored the dependence of dopant diffusivity on Fermi level. This dependence stems from the fact that the number of point defects available for diffusion changes with the Fermi level. We assume that interstitials can be neutral, positively or negatively charged. We assume that the charging reactions are much faster than pairing reactions, since they are electronic reactions and the mobility of electrons is much larger than the mobility of dopants. Therefore, the electronic reactions are always close to equilibrium:

$$
\begin{array}{llll}
e^- + e^+ & \Leftrightarrow & \emptyset & \quad np = n_i^2 \\
I^0 + e^- & \Leftrightarrow & I^- & \quad C_{I^-} = K_{I^-} C_{I^0} (n/n_i) \\
I^0 + e^+ & \Leftrightarrow & I^+ & \quad C_{I^+} = K_{I^+} C_{I^0} (p/n_i)
\end{array}
\tag{2.16}
$$
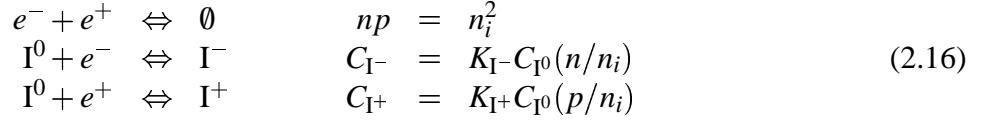
Each of these charged interstitials can pair with dopants. Again, we assume that pairing is in equilibrium:

$$
\begin{array}{llll}
B^- + I^0 & \Leftrightarrow & BI^0 & \quad C_{BI^0} = K_{BI^0} C_B C_{I^0} \\
B^- + I^+ & \Leftrightarrow & BI^+ & \quad C_{BI^+} = K_{BI^+} C_B (K_{I^+} C_{I^0} (p/n_i)) \\
B^- - I^- & \Leftrightarrow & BI^- & \quad C_{BI^-} = K_{BI^-} C_B (K_{I^-} C_{I^0} (n/n_i))
\end{array}
\tag{2.17}
$$
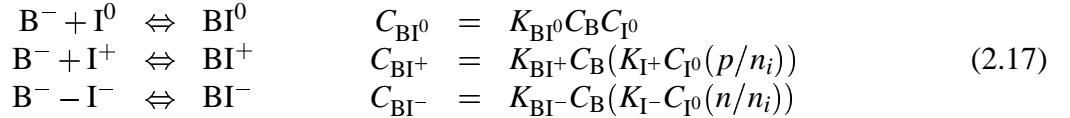
The notation above may be confusing, but is laid out as follows: C_{BI^0} is the concentration of the resulting pair from the reaction of an ionized dopant and I^0. If the dopant is an acceptor, it will carry a net negative charge in its ionized state, making BI^0 negatively charged. If the dopant is a donor, it will carry a net positive charge in its ionized state, making BI^0 positively charged.

Note the dopant is an acceptor (carrying a negative charge) it is very unlikely that it will pair with a negatively charged interstitial due to repulsion, making $C_{BI^-} = 0$. A similar statement is true for donors. But we keep the C_{BI^-} term to make the analysis more general and assume that $K_{BI^-} = 0$ for acceptors and that $K_{BI^+} = 0$ for donors.

Note that due to the charge of ions, the continuity equation will not only have a diffusion component ($\vec{J}^{\text{diff}}$), but also a drift component ($\vec{J}^{\text{drift}}$). The drift terms arise because the charged species can also move because of forces of the electric field, created by the gradient of electron concentration in the substrate. The total flux of point defects and pairs will be equal to the sum of fluxes of each charge state:

$$\frac{\partial C_{\mathrm{B}}^{T}}{\partial t} = -\vec{\nabla} \cdot \sum_{i=-1}^{+1} (\vec{J}_{\mathrm{BI}^i}^{\mathrm{diff}} + \vec{J}_{\mathrm{BI}^i}^{\mathrm{drift}}) \tag{2.18}$$

$$\frac{\partial C_{\mathrm{I}}^{T}}{\partial t} = -\vec{\nabla} \cdot \sum_{i=-1}^{+1} (\vec{J}_{\mathrm{I}^i}^{\mathrm{diff}} + \vec{J}_{\mathrm{I}^i}^{\mathrm{drift}}) - \vec{\nabla} \cdot \sum_{i=-1}^{+1} (\vec{J}_{\mathrm{BI}^i}^{\mathrm{diff}} + \vec{J}_{\mathrm{BI}^i}^{\mathrm{drift}})$$

Next we do the generic derivation of $\vec{J}_{\mathrm{BI}^i}^{\mathrm{diff}} + \vec{J}_{\mathrm{BI}^i}^{\mathrm{drift}}$. Assume that the dopant is an acceptor, and hence carries a charge of $-q$. If the dopant was a donor, it would carry a charge of $+q$. This will make the charge on a BI^i pair $(i+z)q$, where $z = +1$ if the dopant is a donor and $z = -1$ if the dopant is an acceptor. Then, we can write the diffusion term as:

$$
\begin{aligned}
\vec{J}_{\mathrm{BI}^i}^{\mathrm{diff}} &= -D_{\mathrm{BI}^i}\vec{\nabla}C_{\mathrm{BI}^i}\\
&= -D_{\mathrm{BI}^i}\vec{\nabla}(K_{\mathrm{BI}^i}C_{\mathrm{B}}(K_{\mathrm{I}^i}C_{\mathrm{I}^0}(p/n_i)^i))\\
&= -D_{\mathrm{BI}^i}K_{\mathrm{BI}^i}K_{\mathrm{I}^i}\vec{\nabla}(C_{\mathrm{B}}C_{\mathrm{I}^0}(p/n_i)^i)\\
&= -D_{\mathrm{B}}^i/C_{\mathrm{I}^0}^*\left[(p/n_i)^i\vec{\nabla}(C_{\mathrm{B}}C_{\mathrm{I}^0}) + C_{\mathrm{B}}C_{\mathrm{I}^0}\vec{\nabla}(p/n_i)^i\right]\\
&= -D_{\mathrm{B}}^i/C_{\mathrm{I}^0}^*\left[(p/n_i)^i\vec{\nabla}(C_{\mathrm{B}}C_{\mathrm{I}^0}) + C_{\mathrm{B}}C_{\mathrm{I}^0}i(p/n_i)^{i-1}\vec{\nabla}(p/n_i)\right] \tag{2.19}
\end{aligned}
$$

And the drift term becomes:

$$
\begin{aligned}
\vec{J}_{\mathrm{BI}^i}^{\mathrm{drift}} &= \mu_{\mathrm{BI}^i}(i+z)q\vec{\mathcal{E}}C_{\mathrm{BI}^i}\\
&= D_{\mathrm{BI}^i}(q/kT)(i+z)\vec{\mathcal{E}}C_{\mathrm{BI}^i} \tag{2.20}
\end{aligned}
$$

where $\mu = D/kT$ is the mobility according to the Einstein relationship and $\vec{\mathcal{E}}$ is the electric field vector. The electric field can be calculated from the gradient of the potential, which in turn can be found from the local carrier concentration, given by a Boltzmann distribution (Ψ denotes the intrinsic potential):

$$n = n_i \exp\left(\frac{\Psi}{kT/q}\right) \tag{2.21}$$

$$
\begin{aligned}
\vec{\mathcal{E}} &= -\vec{\nabla}\Psi\\
&= -\vec{\nabla}(kT/q\ln(n/n_i))\\
&= \vec{\nabla}(kT/q\ln(p/n_i)) \tag{2.22}
\end{aligned}
$$

$$
\begin{aligned}
\vec{J}_{\mathrm{BI}^i}^{\mathrm{drift}} &= D_{\mathrm{BI}^i}(i-1)C_{\mathrm{BI}^i}\vec{\nabla}\ln(p/n_i)\\
&= D_{\mathrm{BI}^i}(i-1)(K_{\mathrm{BI}^i}C_{\mathrm{B}}(K_{\mathrm{I}^i}C_{\mathrm{I}^0}(p/n_i)^i))(n_i/[)\vec{\nabla}([/n_i)\\
&= D_{\mathrm{BI}^i}K_{\mathrm{BI}^i}K_{\mathrm{I}^i}(i-1)C_{\mathrm{B}}C_{\mathrm{I}^0}(p/n_i)^{i-1}\vec{\nabla}(p/n_i)\\
&= D_{\mathrm{B}}^i/C_{\mathrm{I}^0}^*(i-1)C_{\mathrm{B}}C_{\mathrm{I}^0}(p/n_i)^{i-1}\vec{\nabla}(p/n_i) \tag{2.23}
\end{aligned}
$$

Adding the diffusion and drift terms we get:

$$\vec{J}_{\mathrm{BI}^i} = -D_{\mathrm{B}}^i/C_{\mathrm{I}^0}^* \left[(p/n_i)^i \vec{\nabla}(C_{\mathrm{B}}C_{\mathrm{I}^0}) + C_{\mathrm{B}}C_{\mathrm{I}^0}(p/n_i)^{i-1}\vec{\nabla}(p/n_i) \right]$$

$$= -D_{\mathrm{B}}^i/C_{\mathrm{I}^0}^*(p/n_i)^i \left[\vec{\nabla}(C_{\mathrm{B}}C_{\mathrm{I}^0}) + C_{\mathrm{B}}C_{\mathrm{I}^0}\vec{\nabla}\ln(p/n_i) \right] \tag{2.24}$$

Summing over all the charge states, we will get:

$$\vec{J}_{\mathrm{BI}} = \sum_{i=-1}^{+1} \vec{J}_{\mathrm{BI}^i} = -\frac{(D_{\mathrm{B}}^0 + D_{\mathrm{B}}^+(p/n_i) + D_{\mathrm{B}}^-(n/n_i))}{C_{\mathrm{I}^0}^*} \left[\vec{\nabla}(C_{\mathrm{B}}C_{\mathrm{I}^0}) + C_{\mathrm{B}}C_{\mathrm{I}^0}\vec{\nabla}\ln(p/n_i) \right] \tag{2.25}$$

For donors, we need to replace $\ln(p/n_i)$ with $\ln(n/n_i)$. It may readily be observed that under equilibrium conditions ($C_{\mathrm{I}^0} = C_{\mathrm{I}^0}^*$), this reduces to "Fermi model" (Eq. 2.1).

If we carry out a similar analysis for $\vec{J}_{\mathrm{I}^i}$ we can see that the term with the gradient of (p/n_i) is being canceled by the drift term:

$$\vec{J}_{\mathrm{I}^i}^{\mathrm{diff}} = -D_{\mathrm{I}^i}\vec{\nabla}C_{\mathrm{I}^i}$$

$$= -D_{\mathrm{I}^i}\vec{\nabla}(K_{\mathrm{I}^i}C_{\mathrm{I}^0}(p/n_i)^i)$$

$$= -D_{\mathrm{I}^i}K_{\mathrm{I}^i}\vec{\nabla}(C_{\mathrm{I}^0}(p/n_i)^i)$$

$$= -D_{\mathrm{I}^i}K_{\mathrm{I}^i}\left[(p/n_i)^i\vec{\nabla}C_{\mathrm{I}^0} + C_{\mathrm{I}^0}\vec{\nabla}(p/n_i)^i \right]$$

$$= -D_{\mathrm{I}^i}K_{\mathrm{I}^i}\left[(p/n_i)^i\vec{\nabla}C_{\mathrm{I}^0} + C_{\mathrm{I}^0}i(p/n_i)^{i-1}\vec{\nabla}(p/n_i) \right] \tag{2.26}$$

$$\vec{J}_{\mathrm{I}^i}^{\mathrm{drift}} = D_{\mathrm{I}^i}(q/kT)i\vec{E}C_{\mathrm{I}^i}$$

$$= D_{\mathrm{I}^i}iC_{\mathrm{I}^i}\vec{\nabla}\ln(p/n_i)$$

$$= D_{\mathrm{I}^i}i(K_{\mathrm{I}^i}C_{\mathrm{I}^0}(p/n_i)^i)(n_i/p)\vec{\nabla}(p/n_i)$$

$$= D_{\mathrm{I}^i}K_{\mathrm{I}^i}iC_{\mathrm{I}^0}(p/n_i)^{i-1}\vec{\nabla}(p/n_i) \tag{2.27}$$

$$\vec{J}_{\mathrm{I}^i} = \vec{J}_{\mathrm{I}^i}^{\mathrm{diff}} + \vec{J}_{\mathrm{I}^i}^{\mathrm{drift}} = -D_{\mathrm{I}^i}K_{\mathrm{I}^i}(p/n_i)^i\vec{\nabla}C_{\mathrm{I}^0} \tag{2.28}$$

$$\vec{J}_{\mathrm{I}} = \sum_{i=-1}^{+1} \vec{J}_{\mathrm{I}^i} = -D_{\mathrm{I}^0}(1 + K_{\mathrm{I}^+}(p/n_i) + K_{\mathrm{I}}^-(n/n_i))\vec{\nabla}C_{\mathrm{I}^0} \tag{2.29}$$

The last equation was obtained by the simplifying assumption that interstitials at different charge states diffuse equally fast, that is $D_{\mathrm{I}^0} = D_{\mathrm{I}^+} = D_{\mathrm{I}^-}$. There is no experimental evidence to show that they diffuse at different speeds.

2.1.5 Pair diffusion with both point defects, including Fermi level effects

We will merely state the results here. Derivation is analogous to the previous sections. The only point to pay attention here is that the fractional interstitialcy component of diffusion may change with Fermi level. For example it is known that phosphorus diffuses primarily via interstitials when it is intrinsic, but it diffuses primarily via vacancies when present in large concentrations [11]. We can handle this situation by having separate components like $D_{\mathrm{B}}^{\mathrm{I}^+}$, which stand for "diffusivity of boron due to the positively charged interstitials." We may write:

$$
\begin{aligned}
D_B^{I^0} + D_B^{V^0} &= D_B^0 \\
D_B^{I^+} + D_B^{V^+} &= D_B^+ \\
\frac{D_B^{I^0} + D_B^{I^+}}{D_B^0 + D_B^+} &= f_I^{\text{intr}}
\end{aligned}
\tag{2.30}
$$

where f_I^{intr} is the fractional interstitialcy component of diffusion for intrinsic boron. That is, f_I^{intr} is the fraction of diffusivity caused by the interstitials for intrinsic conditions. Of course, these three equations are not enough to determine the four unknowns $D_B^{I^0}$, $D_B^{V^0}$, $D_B^{I^+}$ and $D_B^{V^+}$, so, another assumption must be made based on the experimental data for the dopant. For example, we can assume that boron diffuses always through interstitialcy mechanism at all Fermi levels. We can then define:

$$
\begin{aligned}
D_B^I &= D_B^{I^0} + D_B^{I^+}\left(\frac{p}{n_i}\right) + D_B^{I^-}\left(\frac{n}{n_i}\right) \\
D_B^V &= D_B^{V^0} + D_B^{V^+}\left(\frac{p}{n_i}\right) + D_B^{V^-}\left(\frac{n}{n_i}\right)
\end{aligned}
\tag{2.31}
$$

This results in the following system of equations:

$$
\begin{aligned}
\frac{\partial C_B^T}{\partial t} &= -\vec{\nabla}\vec{J}_{BI} - \vec{\nabla}\vec{J}_{BV} \\
\frac{\partial C_I^T}{\partial t} &= -\vec{\nabla}\vec{J}_I - \vec{\nabla}\vec{J}_{BI} - k_R^{\text{eff}}(C_{I^0}C_{V^0} - C_{I^0}^* C_{V^0}^*) \\
\frac{\partial C_V^T}{\partial t} &= -\vec{\nabla}\vec{J}_V - \vec{\nabla}\vec{J}_{BV} - k_R^{\text{eff}}(C_{I^0}C_{V^0} - C_{I^0}^* C_{V^0}^*)
\end{aligned}
\tag{2.32}
$$

where

$$
\begin{aligned}
\vec{J}_{BI} &= -D_B^I/C_{I^0}^* \left[\vec{\nabla}(C_B C_{I^0}) + C_B C_{I^0}\vec{\nabla}\ln(p/n_i)\right] \\
\vec{J}_{BV} &= -D_B^V/C_{V^0}^* \left[\vec{\nabla}(C_B C_{V^0}) + C_B C_{V^0}\vec{\nabla}\ln(p/n_i)\right] \\
\vec{J}_I &= -D_{I^0}\chi_I\vec{\nabla}C_{I^0} \\
\vec{J}_V &= -D_{V^0}\chi_V\vec{\nabla}C_{V^0} \\
k_R^{\text{eff}} &= k_R(\chi_I + \pi_I C_B)(\chi_V + \pi_V C_B)
\end{aligned}
\tag{2.33}
$$

with

$$
\begin{aligned}
\chi_I &= 1 + K_{I^+}\left(\frac{p}{n_i}\right) + K_{I^-}\left(\frac{n}{n_i}\right) \\
\chi_V &= 1 + K_{V^+}\left(\frac{p}{n_i}\right) + K_{V^-}\left(\frac{n}{n_i}\right) \\
\pi_I &= K_{BI^0} + K_{BI^+}K_{I^+}\left(\frac{p}{n_i}\right) + K_{BI^-}K_{I^-}\left(\frac{n}{n_i}\right) \\
\pi_V &= K_{BV^0} + K_{BV^+}K_{V^+}\left(\frac{p}{n_i}\right) + K_{BV^-}K_{V^-}\left(\frac{n}{n_i}\right)
\end{aligned}
\tag{2.34}
$$

13

If $C_{BI} \ll C_B$ and $C_{BV} \ll C_B$, one can assume that $C_B^T = C_B$ and write:

$$
\begin{aligned}
C_I^T &= (\chi_I + \pi_I C_B) C_{I^0} \\
C_V^T &= (\chi_V + \pi_V C_B) C_{V^0}
\end{aligned}
\tag{2.35}
$$

A note about the recombination rate k_R^{eff}: Actually the rate is too high as given here, because it also includes recombination terms that actually would not be present. For example, an V^- and I^- would be very unwilling to recombine because they would repel each other. If the dopant is an acceptor, we would have 4 such pairs: I^- and V^-; I^+ and V^+, BI^0 and V^-; BV^0 and I^- (Note that BI^0 is actually negatively charged). For an acceptor, BI^- and BV^- are unlikely to exists, so we don't have to consider them.

Thus we have only 4 extra pairs out of the 25 pairs that can recombine with each other. The error of including these 4 pairs in the expression for recombination is often negligible, and makes the equations much simpler. If more accuracy is desired, the following must be subtracted from the k_R^{eff} above:

$$
k_R[K_{I-}K_{V-}(n/n_i)^2 + K_{I+}K_{V+}(p/n_i)^2 + K_{BI^0}K_{V-}(n/n_i) + K_{BV^0}K_{I-}(n/n_i)]
\tag{2.36}
$$

2.1.6   Five stream model

If we don't make the assumption that pairing is fast, we should keep all five variables. We can carry out a similar analysis to eliminate the charging reactions. The resulting system can be expressed as:

$$
\begin{aligned}
\frac{\partial C_B}{\partial t} &= -R_{BI} - R_{BV} + R_{BI+V} + R_{BV+I} + 2R_{BI+BV} \\
\frac{\partial C_{BI}}{\partial t} &= -\vec{\nabla}\vec{J}_{BI} + R_{BI} - R_{BI+V} - R_{BI+BV} \\
\frac{\partial C_{BV}}{\partial t} &= -\vec{\nabla}\vec{J}_{BV} + R_{BV} - R_{BV+I} - R_{BI+BV} \\
\frac{\partial C_I^T}{\partial t} &= -\vec{\nabla}\vec{J}_I - R_{BI} - R_{I+V} \\
\frac{\partial C_V^T}{\partial t} &= -\vec{\nabla}\vec{J}_V - R_{BV} - R_{I+V}
\end{aligned}
\tag{2.37}
$$

where

$$
\begin{aligned}
\vec{J}_{BI} &= -\frac{D_B^I}{C_{I^0}^*}\left[\vec{\nabla}\left(\frac{C_{BI}}{\pi_I}\right) + \frac{C_{BI}}{\pi_I}\vec{\nabla}\ln\left(\frac{p}{n_i}\right)\right] \\
\vec{J}_{BV} &= -\frac{D_B^V}{C_{V^0}^*}\left[\vec{\nabla}\left(\frac{C_{BV}}{\pi_V}\right) + \frac{C_{BV}}{\pi_V}\vec{\nabla}\ln\left(\frac{p}{n_i}\right)\right] \\
R_{BI} &= k_{BI}[C_B C_I - \frac{\chi_I}{\pi_I}C_{BI}] \\
R_{BV} &= k_{BV}[C_B C_V - \frac{\chi_I}{\pi_I}C_{BV}] \\
R_{BI+V} &= k_R(C_{BI}C_V - C_{I^0}^* C_{V^0}^* \pi_I \chi_V C_B)
\end{aligned}
\tag{2.38}
$$

14

$$R_{\text{BV+I}} = k_{\text{R}}(C_{\text{BV}}C_{\text{I}} - C^*_{\text{I}0}C^*_{\text{V}0}\pi_V\chi_I C_{\text{B}})$$
$$R_{\text{BV+BI}} = k_{\text{R}}(C_{\text{BV}}C_{\text{BI}} - C^*_{\text{I}0}C^*_{\text{V}0}\pi_I\pi_V C^2_{\text{B}})$$

and other variables have same meanings as in the previous section.

2.2 Initial conditions: Damage created by ion implantation

To develop models for TED, we need to have a good understanding of the damage the ion implantation process creates. Since there is no accurate way of measuring the damage profile experimentally, we have to rely on Monte-Carlo simulations for calculation of the implant damage. In this work, we used the Monte-Carlo ion implant simulators TRIMCSR [4, 53] and UT-Marlowe [51].

The damage creation process can be summarized as follows: As an ion with high kinetic energy enters the silicon substrate, it undergoes a series of collisions with a number of silicon atoms. The kinetic energy of the ion is high enough to displace these atoms from their original sites, leaving a vacancy behind. These secondary ions also collide with other silicon atoms, etc., creating a collision cascade. One implanted ion can easily create thousands of Frenkel pairs (interstitial-vacancy pairs), depending on the energy and mass of the implanted ion. If the created damage is high enough, the substrate will become amorphous.

2.2.1 Non-amorphizing implants

We first want to investigate non-amorphizing implants. In these types of implants, the dose of the implanted ion is small enough that the created damage doesn't reach the amorphization threshold. Thus, the substrate maintains it crystalline nature, although there is extensive damage in the crystal structure.

TRIMCSR assumes that the structure is amorphous to begin with. Therefore, it ignores any channeling that may occur due to the crystalline nature of the substrate. On the other hand, UT-Marlowe takes the crystal structure of the substrate into account and can predict the tilt and rotation dependence of the tail of the profile. The difference between the two simulators is obvious as represented in Figure 2.1. Even though the implant has been performed at 7° tilt and 45° rotation to minimize channeling, still substantial channeling occurs. Therefore, UT-Marlowe will be our choice of simulator for non-amorphizing implants.

Looking at the damage created by the ion implantation process, we can see that the number of Frenkel pairs generated is much higher than the number of implanted ions (Fig. 2.2). In fact, the interstitial and vacancy curves are almost indistinguishable from each other, but there is a vacancy-rich region near the surface and an interstitial-rich region deeper in the substrate. This stems from the fact that the implantation drives some silicon atoms deeper into the substrate.

We know that even during the implantation process the Frenkel pairs will recombine. After an extremely small thermal budget (1 ms at 600°C), we would expect that most Frenkel pairs would have recombined because the system is so far away from equilibrium. This would leave us with a net "+1" damage, where each incoming ion displaces one silicon atom, such that the net I−V dose is equal to the implant dose.
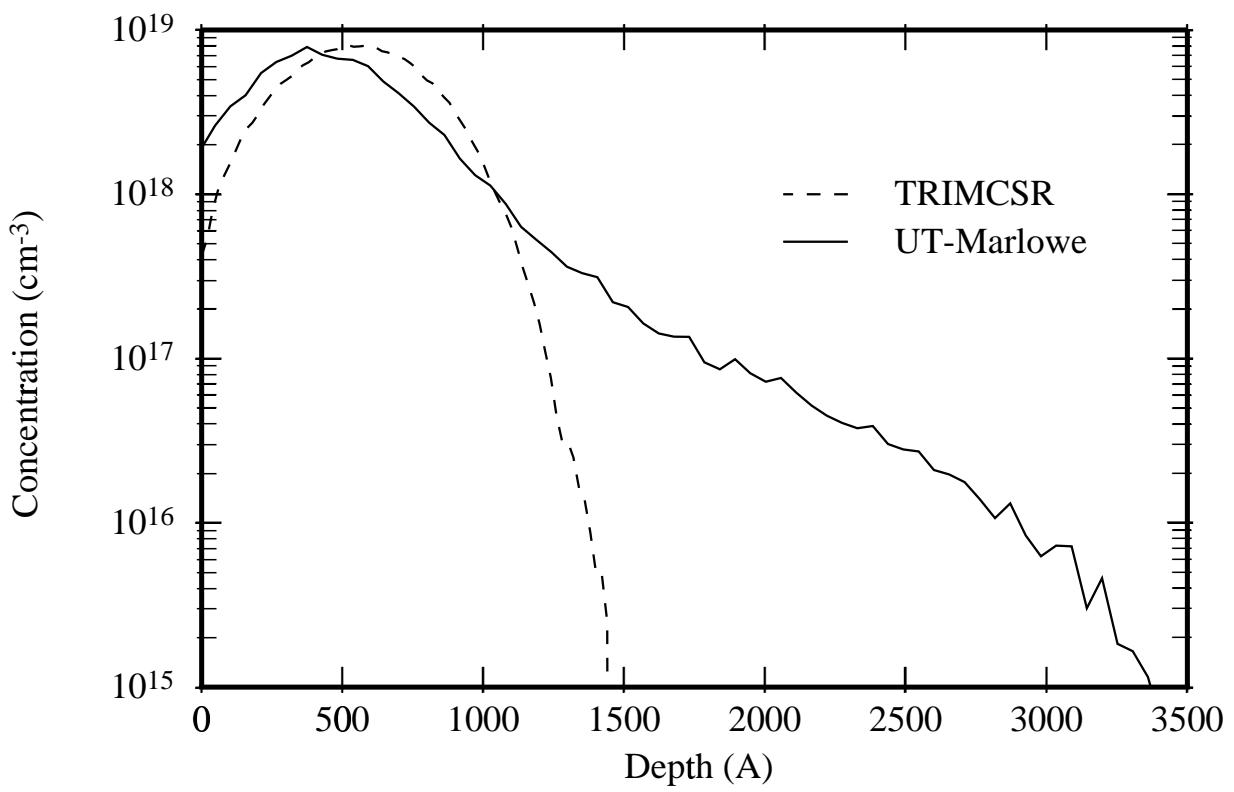
Figure 2.1: Comparison of UT-Marlowe and TRIMCSR simulations of a $40\,\text{keV}$ $5 \times 10^{13}\,\text{cm}^{-2}$ Si implant at 7° tilt and 45° rotation.
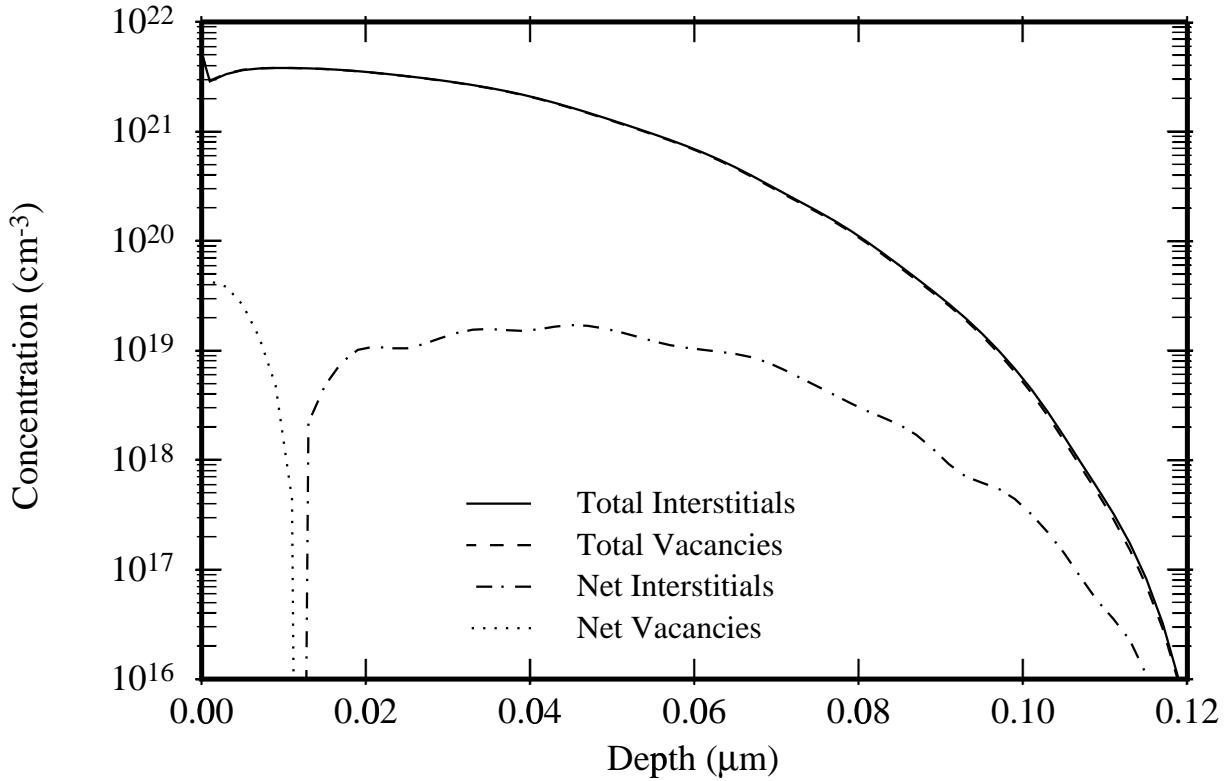
Figure 2.2: Total and net damage created by a $40\,\text{keV}$ $5 \times 10^{13}\,\text{cm}^{-2}$ Si implant. Monte Carlo simulations with TRIMCSR.

16
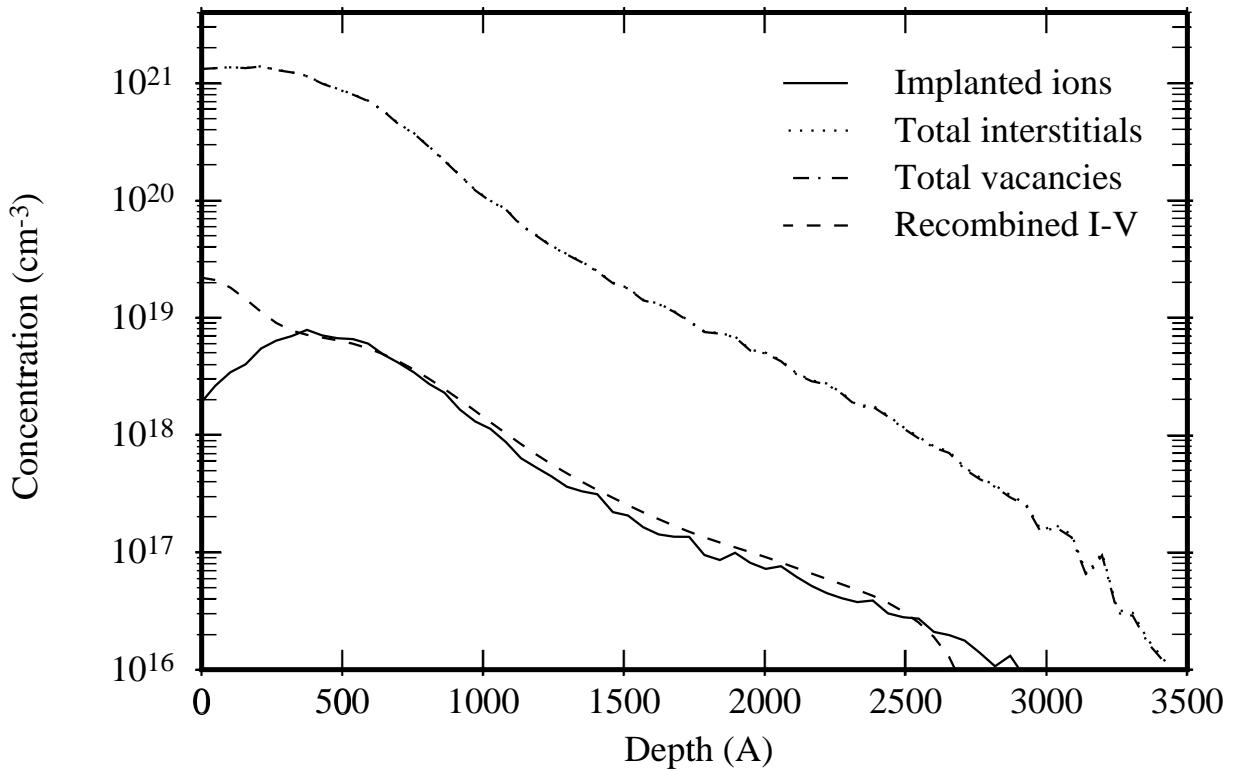
Figure 2.3: Damage created by a $40\,\mathrm{keV}$ $5 \times 10^{13}\,\mathrm{cm}^{-2}$ Si implant before and after very short annealing.

However, I/V recombination is not the only process occurring during the post implant phase. Interstitials and and vacancies can also diffuse and recombine at the surface. Ab-initio calculations show that the diffusivity of vacancies is higher than the diffusivity of interstitials, particularly at lower temperatures. Thus we would expect the vacancies in the vacancy-rich region near the surface to recombine at the surface more readily than they would recombine with an interstitial. To demonstrate this effect, we have performed simulations assuming that $D_\mathrm{V} \gg D_\mathrm{I}$ and both surface recombination and I/V recombination are diffusion limited processes. Figure 2.3 shows that we indeed get a region near the surface where the net I$-$V concentration is higher than predicted by a "+1" approach, and the net I$-$V dose is larger than "+1".

This effect is, however, dose dependent. If we have a relatively high dose, there is a higher probability that a vacancy will first find an interstitial and recombine with it. If we have a relatively low dose, there is a higher chance that the vacancy will hit the surface before finding another interstitial. Therefore, we would expect the net I$-$V dose after recombination to be increasing with decreasing implant dose. We have run a series of simulations to affirm this perception, and indeed we see that the "plus factor" can be as high as 10 (Fig. 2.4).

Note that there are also other phenomena occurring during the implantation process, such as amorphous pocket formation, which might increase the magnitude of the "+n" effect. Formation of amorphous pockets confines the interstitials and vacancies to a relatively small region in space. If a vacancy manages to escape the amorphous pocket, it has a fairly high chance of hitting the surface rather than another amorphous pocket. We believe that we have taken this effect into account to some extend by assuming $D_\mathrm{I} = 0$ in our simulations, but clearly atomistic simulations are required to accurately

17
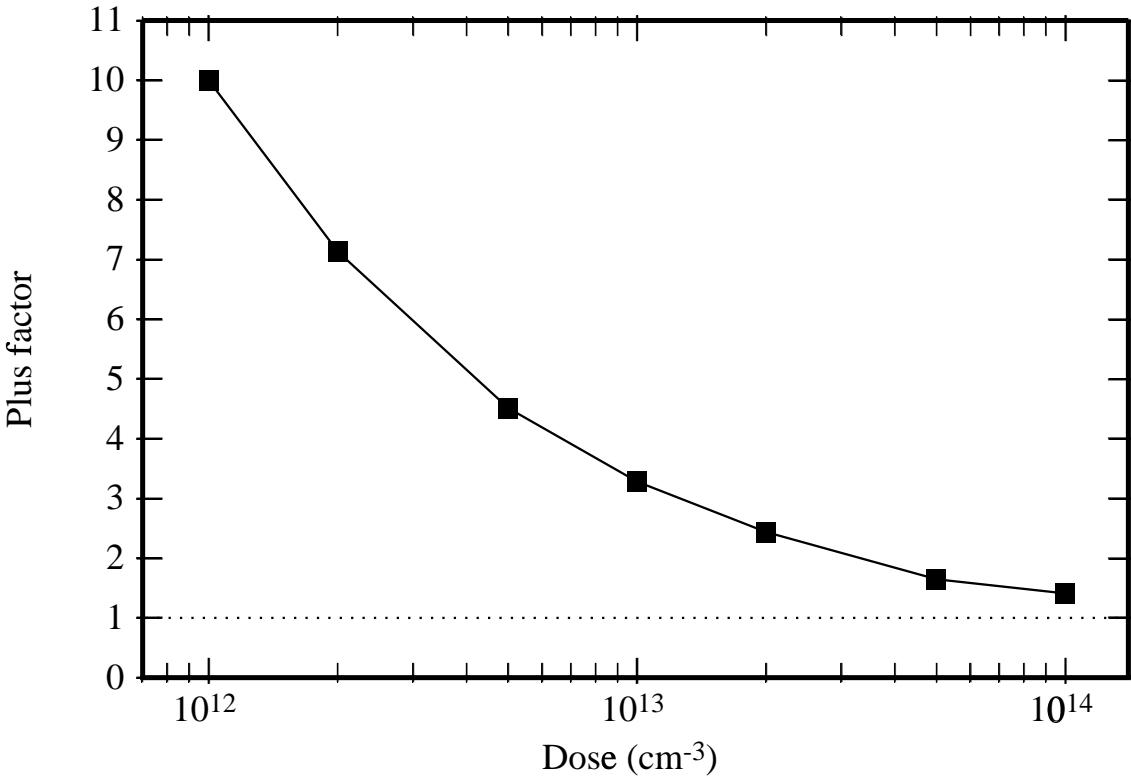
Figure 2.4: Net damage (I−V) dose divided by implant dose (plus factor) for a series of non-amorphizing 40 keV Si implants.

estimate these effects.

2.2.2 Amorphizing implants

The picture is slightly different for amorphizing implants. If the substrate is amorphized up to a certain depth (the amorphous/crystalline interface), this portion will regrow epitaxially, giving a defect free region around the peak of the implant, and leaving an excess interstitial profile only near the tail of the profile (Fig. 2.5). This interstitial rich region is also called the end of range (EOR) region and this is where the dislocation loops form.

Note that the net damage dose is much less than the implant dose, since much of the damage goes away during solid phase epitaxial regrowth. Therefore, TED from an amorphizing implant can actually be *less* than from a non-amorphizing implant. However, dislocation loops, which are very stable, have a negative impact on the device characteristics: They are in the middle of the depletion region, and therefore increase the leakage current of the junction.

Another important difference from the non-amorphizing implants is that the amorphization threshold has no unique value. Amorphization threshold is the total vacancy concentration above which the substrate is assumed to be amorphized. It is usually expressed as a percentage of the silicon atom concentration (5×10^{22} cm^{-3}). Studies have shown that this threshold depends on implant temperature and implant dose rate, since both of these factors affect the damage accumulation process [47].

Moreover, the net I−V dose is a very strong function of the amorphous/crystalline (a/c) interface.
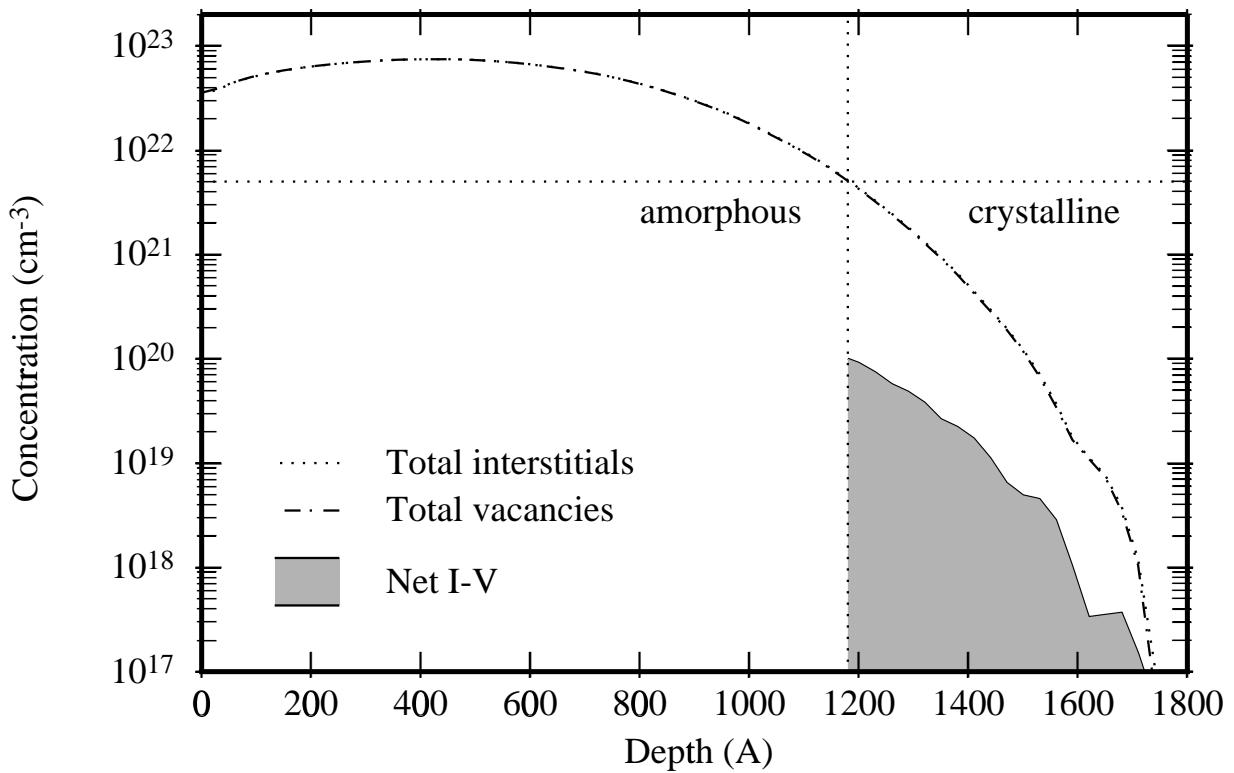
Figure 2.5: TRIMCSR simulation of total and net implant damage for a $50\,\mathrm{keV}$ $1 \times 10^{15}\,\mathrm{cm}^{-2}$ Si implant. Amorphization threshold has been assumed to be 10%.

Under conditions of Fig. 2.5, a $30\,\text{Å}$ change in the a/c interface would change the net I$-$V dose by 25%. Even if the a/c interface is measured experimentally, the end of range damage still cannot be determined accurately because of the sensitivity of the net I$-$V dose on the location of the a/c interface. Therefore, it is important to have another measure, such as the number of interstitials trapped in dislocation loops, to model the net damage under amorphizing conditions.

2.3   Other parameters

2.3.1   Point defect properties

One of the most important parameters for TED is point defect properties, especially those of interstitials. We tried to use as accurate values as possible, but since no direct measurement of point defect properties can be performed, all parameter values we obtain in our simulations have to be re-calibrated when a different set of point defect properties is used. In this section, we investigate the relationship between point defect properties and modeling results.

The most important parameter is the self diffusion coefficient via interstitials ($D_\mathrm{I}C_\mathrm{I}^*$ product). The value of this product directly effects simulation results. More precisely, $D_\mathrm{I}C_\mathrm{I}^*$ and $\sqrt{Dt}$ (the junction movement during TED) are inversely proportional to each other. Luckily, the $D_\mathrm{I}C_\mathrm{I}^*$ can be relatively well determined from experiments. However, the most reliable experiments for determining $D_\mathrm{I}C_\mathrm{I}^*$ are metal diffusion experiments, which are usually performed at higher temperatures than TED

conditions. Therefore, a small error in the activation energy of $D_I C_I^*$ may lead to a big error in TED predictions.

The values of diffusivity of interstitials (D_I) and equilibrium concentration of interstitials (C_I^*) individually don't affect TED results directly, as long as their product is constant. The duration of TED is controlled by the flux of interstitials towards the surface, which is directly proportional to the ratio of solid solubility of interstitial (C_{ss}) to C_I^*. Thus, as long as the $D_I C_I^*$ product and C_{ss}/C_I^* ratio is constant, the results will remain unchanged.

The vacancy parameters don't affect the simulation results both for TED and extended defect evolution, except for the "+n" effect described in section 2.2.1. Even for that effect, the actual value of D_V is irrelevant; the only thing that is important is $D_V \gg D_I$.

In summary, the primarily relevant point defect properties are $D_I C_I^*$ and C_{ss}/C_I^*. In this thesis, point defect values from metal diffusion are used [5, 58] consistently. I/V recombination is not a significant process for TED (except for the first μs); therefore we can assume for simplification that it is diffusion limited. We have also assumed that interstitial precipitation (formation of extended defects) is also diffusion limited. This assumption is necessary if we assume fast surface recombination (see next section), in order to ensure a steady interstitial flux towards the surface.

2.3.2   Surface recombination

Under TED conditions, the surface is the main sink for interstitials. Data by Eaglesham *et al.* [17] suggest a surface recombination rate that is decreasing with time, since the rate at which interstitials are consumed is decreasing approximately exponentially with time. Other experimental observations also indicate that a fast effective interstitial surface regrowth exists for small thermal budgets, with a much slower one for longer times and higher temperatures [15]. Thus, rather than using a simple model with constant surface recombination rate, we used the film segregation model of Agarwal and Dunham [1] to account for surface regrowth. In this model, the primary mechanism by which the surface consumes interstitials is not surface recombination, but segregation of interstitials to the oxide layer.

However, after performing a series of simulations, we find that the surface has no strong effect on the results, as long as it has a fast recombination rate. The main reason behind the exponential decay in Eaglesham's data is Ostwald ripening process. We find that using a fast, constant surface recombination model gives almost exactly the same results as the film segregation model. Therefore, we switched to a constant surface recombination model where we assumed that the ratio of the surface recombination velocity and interstitial diffusivity is $\geq 0.1\,\text{Å}^{-1}$.

Chapter 3

Modeling Extended Defects with Kinetic Precipitation Model

3.1 Introduction

As mentioned in section 1.2.3, Transmission Electron Microscopy (TEM) observations [10, 17] show that {311} defects (also known as "rod-like defects") form, grow and eventually dissolve during annealing of ion implanted samples. Initially, there is a huge driving force to form {311} defects, such that, for sub-amorphizing silicon implants, almost the whole net excess interstitial dose aggregates into these extended defects within a very short period of time (less than $5\,\mathrm{s}$ at $815°\mathrm{C}$) [17]. As annealing continues, these defects undergo Ostwald ripening: Their average size increases and their number decreases. The total number of interstitials bound to these defects decreases approximately exponentially, and eventually, all {311} defects dissolve and disappear. It has been reported that the time scale for their dissolution is about the same as the time scale of TED [10]. These observations strongly suggest that {311} defects play a central role under TED conditions. If we could model the evolution of these defects correctly, we should be able to predict TED.

In general, nucleation and growth processes play a critical role in a large range of materials processing systems. Classical modeling approaches divide such processes into two discrete steps, with nucleation and growth being modeled using fundamentally different assumptions, each valid only under idealized conditions. Thus, although these approaches are very useful for understanding qualitative behavior, they are unsuitable in many cases for the development of quantitative models, particularly under complex annealing conditions (e.g., multi-step anneals). Noting the power of modern computers to solve complex systems of coupled differential equations, we have developed a unified approach to modeling of nucleation and growth processes which extends nucleation theory to include the behavior of supercritical as well as sub-critical aggregates.

3.2 Full Kinetic Precipitation Model (FKPM)

The major challenge in modeling the evolution of precipitates and extended defects is the fact that different sized defects have very different properties. The Full Kinetic Precipitation Model (FKPM) [14] treats precipitates of different sizes as independent species (f_n) and accounts for their kinetics by
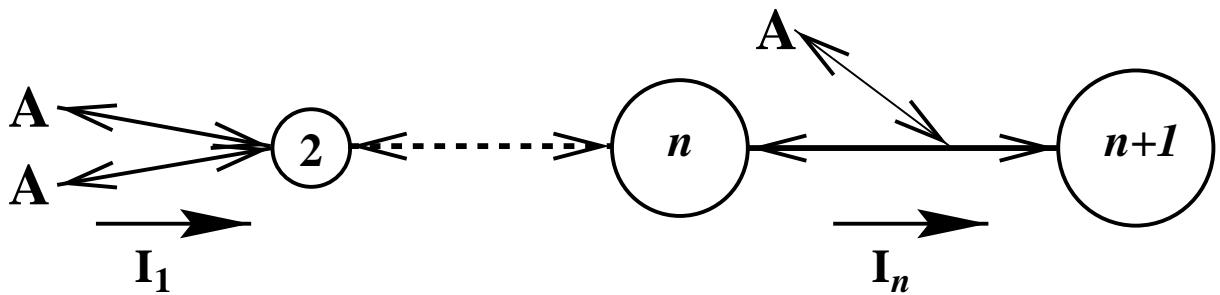
Figure 3.1: Growth and dissolution of precipitates by attachment and emission of solute atoms.

considering the attachment and emission of solute atoms (Fig 3.1).

The driving force for precipitation is the minimization of the free energy of the system, where the free energy of a size n extended defect is given by:

$$\Delta G_n = -nkT \ln \frac{C_A}{C_{ss}} + \Delta G_n^{exc} \tag{3.1}$$

Here, C_A denotes the solute concentration, C_{ss} is the solid solubility and ΔG_n^{exc} is the excess surface and strain energy of a size n extended defect. We usually assume that ΔG_n^{exc} has a polynomial form, since any function can be approximated by a polynomial:

$$\Delta G_n^{exc} = a_0 n^{\beta_0} + a_1 n^{\beta_1} + a_2 n^{\beta_2} \tag{3.2}$$

with $\beta_2 < \beta_1 < \beta_0 < 1$. The largest exponent ($\beta_0$) controls the asymptotic behavior for large sizes. Theoretical calculations [43] for the functional form of ΔG_n^{exc} show that it is reasonable to assume that $\beta_0 = 0.5$ since {311} defects are planar defects. We used $\beta_1 = -0.2, \beta_1 = -1$ as corrections for small size behavior. a_0, a_1 and a_2 remain as temperature independent fitting parameters.

The main reaction in the system is the attachment and emission of solute atoms to and from precipitates. If I_n denotes the net growth rate from size n to $n+1$, we may write the following equation:

$$I_n = \begin{cases} D\lambda_n \left(C_A f_n - C_n^* f_{n+1}\right) & \text{for } n \geq 2 \\ D\lambda_1 \left(C_A^2 - C_1^* f_2\right) & \text{for } n = 1 \end{cases} \tag{3.3}$$

Note that I_1 is different from other terms, because it represents the rate for formation of the defects by reaction of two interstitials.

The growth rate of precipitates is written in the form $D\lambda_n$, where λ_n incorporates effects of both diffusion to the precipitate/silicon interface and the reaction at the interface. λ_n is calculated based on solving the steady-state diffusion equation in the neighborhood of a precipitate, taking its shape into account (see Appendix A). C_n^* represents the interstitial concentration at which there would be no change in free energy for a precipitate growing from size n to size $n+1$. C_n^* can be found by setting $\Delta G_n = \Delta G_{n+1}$ and solving for C_A.

$$C_n^* = C_{ss} \exp\left(\frac{\Delta G_{n+1}^{exc} - \Delta G_n^{exc}}{kT}\right) \tag{3.4}$$

The evolution of the size distribution f_n is given by the difference between the net rate at which defects grow from size $n-1$ to n (I_{n-1}) and the net rate of growth from size n to $n+1$ (I_n). Since the

fundamental growth process is the incorporation of a solute atom, the total change in C_A includes a term from each growth reaction, giving a sum over I_n:

$$\frac{\partial f_n}{\partial t} = I_{n-1} - I_n \tag{3.5}$$

$$\frac{\partial C_A}{\partial t} = -2I_1 - \sum_{n=2}^{\infty} I_n \tag{3.6}$$

3.3 Reduced Kinetic Precipitation Models (RKPM)

The Full Kinetic Precipitation Model adds an extra dimension, namely precipitate size, to the problem being solved. Even if one limits the number of precipitate sizes that will be solved for, the number of variables is still very large for efficient solution of the equation system. If the system has multiple spatial dimensions, the number of solution variables becomes prohibitively large.

To minimize the computational budget, we have developed a more efficient version of this model, based on the work of Clejan and Dunham [8]. Instead of calculating all the f_n, one calculates only the lowest *moments* of the distribution ($m_i = \sum_{n=2}^{\infty} n^i f_n$, where $i = 0, 1, 2, \ldots$). This transforms the system of equations to the following set:

$$\frac{\partial m_i}{\partial t} = 2^i I_1 + \sum_{n=2}^{\infty} \left[(n+1)^i - n^i \right] I_n \tag{3.7}$$

Note that the sums over the I_n can all be written in terms of sums over f_n, $n f_n$, etc. Hence, they can be calculated from the moments if moments are used to describe the distribution. This reduces the system of equations to be solved to:

$$\frac{\partial m_i}{\partial t} = D_A \left[2^i \lambda_1 C_A^2 + m_0 C_A \gamma_i^+ - m_0 C_{ss} \gamma_i^- \right]$$

$$\gamma_i^+ = \sum_{n=2}^{\infty} \left[(n+1)^i - n^i \right] \lambda_n \hat{f}_n \tag{3.8}$$

$$\gamma_i^- = \lambda_1 \hat{C}_1^* \hat{f}_2 + \sum_{n=2}^{\infty} \left[n^i - (n-1)^i \right] \lambda_{n-1} \hat{C}_{n-1}^* \hat{f}_n$$

where $\hat{C}_n^* = C_n^*/C_{ss}$ and $\hat{f}_n = f_n/m_0$.

Since no finite number of moments can fully describe a full distribution, we need a closure assumption, which is an assumption about the form of the distribution, $f_n = f(n, z_i)$. The z_i are parameters of the distribution which can be determined from the moments. The number of moments we need to keep track of equals the number of parameters in the distribution function. This results in different versions of RKPM:

3.3.1 3-moment model (3KPM)

If nothing is known about the distribution of extended defects over size space, it is logical to use an energy minimizing closure assumption [8]. The energy minimizing closure assumption assumes that

23

the distribution will be the one that minimizes the free energy, given the moments. It can be found from constrained minimization of the free energy (ΔG_n). This results in the following (normalized) distribution with three parameters:

$$\hat{f}_n = z_0 \exp\left(-\Delta G_n^{\text{exc}}/kT + z_1 n + z_2 n^2\right) \tag{3.9}$$

The resulting system is a 3-moment system (3KPM):

$$
\begin{aligned}
\frac{\partial m_0}{\partial t} &= D\left[\lambda_1 C_A^2 - m_0 C_{\text{ss}} \gamma_0^-\right] \\
\frac{\partial m_1}{\partial t} &= D\left[2\lambda_1 C_A^2 + m_0 C_A \gamma_1^+ - m_0 C_{\text{ss}} \gamma_1^-\right] \\
\frac{\partial m_2}{\partial t} &= D\left[4\lambda_1 C_A^2 + m_0 C_A \gamma_2^+ - m_0 C_{\text{ss}} \gamma_2^-\right] \\
\frac{\partial C_A}{\partial t} &= -\frac{\partial m_1}{\partial t}
\end{aligned}
\tag{3.10}
$$

with

$$
\begin{aligned}
\gamma_0^- &= \lambda_1 \hat{C}_1^* \hat{f}_2 \\
\gamma_1^+ &= \sum_{n=2}^{\infty} \lambda_n \hat{f}_n \\
\gamma_1^- &= \lambda_1 \hat{C}_1^* \hat{f}_2 + \sum_{n=2}^{\infty} \lambda_{n-1} \hat{C}_{n-1}^* \hat{f}_n \\
\gamma_2^+ &= \sum_{n=2}^{\infty} (2n+1)\lambda_n \hat{f}_n \\
\gamma_2^- &= \lambda_1 \hat{C}_1^* \hat{f}_2 + \sum_{n=2}^{\infty} (2n-1)\lambda_{n-1} \hat{C}_{n-1}^* \hat{f}_n
\end{aligned}
\tag{3.11}
$$

For the 3-moment model (3KPM), the distribution function is not readily integrable. Therefore, we can't analytically replace a function of the parameters of the distribution function with a function of the moments, which are our solution variables. Instead, we have to solve the following set of non-linear, coupled equations at every time step and grid point:

$$
\begin{aligned}
1 &= \sum_{n=2}^{\infty} z_0 \exp\left(-\Delta G_n^{\text{exc}}/kT + z_1 n + z_2 n^2\right) \\
\hat{m}_1 &= \sum_{n=2}^{\infty} n z_0 \exp\left(-\Delta G_n^{\text{exc}}/kT + z_1 n + z_2 n^2\right) \\
\hat{m}_2 &= \sum_{n=2}^{\infty} n^2 z_0 \exp\left(-\Delta G_n^{\text{exc}}/kT + z_1 n + z_2 n^2\right)
\end{aligned}
\tag{3.12}
$$

To make the simulation computationally efficient, we solve the above non-linear set of equations for a range of $\hat{m}_1$ and $\hat{m}_2$ values and calculate the γ_i for these values. Then the γ_i are stored in a lookup

24
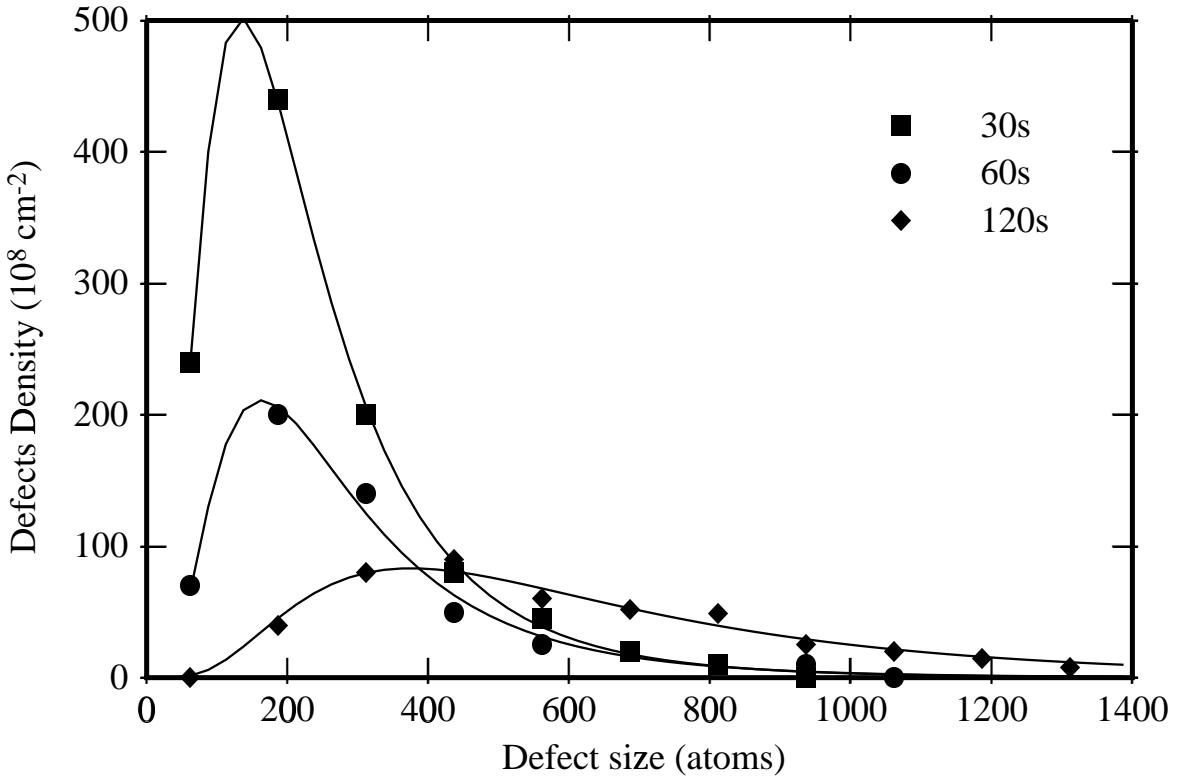
Figure 3.2: Distribution of {311} defect densities over defect sizes and best fit to log-normal distribution. $z_2 = 0.8$ has been used in all fits. Data from Pan and Tu [41].

table and interpolation is used to find values of γ_i for values of $\hat{m}_i$ that have not been tabulated. Clejan and Dunham have applied this system to dopant deactivation and showed that the use of a moment based approach doesn't refrain us from capturing the physics of the system [8].

3.3.2 2-moment model (2KPM)

For {311} defects and dislocation loops, the size distribution has been measured experimentally [41]. The results suggest that the distribution is roughly log-normal:

$$f_n = z_0 \exp(-\ln(n/z_1)^2/z_2) \tag{3.13}$$

When we analyze the data, we find that z_2 appears to be independent of annealing time. The distributions can be approximated by log-normal distributions with $z_2 = 0.8$ (Fig. 3.2). Thus, we can reduce the number of parameters (hence number of moments) to 2. The resulting system is a 2-moment system (2KPM):

$$
\begin{aligned}
\frac{\partial m_0}{\partial t} &= I_1 = D\left[\lambda_1 C_A^2 - m_0 C_{ss}\gamma_0^-\right] \\
\frac{\partial m_1}{\partial t} &= 2I_1 + Dm_0\left[C_A\gamma_1^+ - C_{ss}\gamma_1^-\right] \\
\frac{\partial C_A}{\partial t} &= -\frac{\partial m_1}{\partial t}
\end{aligned}
\tag{3.14}
$$

25
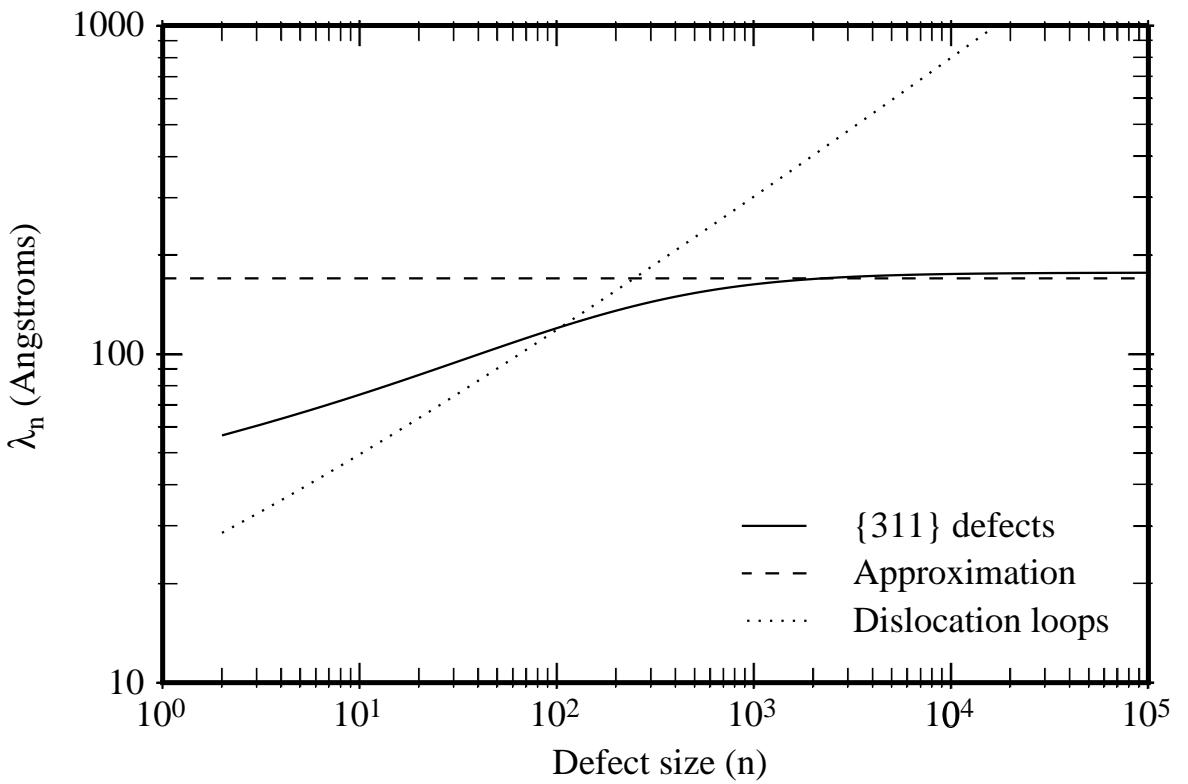
Figure 3.3: Change of λ_n versus defect size for {311} defects and dislocation loops. The calculation can be found in Appendix A.

with

$$
\begin{aligned}
\gamma_0^- &= \lambda_1 \hat{C}_1^* \hat{f}_2 \\
\gamma_1^+ &= \sum_{n=2}^{\infty} \lambda_n \hat{f}_n \\
\gamma_1^- &= \sum_{n=2}^{\infty} \lambda_n \hat{C}_n^* \hat{f}_{n+1}
\end{aligned}
\tag{3.15}
$$

Note that for the 2KPM, the integral of the distribution function can be found analytically, and therefore the parameters of the distribution can be calculated from the moments by means of analytical functions. This eliminates the need for the lookup table and interpolation, giving speed and robustness advantages. However, still the γ_i need to be calculated by sums, which is an iterative process.

3.4   Analytical Kinetic Precipitation Model (AKPM)

RKPM, although computationally more efficient than the FKPM, can still be very costly for large simulations in multiple dimensions. We have developed an even more efficient version starting with 2KPM.

First of all, we note that for {311} defects, the kinetic precipitation rate λ_n is a weak function of the precipitate size (as compared to dislocation loops) and converges to a constant as the precipitate

26

size increases (Fig. 3.3). Therefore, it would be reasonable to replace λ_n by a constant value λ for all sizes. This value can be found approximately from a weighted sum of λ_n. Therefore, our system reduces to:

$$
\begin{aligned}
\frac{\partial m_0}{\partial t} &= I_1 = D\lambda \left[C_A^2 - m_0 C_{ss} \gamma_0 \right] \\
\frac{\partial m_1}{\partial t} &= 2I_1 + D\lambda m_0 \left[C_A - C_{ss} \gamma_1 \right] \\
\frac{\partial C_A}{\partial t} &= -\frac{\partial m_1}{\partial t}
\end{aligned}
\tag{3.16}
$$

with

$$
\begin{aligned}
\gamma_0 &= \hat{C}_1^* \hat{f}_2 \\
\gamma_1 &= \sum_{n=2}^{\infty} \hat{C}_n^* \hat{f}_{n+1}
\end{aligned}
\tag{3.17}
$$

Note that in the above equations, $\hat{f}_n$ is given by the distribution function we assume, and can be determined fully if $\hat{m}_1$ is given. For example, if the distribution function is a geometric distribution function ($\hat{f}_n = z_0 z_1^n$), then the distribution can be determined by solving the following set of equations:

$$
\begin{aligned}
1 &= \sum_{n=2}^{\infty} z_0 z_1^n \\
\hat{m}_1 &= \sum_{n=2}^{\infty} n z_0 z_1^n
\end{aligned}
\tag{3.18}
$$

The solution of this system gives:

$$
\begin{aligned}
z_1 &= \frac{\hat{m}_1 - 2}{\hat{m}_1 - 1} \\
z_0 &= \frac{1 - z_1}{z_1^2}
\end{aligned}
\tag{3.19}
$$

Hence the normalized distribution can be written in terms of $\hat{m}_1$:

$$
\hat{f}_n = \frac{1}{\hat{m}_1 - 1} \left(\frac{\hat{m}_1 - 2}{\hat{m}_1 - 1} \right)^{n-2}
\tag{3.20}
$$

Since we also assume a functional form for $\hat{C}_n^*$, the γ_i are uniquely defined if $\hat{m}_1$ is known. so, in fact, the γ_i are functions of $\hat{m}_1$:

$$
\begin{aligned}
\gamma_0 &= \gamma_0(\hat{m}_1) \\
\gamma_1 &= \gamma_1(\hat{m}_1)
\end{aligned}
\tag{3.21}
$$

27

Looking at the functional form of $\hat{C}_n^*$ and $\hat{f}_n$, we may write the following limits for these functions:

$$
\begin{aligned}
\lim_{\hat{m}_1 \to 2} \gamma_0 &= \hat{C}_1^* \\
\lim_{\hat{m}_1 \to \infty} \gamma_0 &= 0 \\
\lim_{\hat{m}_1 \to 2} \gamma_1 &= 0 \\
\lim_{\hat{m}_1 \to \infty} \gamma_1 &= 1
\end{aligned}
\tag{3.22}
$$

Thus, for every ΔG_n^{exc} $\hat{f}_n$ pair, we can find a corresponding $\gamma_0(\hat{m}_1)$, $\gamma_1(\hat{m}_1)$ pair; and instead of using the parameters of ΔG_n^{exc} as our fitting parameters, we can use corresponding parameters of $\gamma_0(\hat{m}_1)$ and $\gamma_1(\hat{m}_1)$ as fitting parameters.

To demonstrate this transformation, we use an example. Assume that the size distribution is again geometrical as given by Eq. 3.20. For simplicity of calculation, assume that $\hat{C}_n^*$ is also given in a geometric fashion:

$$
\hat{C}_n^* = ab^{n-1} + 1
\tag{3.23}
$$

This gives $\hat{C}_1^* = 1 + a$ and $\hat{f}_2 = 1/(\hat{m}_1 - 1)$, resulting in:

$$
\gamma_0 = \frac{1 + a}{\hat{m}_1 - 1}
\tag{3.24}
$$

For γ_1, we have to do the following summation:

$$
\begin{aligned}
\gamma_1 &= \sum_{n=2}^{\infty} (ab^{n-1} + 1) \frac{1}{\hat{m}_1 - 1} \left(\frac{\hat{m}_1 - 2}{\hat{m}_1 - 1} \right)^{n-1} \\
&= \frac{\hat{m}_1 - 2}{\hat{m}_1 - 1} \left[\frac{ab}{\hat{m}_1(1 - b) - 1 + b} + 1 \right]
\end{aligned}
\tag{3.25}
$$

Similarly, starting with the polynomial form of ΔG_n^{exc} as given by Eq. 3.2 and the log-normal distribution of the defect sizes as given in Eq. 3.13, we calculate the corresponding $\gamma_0(\hat{m}_1)$, $\gamma_1(\hat{m}_1)$ pairs numerically. Figures 3.4 and 3.5 show the set of calculated γ_i for a given set of coefficients for the polynomial of ΔG_n^{exc}. Our calculations show that the results can be approximated by the following functions of $\hat{m}_1$:

$$
\begin{aligned}
\gamma_0(\hat{m}_1) &= \frac{K_1}{\hat{m}_1 - 1} \\
\gamma_1(\hat{m}_1) &= \frac{\hat{m}_1 - 2}{\hat{m}_1 + K_0} \left(1 + \frac{(K_0 + 2)K_2}{\hat{m}_1 + K_0} \right)
\end{aligned}
\tag{3.26}
$$

To get a feel for these functions, we have plotted them in Figure 3.6, in addition to Figures 3.4 and 3.5. The parameter K_0 controls the x-scale, parameter K_1 defines the overall scale of γ_0 and the parameter K_2 defines the magnitude of the peak for γ_1. Using these three parameters, we can cover a wide range of curve shapes.

Since the γ_i calculated from 2KPM and determined by the analytical functions of AKPM are approximately equal, we would expect that both models would give the same simulation results.
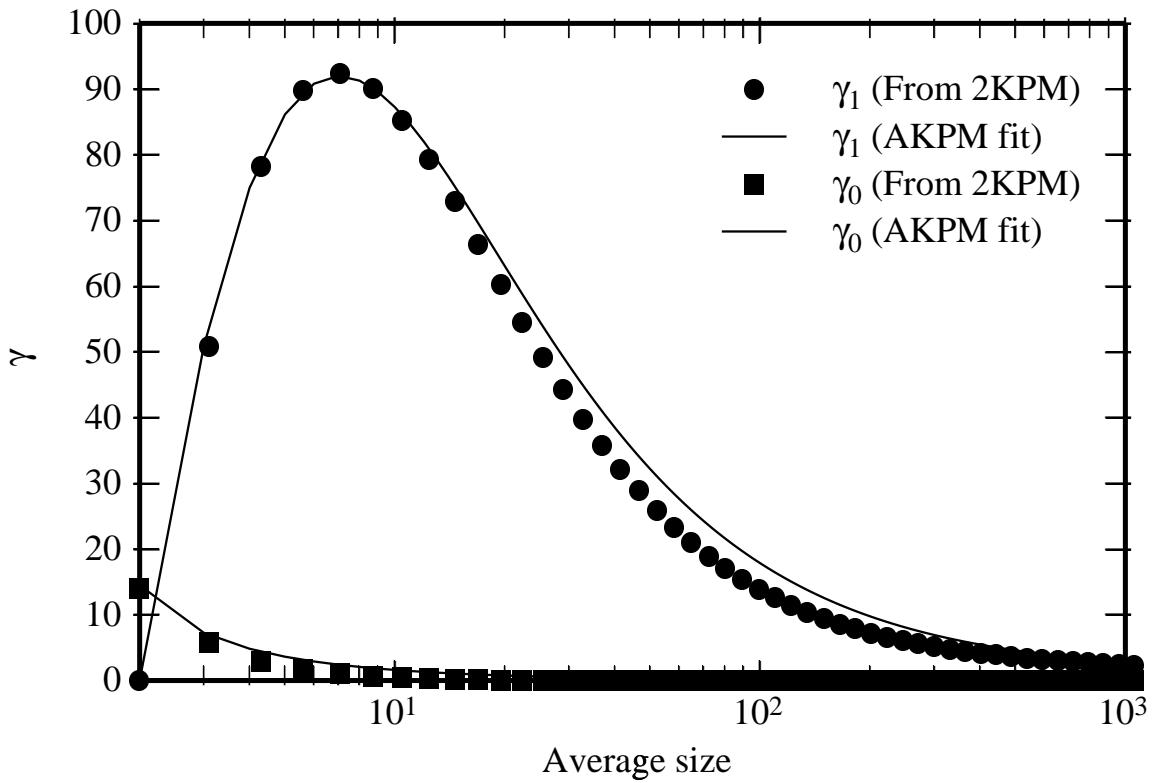
Figure 3.4: The corresponding γ_i as a function of $\hat{m}_1$ for $a_0 = 3.855$, $a_1 = 15.9$, $a_2 = -1.4$. The parameters for γ_i are $K_0 = 3$, $K_1 = 14.5$ and $K_2 = 366$.
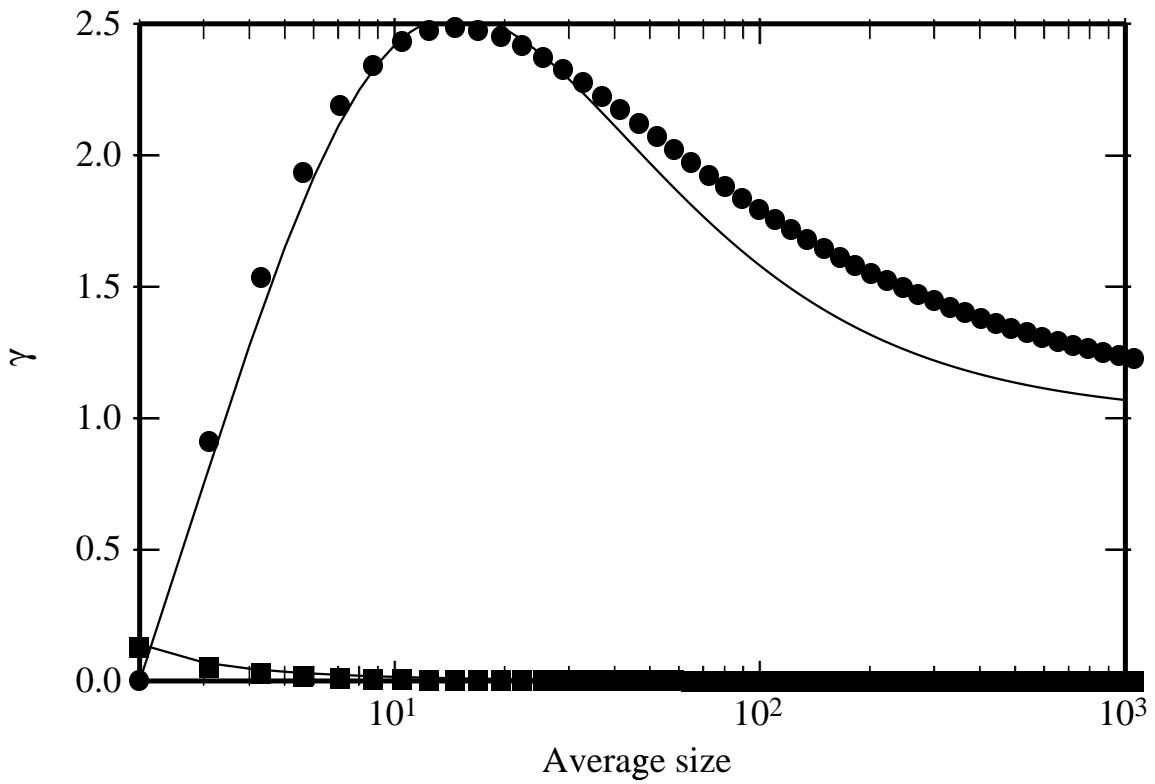
Figure 3.5: The corresponding γ_i as a function of $\hat{m}_1$ for $a_0 = 1$, $a_1 = 4.7$, $a_2 = 0$. The parameters for γ_i are $K_0 = 8$, $K_1 = 0.14$ and $K_2 = 8$.
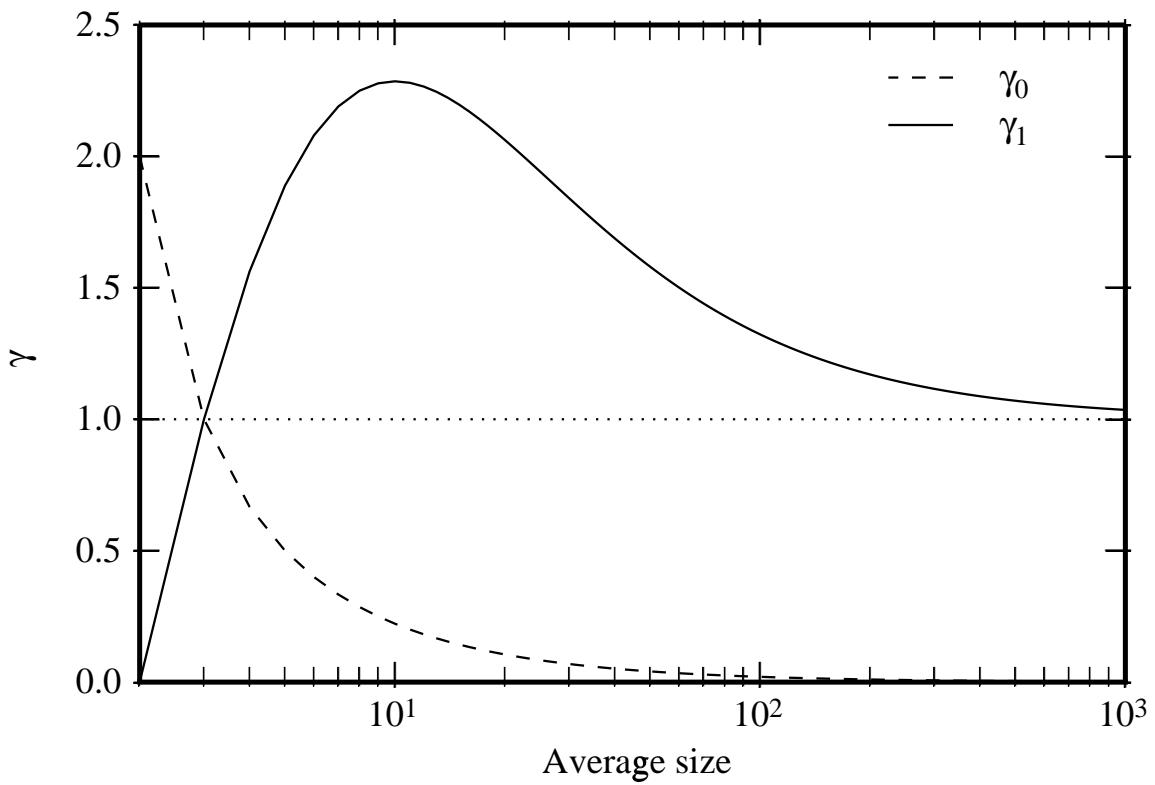
Figure 3.6: Example of γ_i as defined by Eq. 3.27. In this particular plot $K_0 = 4$, $K_1 = 2$ and $K_2 = 7$ have been used.
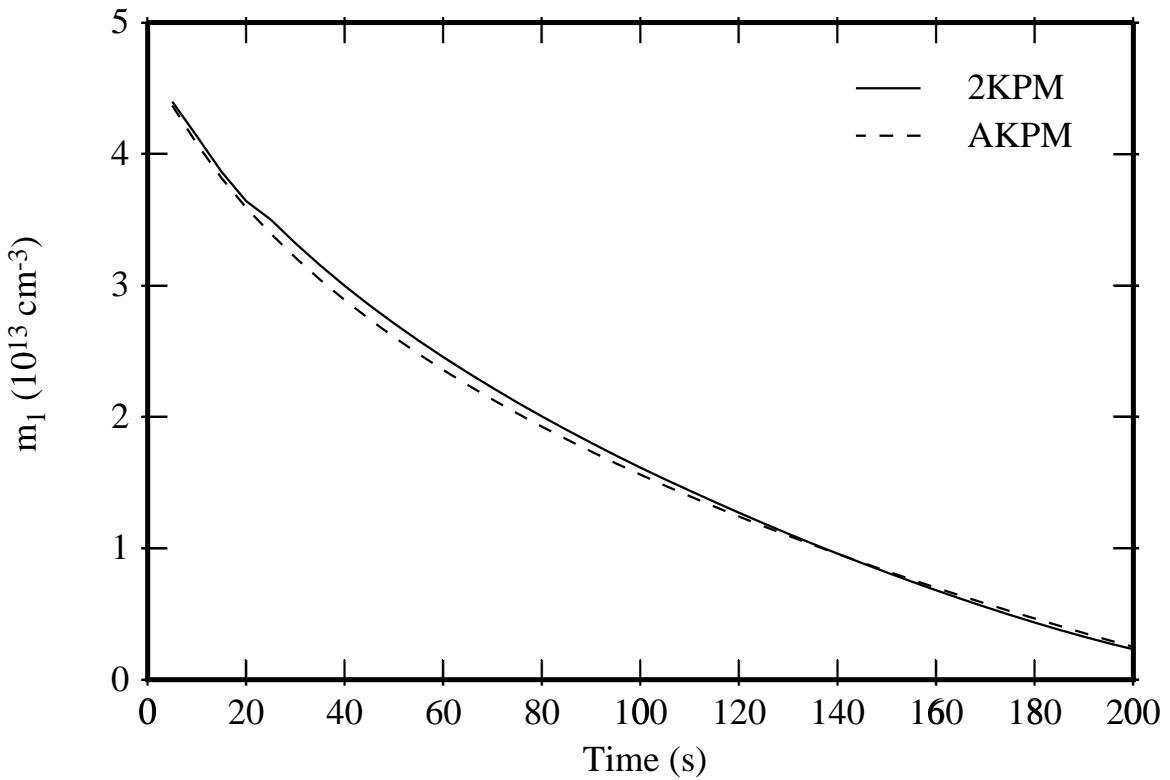
Figure 3.7: Comparison of 2KPM and AKPM under identical conditions and equivalent parameters as given in Fig. 3.4.

Indeed, when we test both models under the same conditions, the results are almost indistinguishable (Fig 3.7). To obtain Fig 3.7, we have used the parameters of Fig. 3.4, with an initial $5 \times 10^{13} \, \text{cm}^{-2}$ interstitial dose.

It is also possible to find $\hat{C}_n^*$, and hence ΔG_n^{exc}, if the parameters of the γ_i (K_i) and the distribution function is given, although this procedure is less straightforward. Since γ_0 is the product of $\hat{C}_1^*$ and $\hat{f}_2$, knowing γ_0, we can easily find $\hat{C}_1^*$. On the other hand, γ_1 is only dependent on $\hat{C}_2^*$ through $\hat{C}_\infty^*$. So, we can find $\hat{C}_n^*$, by solving a large set of linear equations that is defined by:

$$\gamma_1(\hat{m}_1) = \sum_{n=2}^{n_{max}} \hat{C}_n^* \hat{f}_n(\hat{m}_1) \tag{3.27}$$

at different $\hat{m}_1$. Once $\hat{C}_n^*$ is determined, ΔG_n^{exc} can be found by solving the expression for C_n^* (Eq. 3.4) for ΔG_n^{exc}, which gives a recurrence relation:

$$\Delta G_{n+1}^{\text{exc}} = \Delta G_n^{\text{exc}} + kT \ln \hat{C}_n^* \tag{3.28}$$

Obviously, ΔG_1^{exc} must be set as a reference point.

3.5 Simple solid-solubility model (SSS)

All of the above models account for the fact that the characteristics of the precipitates change with changing average size, and therefore can be considered as "sophisticated" models. The simplest model for precipitation is to assume a constant solid solubility cut-off. This amounts to assuming that all solute atoms above the solid solubility level will form precipitates instantaneously. We have added a kinetic rate for this system and will use it for comparisons with KPM models discussed in the text. The rate equations for this model can be formulated as follows:

$$\frac{\partial m_1}{\partial t} = D\lambda m_1 (C_A - C_{ss}) + \begin{cases} D\lambda (C_A - C_{ss})^2 & \text{for } C_A > C_{ss} \\ 0 & \text{for } C_A \leq C_{ss} \end{cases} \tag{3.29}$$

$$\frac{\partial C_A}{\partial t} = -\frac{\partial m_1}{\partial t}$$

The first term in the above equation is for growth/dissolution of the precipitates, whereas the second term is for nucleation of precipitates when $C_A > C_{ss}$. Since this model keeps track of only one moment (m_1), we can classify it as a 1-moment model. This model is similar to the model proposed by Rafferty [48], in the sense that both models capture the dynamics of cluster formation, but use a constant solid solubility.

Chapter 4

Modeling {311} Defects and TED

In this chapter, we will apply the models that were developed in the previous chapter to {311} defect evolution data by Eaglesham *et al.* [17] to obtain parameter values for these models. We will then use these parameters and models to predict TED and compare the predictions to boron marker layer data by Packan [39] and Chao [6].

4.1   Evolution of {311} Defect Profile

Eaglesham *et al.* [17] implanted $5 \times 10^{13}\,\text{cm}^{-2}$ Si into silicon at $40\,\text{keV}$ and annealed the samples at various temperatures. They measured the resulting {311} defect distributions using TEM and reported the moments of this distribution. However, they were unable to observe defects smaller than a cut-off of $20\,\text{Å}$ and assumed that all {311} defects have a constant width of $50\,\text{Å}$. An elongated defect shouldn't have its width larger than its length, so we assumed $w = \min(l, 50\,\text{Å})$ (see Appendix A). We fit our data to moments that we calculate the same way Eaglesham *et al.* did, but we will show that the real moments might be different from those.

First, we applied the 3-moment model (3KPM) to Eaglesham's data. We optimized our parameters (a_0, a_1, a_2 and C_{ss}, with only C_{ss} being temperature dependent) to match the data represented. It can be seen that we were able to obtain a good agreement between the data and the model (Figs. 4.1, 4.2 and 4.3). We show model results both for the full distribution (actual) and the portion of the distribution with size greater than $20\,\text{Å}$ (observable). Note that the average size of the observable defects ($l > 20\,\text{Å}$) seems to diverge from the average size of all defects, and we will explain this behavior later.

To gain a better understanding of the system let us investigate how the depth profile changes over time (Fig. 4.4). It can be observed that the {311} defect pile is being consumed from the side that is closer to the surface, and this process moves the profile deeper into the substrate with time. As a matter of fact, the approximately exponential decay of the number of interstitials in {311} defects arises from the combination of the Ostwald ripening behavior and the shift of the {311} defect frontier away from the surface.

Fig. 4.5 shows a plot of C_n^* versus defect length for this system. It can be observed that C_n^* has a peak around $n = 7$, which would be the least stable cluster size. The fact that small clusters are
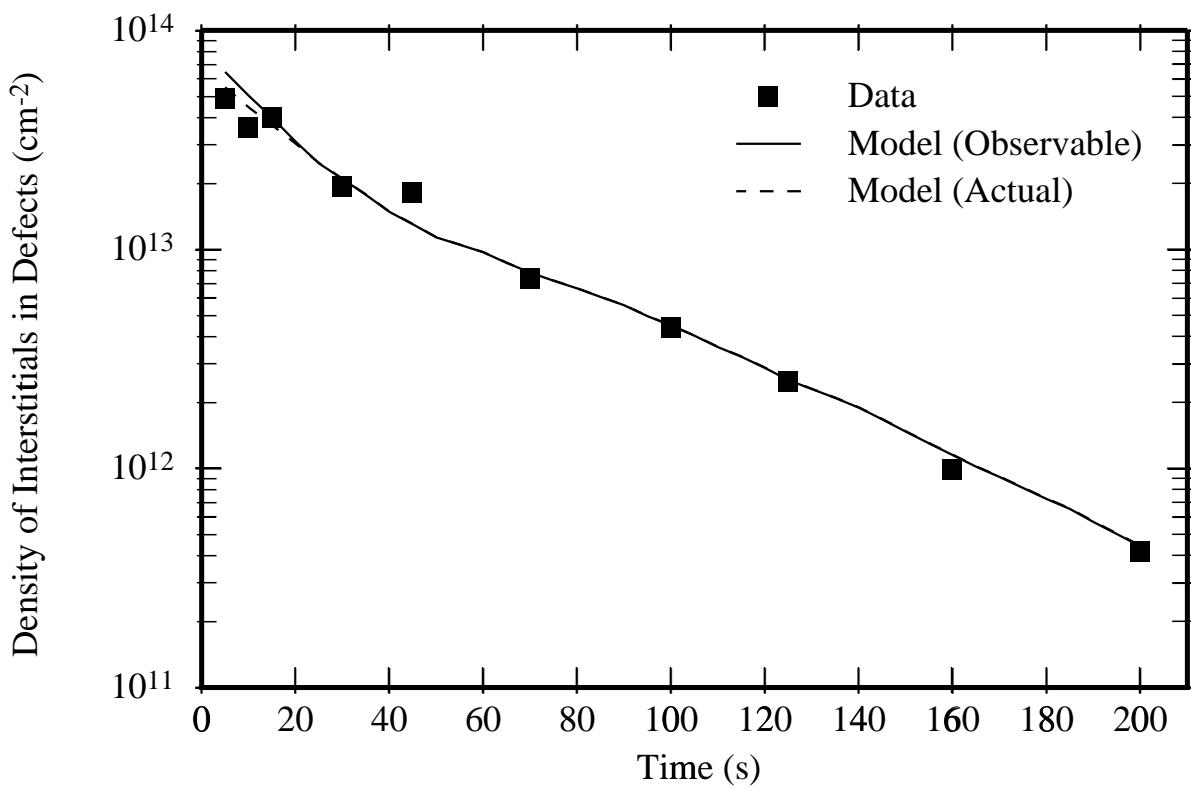
Figure 4.1: Evolution of density of interstitials in $\{311\}$ defects (m_1) and comparison to model. Data for $5 \times 10^{13}\,\mathrm{cm}^{-2}$ Si implant at $40\,\mathrm{keV}$ with anneal at $815°C$.
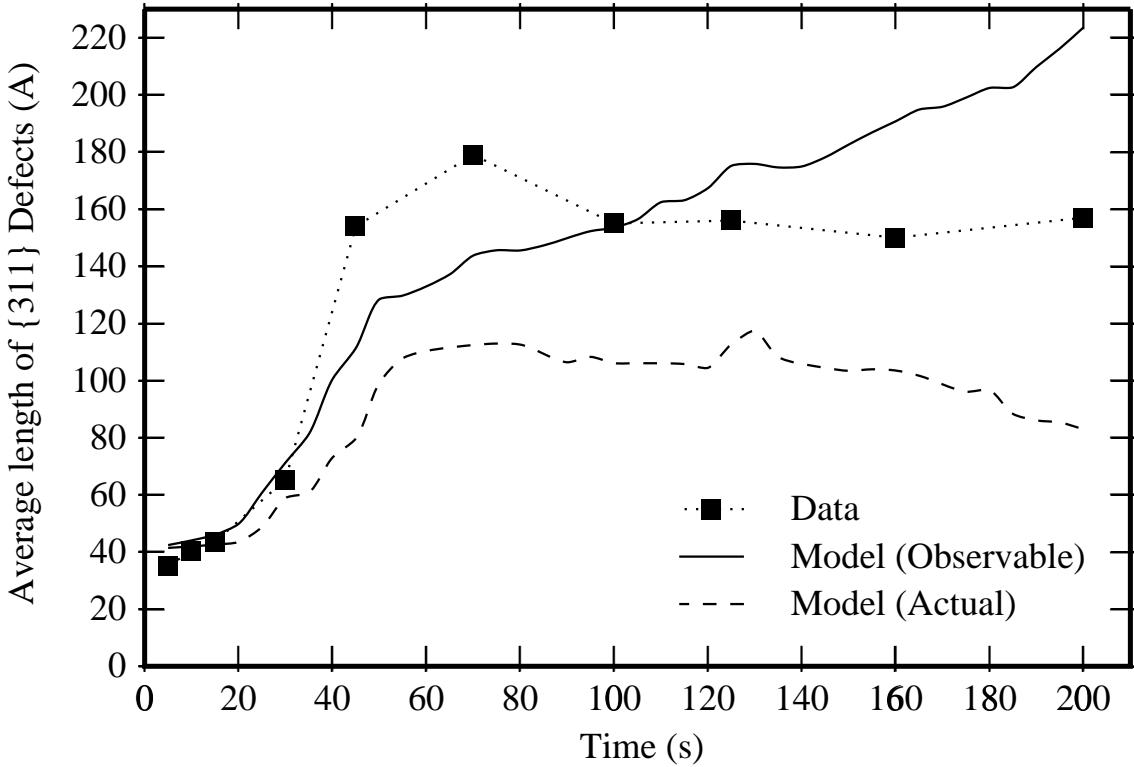
Figure 4.2: Evolution of the average length of $\{311\}$ defects and comparison to model. Data for $5 \times 10^{13}\,\mathrm{cm}^{-2}$ Si implant at $40\,\mathrm{keV}$ with anneal at $815°C$.
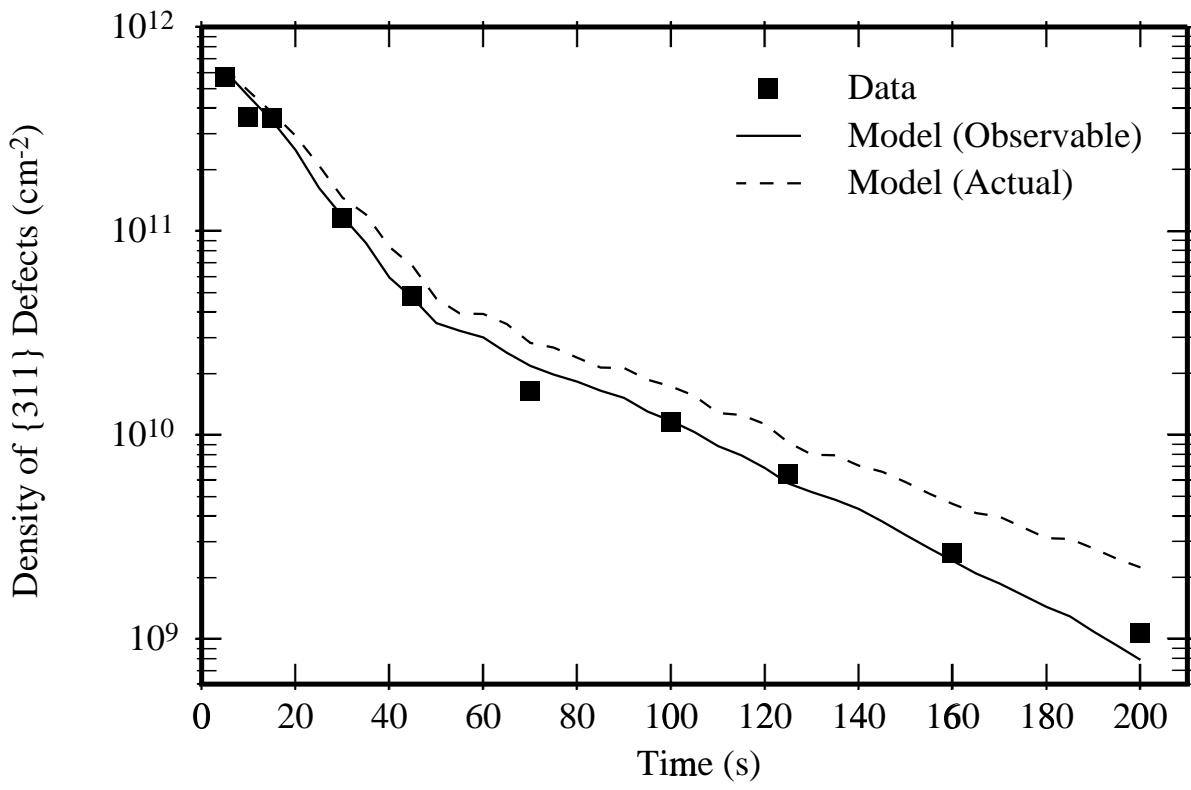
Figure 4.3: Evolution of density of {311} defects (m_0) and comparison to model. Data for $5 \times 10^{13}\,\text{cm}^{-2}$ Si implant at $40\,\text{keV}$ with anneal at 815°C.
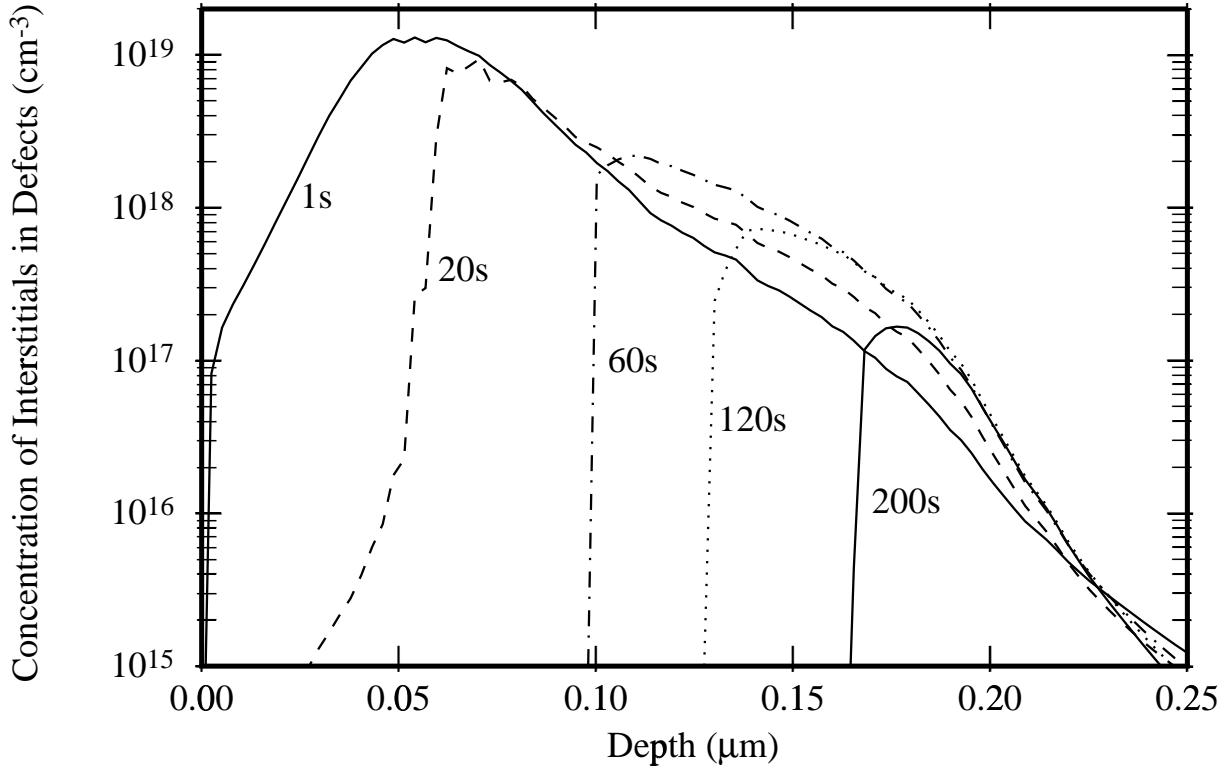
Figure 4.4: The {311} defect profile for various annealing times at 815°C.
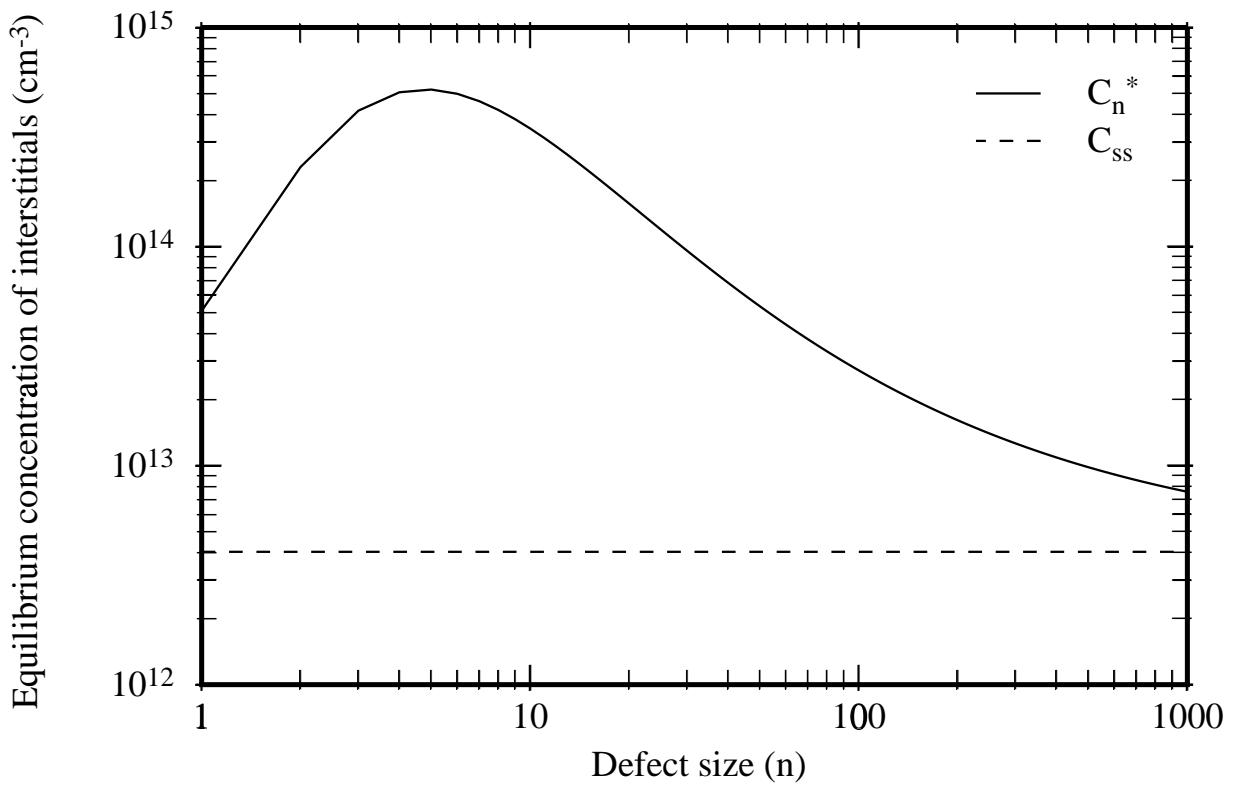
Figure 4.5: C_n^* and C_{ss} versus $\{311\}$ defect size for anneals at 815°C.

stable gives rise to the very rapid formation of $\{311\}$ defects, whereas the continuously decreasing C_n^* for $l > 10\,\text{Å}$ gives rise to the ongoing Ostwald ripening in the system. The leveling off after sizes $l > 300\,\text{Å}$ stops the growth of $\{311\}$ defects around $l = 150\,\text{Å}$, as suggested by the data. Note that the exact shape of C_n^* depends on the form assumed, but the general slope is necessary in order to match the experimental results.

The shape of the distribution over the sizes (Fig. 4.6) also tells us that there is an unstable region of cluster sizes, such that the distributions are double-peaked. This shape of the defect size distribution is an immediate result of the energy-minimizing closure assumption. The fact that Eaglesham *et al.* cannot observe clusters smaller than 20 Å results in an overestimation of the average size (see Fig. 4.2), as well as an underestimation of m_0, the number of clusters (Fig. 4.3). The clusters in the first peak are completely invisible to them. Luckily, these clusters don't contribute significantly to m_1. Note that for a log-normal closure assumption, there is no second peak, such that the average size of observable clusters and all clusters is the same.

We characterized the parameters of the system for different temperatures (specifically, 815°C, 738°C, 705°C and 670°C), taking only C_{ss} as temperature dependent. Two of these fits are shown in Fig. 4.7.

We then applied the same system and parameters to the dose dependence of interstitials in $\{311\}$ defects. Poate *et al.* [46] reported that above a threshold dose the number of interstitials in $\{311\}$ defects at the initial stages of TED increases linearly with implant dose, but with a slope of about 1.4. Our model was able to accurately predict this behavior (Fig. 4.8), both the slope as well as the dose below which no $\{311\}$ defects form.
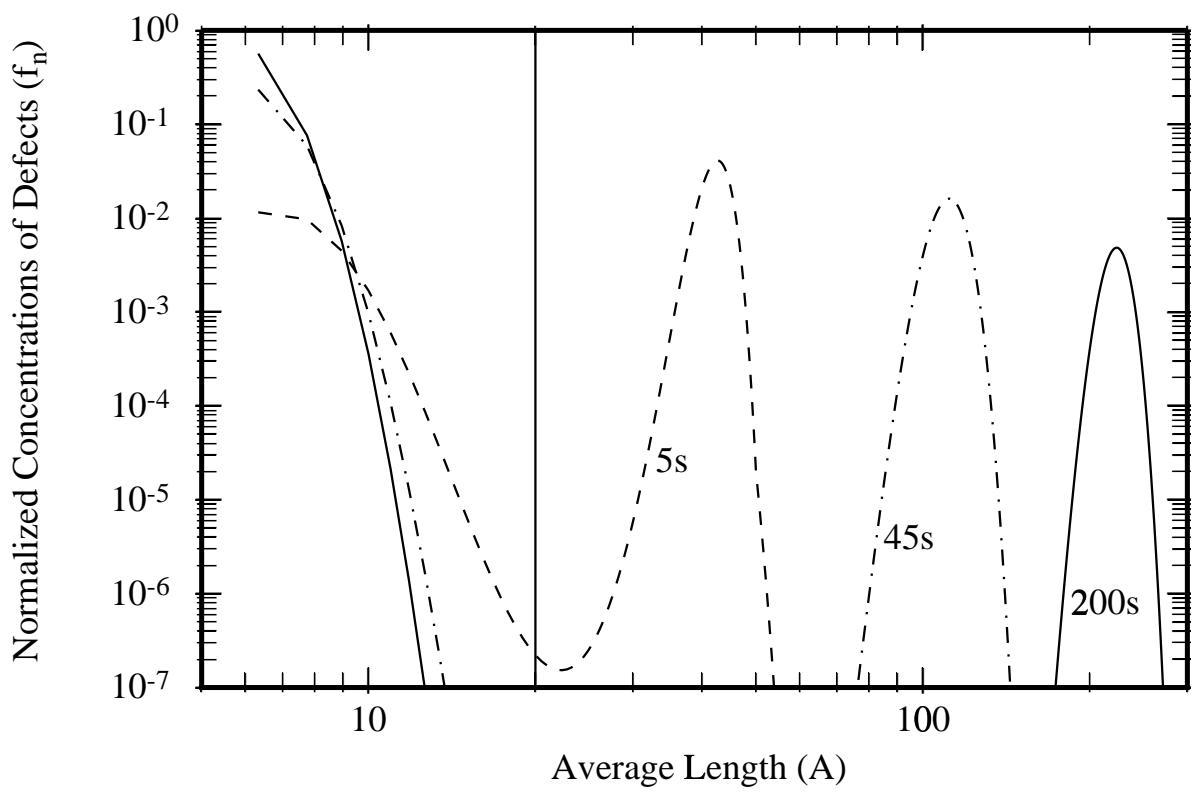
Figure 4.6: Normalized distribution of {311} defect sizes for various times for anneals at 815°C. The vertical line represents the minimum observable defect size (20 Å).
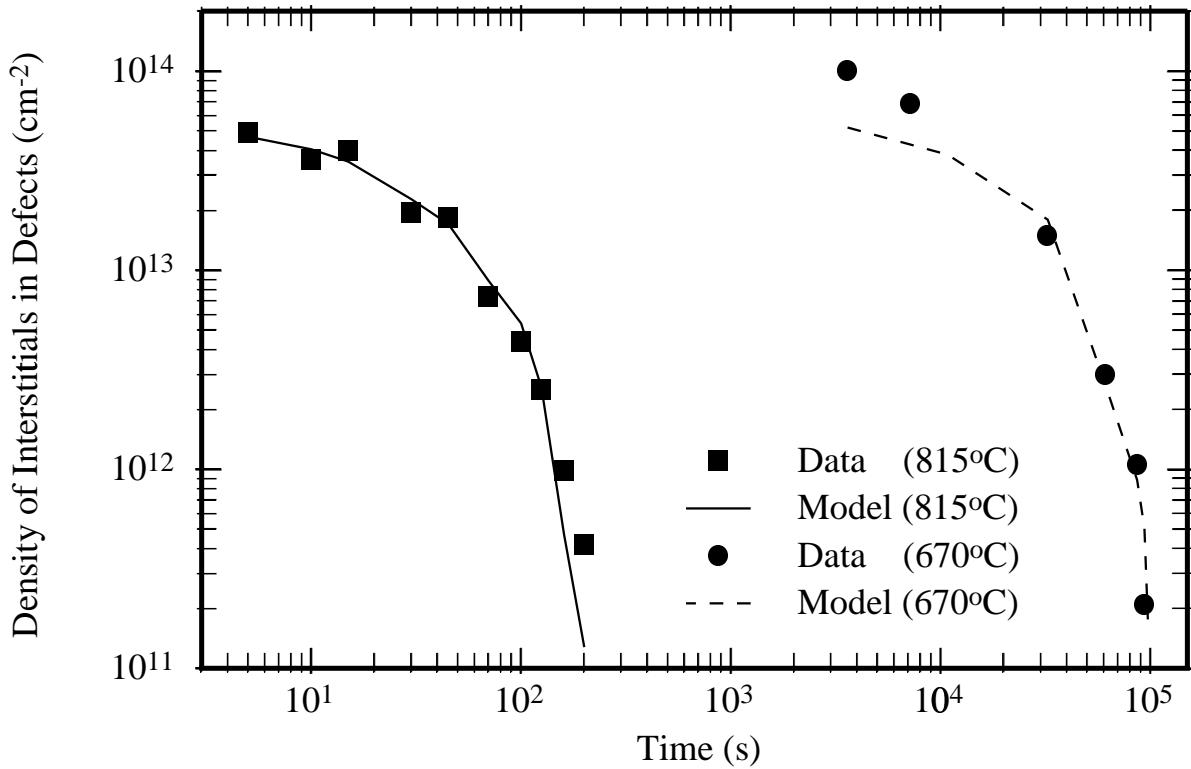

Figure 4.7: Evolution of density of interstitials in {311} defects (m_1) and comparison to model. Data for 5×10^{13} cm^{-2} Si implants at 40 keV with anneals at 815°C and 670°C.
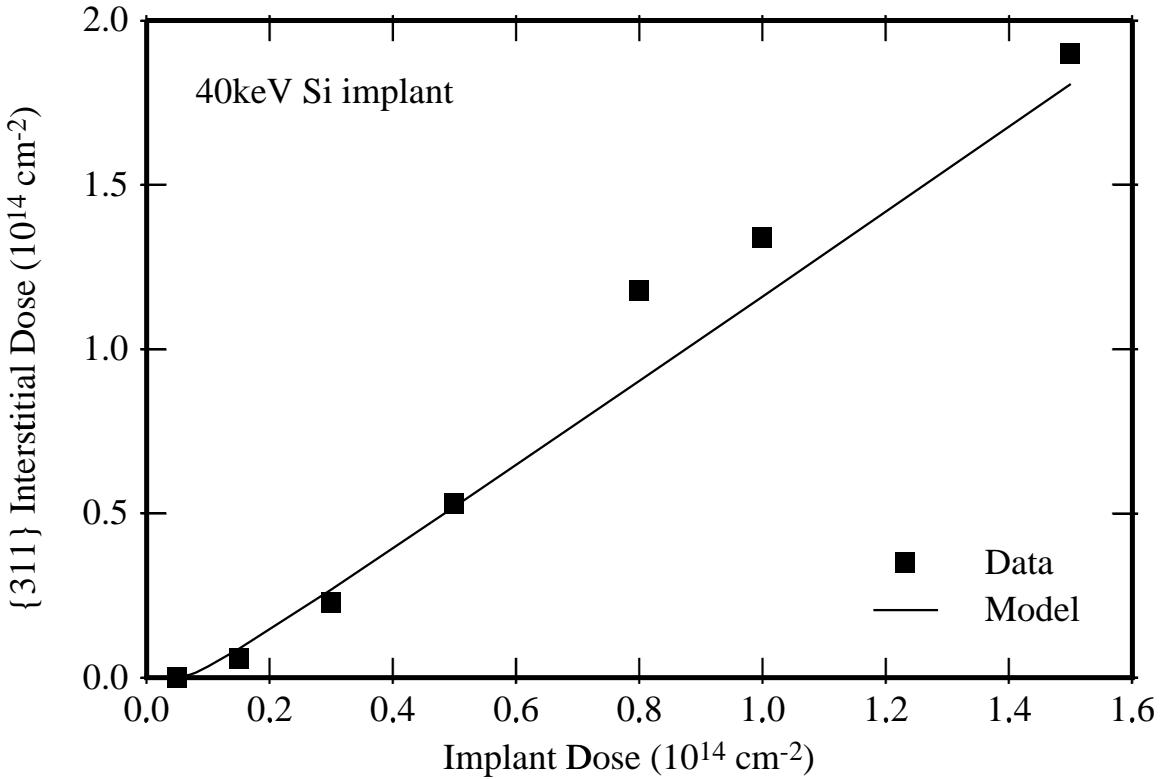
Figure 4.8: Prediction of dose dependence of interstitials in {311} defects during initial stages of TED. Data from Poate *et al.* [46] for 40 keV Si implants and 1 hr anneal at 670°C.

4.2 Prediction of TED

We used the parameters obtained in the previous section to predict TED behavior as a function of implant and annealing conditions. For comparison, we used data from Packan [39], who used implants of ^{29}Si into silicon at energies ranging from 10 keV to 200 keV and doses ranging from 1×10^{12} to 2×10^{14} cm^{-2}. TED was measured by observing profile movement of a deep boron marker layer. No further fitting was done at this stage and all parameters were from work cited previously[1, 5] or from matching data by Eaglesham *et al.*

The results show that the model predictions do a good job in matching the time and energy dependence (Figs. 4.9 and 4.10). The model not only gives the right magnitude for the observed enhancements, but also predicts length of time TED lasts. In addition, it also correctly predicts that higher doses or energies make TED last longer, but give similar enhancements for short times (Fig. 4.10). The predicted dose dependence matches most of the data (Fig. 4.11), with substantial differences only for the lowest implant dose. Please note that in these simulations a "+1" damage dose was used and the effect of using a plus value that is dose dependent will be investigated later.

4.3 Comparison of models

In this section, we will compare four extended defect models: 3-moment model (3KPM), which was demonstrated in the previous section, 2-moment model (2KPM), the simple solid solubility model
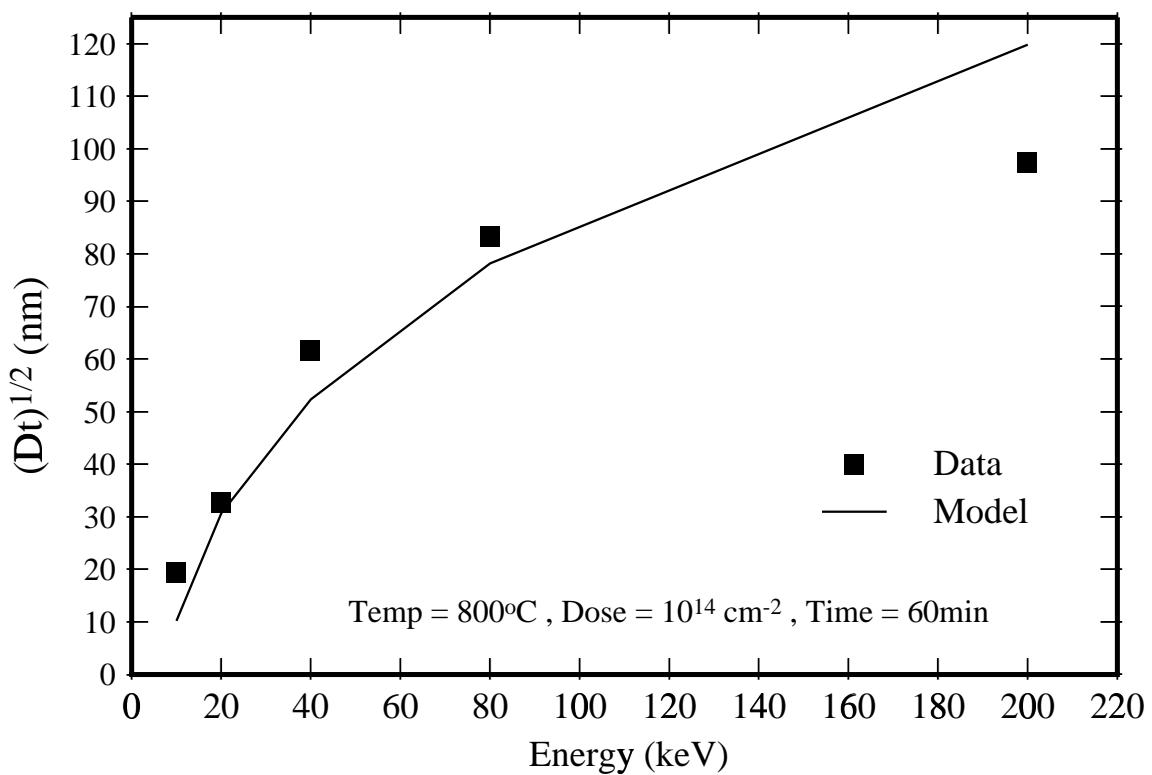
Figure 4.9: Energy dependence of TED. Total broadening of a deep B marker profile due to implantation of $1 \times 10^{14}\,\mathrm{cm^{-2}}$ ^{29}Si with annealing at 800°C for 60 min.
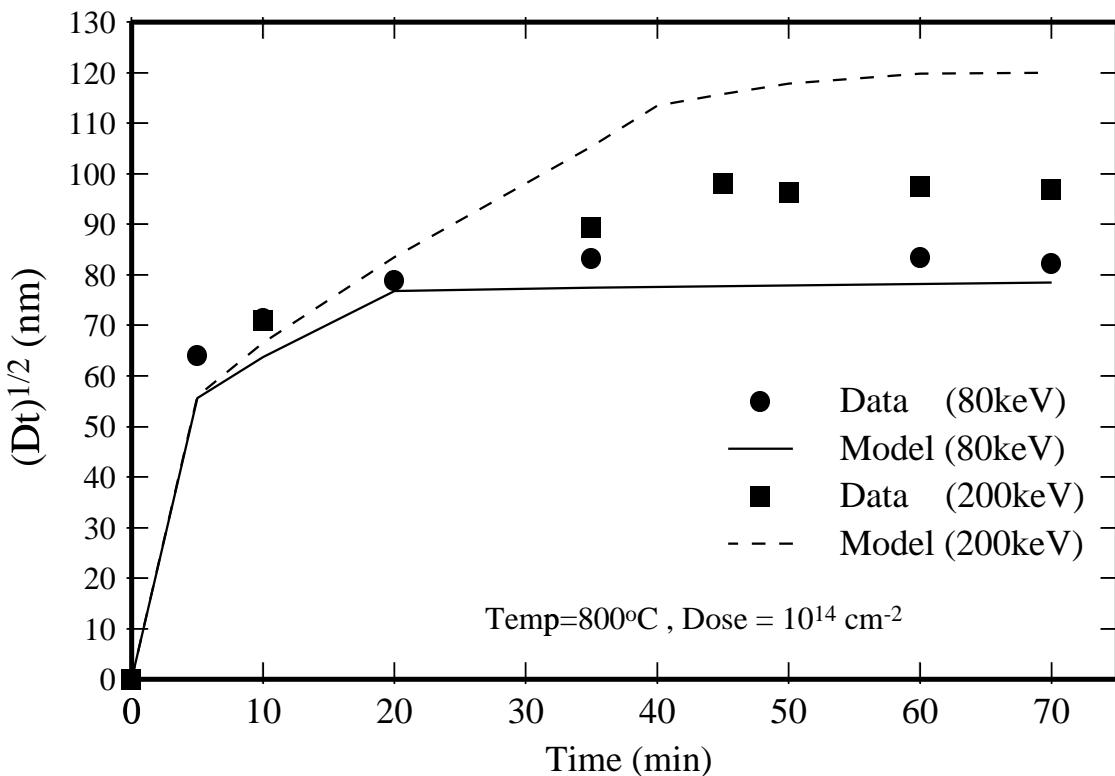
Figure 4.10: Time dependence of TED. Total broadening of a B marker profile due to implantation of $1 \times 10^{14}\,\mathrm{cm^{-2}}$ ^{29}Si at 80 and 200 keV with annealing at 800°C.

38
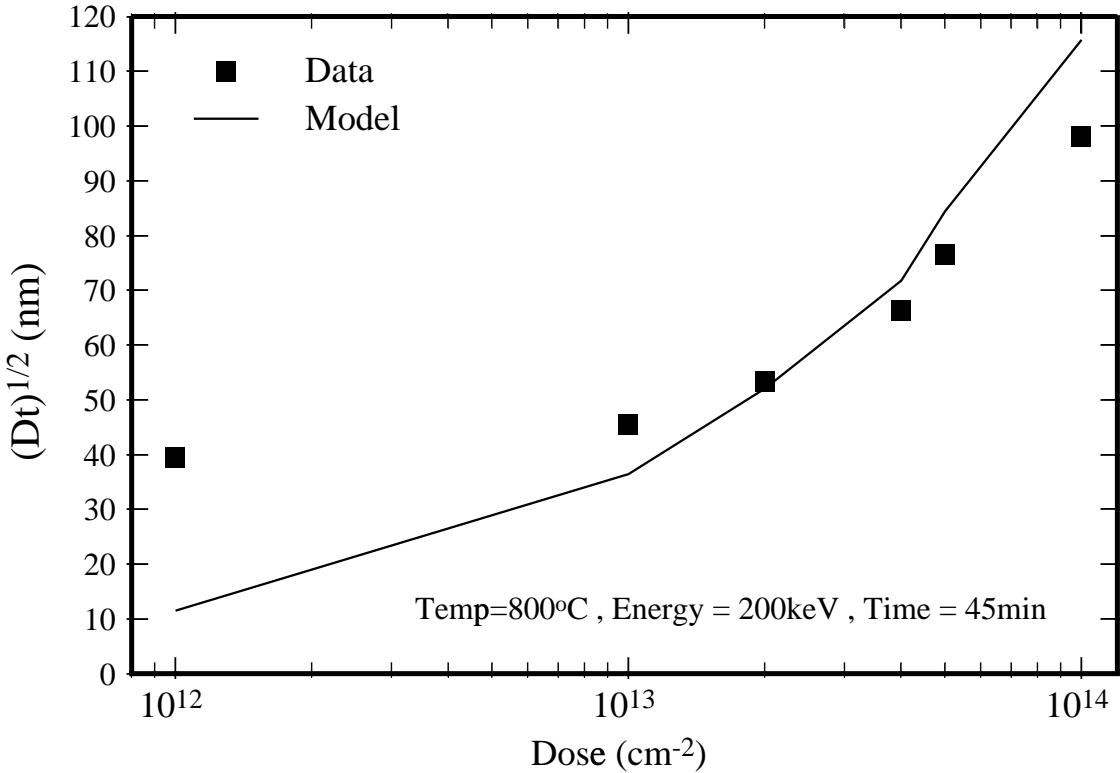
Figure 4.11: Dose dependence of TED. Total broadening of a B marker profile due to [29]Si implantation at 200 keV with annealing at 800°C for 45 min.

(SSS) and the analytical model (AKPM). We first review the assumptions of these four models:

- **1-moment model:** In this model we assume that solute atoms above solid solubility precipitate to extended defects with a diffusion limited rate. This model does not account for Ostwald ripening.

- **2-moment model:** We use log-normal distribution of extended defects with fixed z_2. The variables we have are m_0 and m_1.

- **3-moment model:** We use energy minimizing closure assumption with three moments.

- **Analytical model:** We use analytical functions for the reaction rates that depend on average size.

Figure 4.12 shows the comparison of 1-, 2- and 3-moment models to the $\{311\}$ dissolution data from Eaglesham *et al.* [17]. It can be observed that both the 2 and 3-moment models accurately capture the observed behavior. However, the 1-moment model cannot account for the exponential decay in the number of interstitials stored in $\{311\}$ defects, since it neglects Ostwald ripening process, and predicts an approximately linear decay in the number of interstitials stored in $\{311\}$ defects. The exponential decay rate is a result of decreasing super-saturation of interstitials with time, which is, in turn, a result of the ripening of defects.

When we apply AKPM to the same set of data, we find that it also describes the Ostwald ripening process equally well, although the computation time is much smaller (Fig. 4.13 and Fig. 4.14). This

39
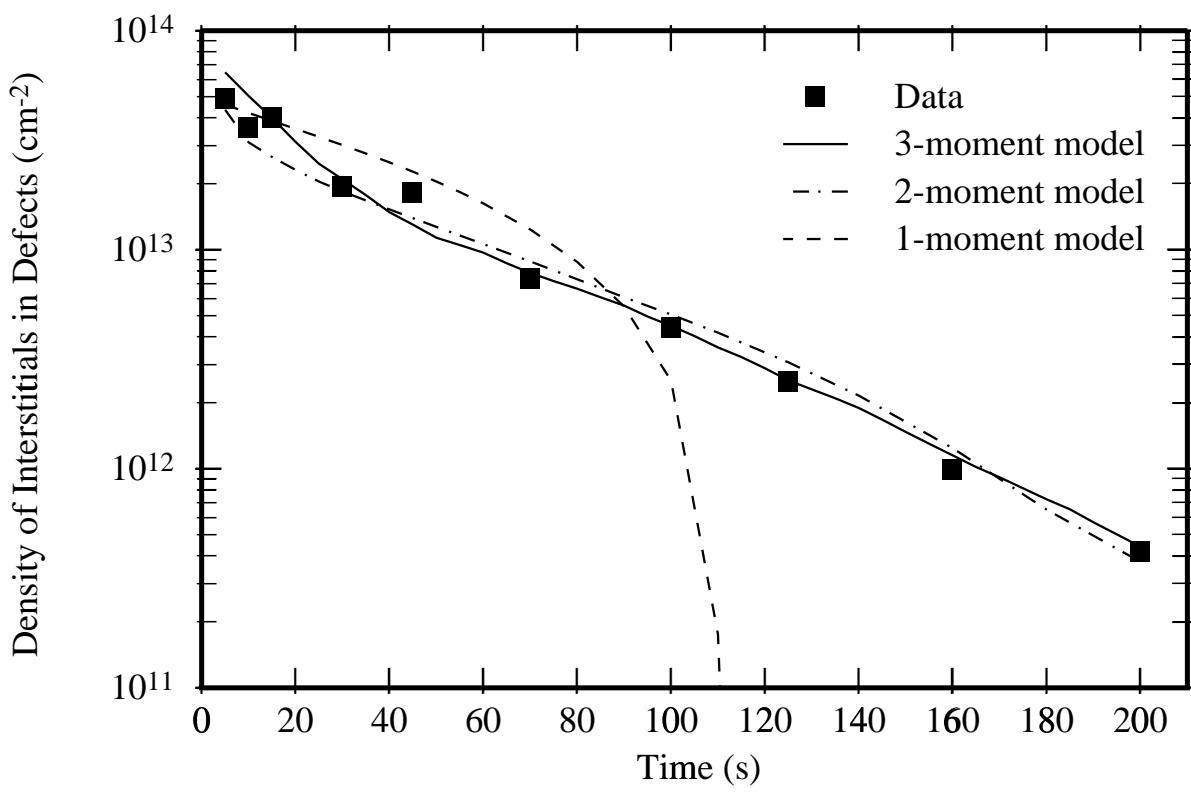
Figure 4.12: Comparison of 1, 2 and 3-moment models for evolution of {311} defects. Both 2 and 3-moment models capture the exponential decay of interstitials in {311} defects.
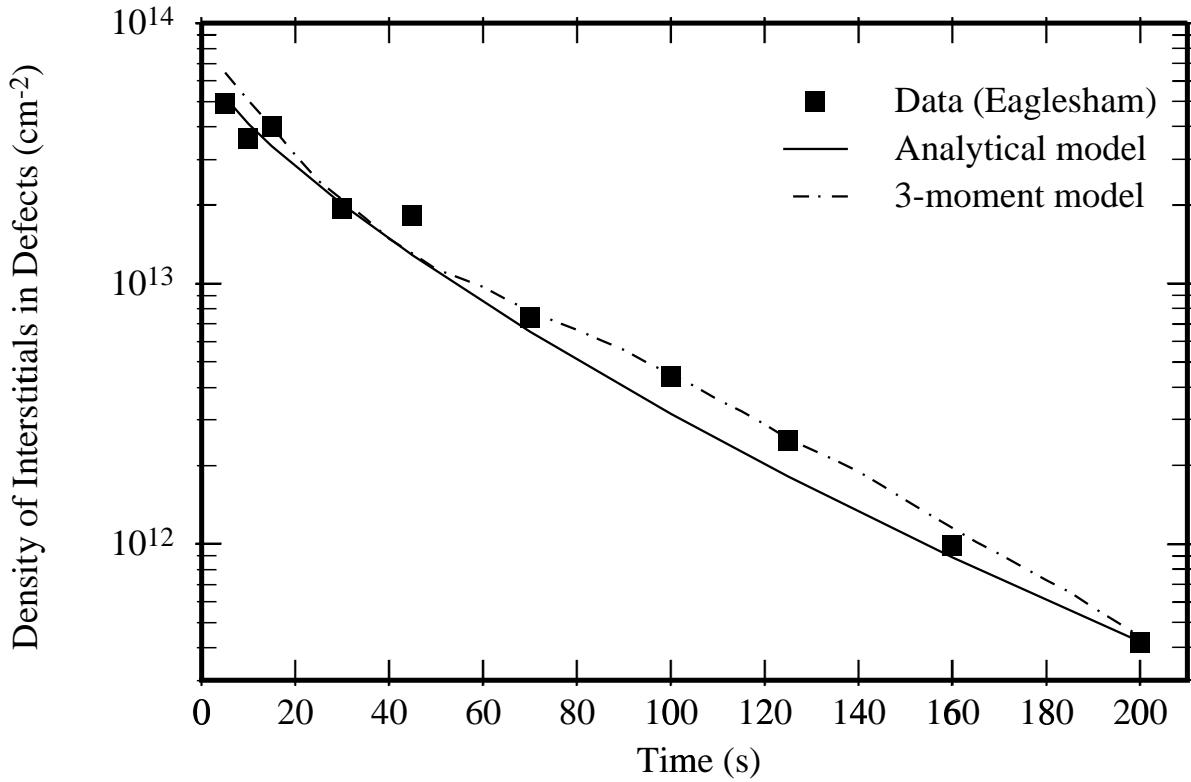
Figure 4.13: Evolution of density of interstitials in {311} defects (m_1) and comparison to analytical model (AKPM) and 3-moment model (3KPM).
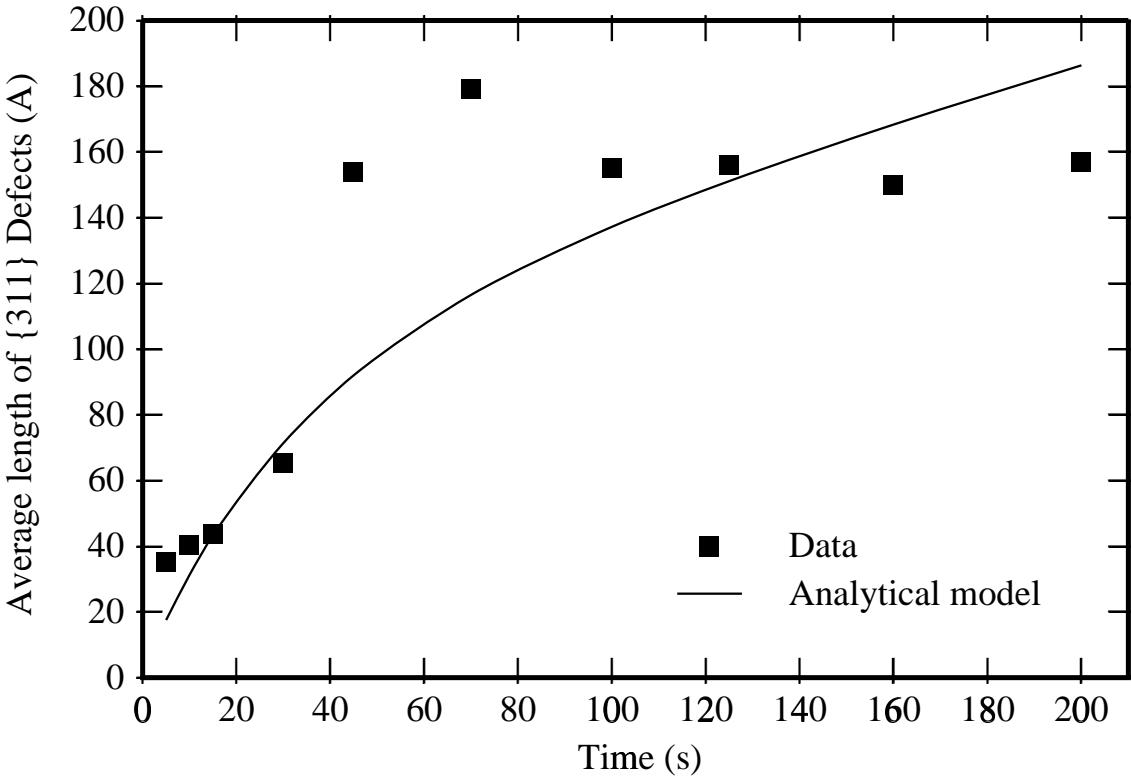
Figure 4.14: Evolution of the average length of {311} defects and comparison to analytical model (AKPM).

makes the AKPM model of choice for simulation of {311} defects in large systems. The fact that AKPM doesn't require any proprietary operators enables easy integration to many PDE solvers.

If we look at TED data from Packan [39], the differences between the three models is relatively small (Fig. 4.15). One can readily observe that the final amount of TED predicted by all three models is approximately the same. This is due to the fact that the final amount of TED is not dependent on how the interstitial super-saturation evolves over time, but rather on effectiveness of the surface in consuming interstitials. Only at short times does there seem to be a significant difference between the models. If we look at short time behavior more closely, the difference between the models becomes more evident (Fig. 4.16). The 1-moment model predicts a constant enhancement of diffusivity until TED is over, whereas the 2-moment model accounts for the reduction of diffusivity enhancement — or interstitial super-saturation — during TED. Again, this is an effect caused by the Ostwald ripening process.

4.4 Effect of "$+n$" factor

Let's investigate the differences between using a "$+1$" model for initial damage, and the more rigorous "$+n$" model described in section 2.2.1 using AKPM. Since the "$+n$" model predicts a plus value as high as 10 (Fig. 2.4), we would expect that the TED predictions at lower doses would be would be substantially increased. However, simulations show only a marginal increase (Fig. 4.17). The reason behind this can be understood by investigating the depth profile of the damage (Fig. 2.3). Although the

41

Figure 4.15: Comparison of 1, 2 and 3-moment models for TED predictions. The models differ significantly only at short time behavior, which this data cannot distinguish.

Figure 4.16: Comparison of 1 and 2-moment models for short time diffusivity enhancements. Data from Chao[6] for a 5×10^{13} cm^{-2} 50 keV implant with anneals at 750°C.

42
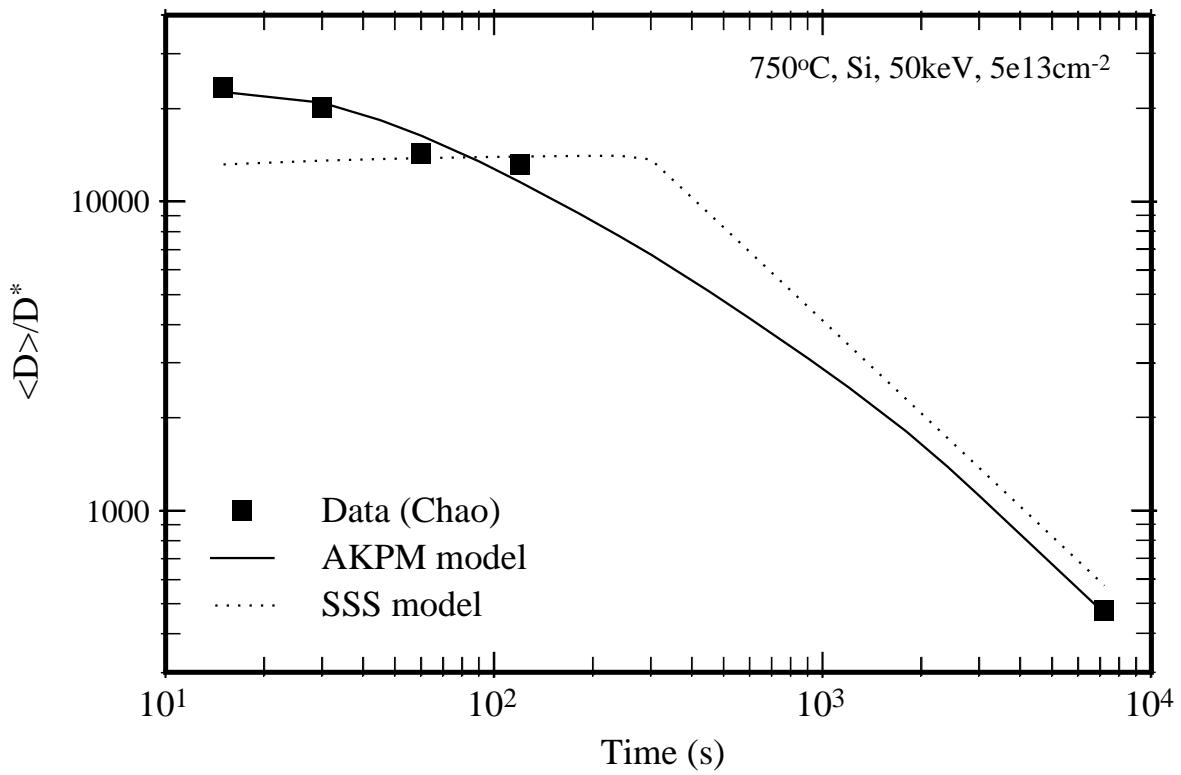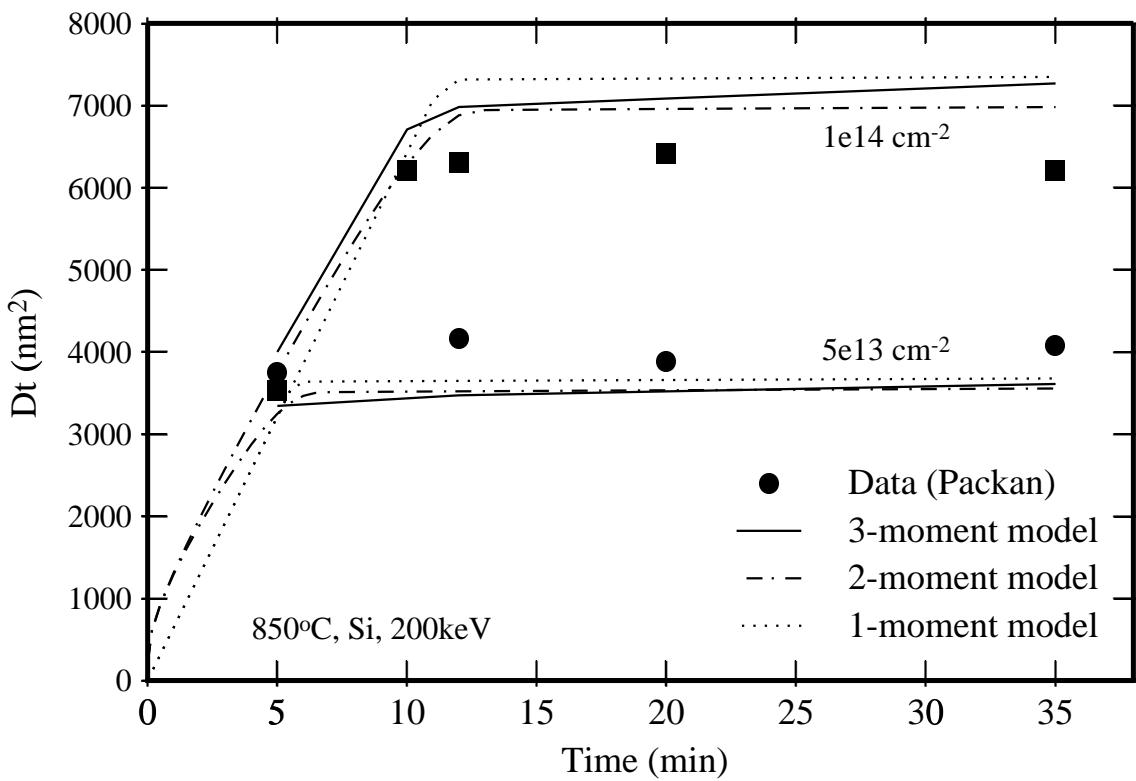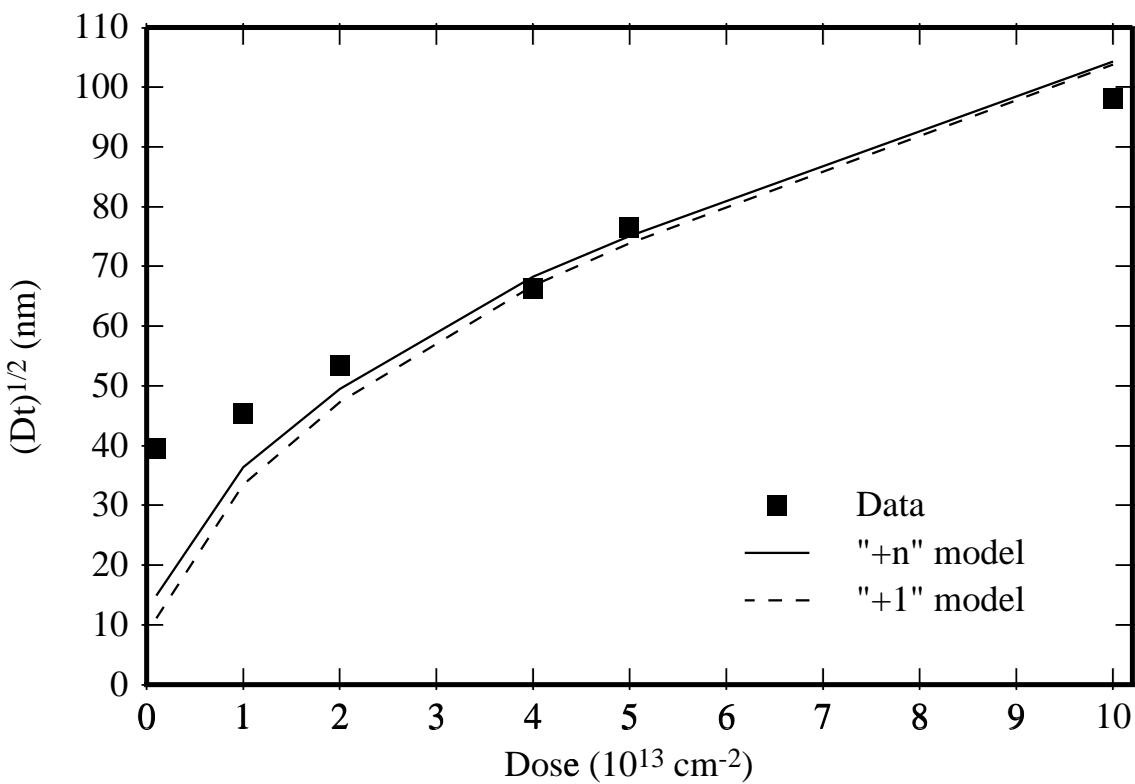
Figure 4.17: Comparison of predictions for the dose dependence of TED using "+1" and "+n" models.

lower implant doses indeed result in a higher plus value, much of this extra interstitial concentration is near the surface, such that it is dissolved very quickly. Therefore, the net effect of this excess damage is minimal.

However, to fully understand the effects, a more rigorous "+n" model has to be developed based on atomistic simulations, which takes diffusion of interstitials and vacancies during annealing into account and also considers factors such as amorphous pocket formation.

4.5 Summary

In summary, we have developed a range of KPM models and tested them for validity and accuracy under different conditions. For the evolution of {311} defects and for TED behavior the difference between the 2 and 3-moment models (2KPM, 3KPM) and the analytical model (AKPM) is negligible. The ordering of models with respect to their computational efficiency is as follows (from most time consuming to least time consuming): 3KPM, 2KPM, AKPM, SSS. For the range of available data, AKPM seems to be the best compromise between computational efficiency and accuracy.

The simple solid solubility model (SSS) is not able to account for the Ostwald ripening process, and thus is unsuitable for modeling of extended defect kinetics and short-time TED behavior. However, it does a good job in predicting the final amount of TED. But the kinetics of {311} defects at the initial stages of TED is important if we have temperature ramps. Depending on the speed of the temperature ramp, we may end up with different amounts of clustered interstitials. The SSS model is

not capable of making this distinction since it doesn't account for Ostwald ripening. Another point where the {311} defect kinetics is important is when we have a competing process, such as boron interstitial cluster (BIC) formation. In such a case, both {311} defects and BICs will compete in capturing the interstitials, and the kinetics become important. With respect to all of these, we won't recommend using SSS model for modeling extended defects.

Chapter 5

Models for Dislocation Loops

5.1 Extending KPM to dislocation loops

Our first approach to modeling of dislocation loops was to extend the KPM model to include dislocation loops in addition to $\{311\}$ defects. We did this by assuming that there are two population of extended defects which can interact with each other. We assumed that for smaller sizes it was energetically more favorable to stay as a $\{311\}$ defect, but above a certain size it was more favorable to transform into a dislocation loop (Fig 5.2). Our simulations gave a cross-over around $n = 2200$. The transfer rate from $\{311\}$ defects into dislocation loops can be expressed as:

$$\frac{D_{\mathrm{I}}}{b^2} \left[f_n^{\{311\}} - f_n^{\mathrm{loop}} \exp\left(-\frac{\Delta G_n^{\{311\}} - \Delta G_n^{\mathrm{loop}}}{kT} \right) \right] \tag{5.1}$$

where b is a "capture distance." We found a value of $20\,\mu\mathrm{m}$ for b. Thus the transfer from $\{311\}$ defects into dislocation loops is a rather slow process.

Pan *et al.* [42] implanted $1 \times 10^{16}\,\mathrm{cm}^{-2}$ Si into silicon at $50\,\mathrm{keV}$ and annealed the samples at $850°\mathrm{C}$ and $1000°\mathrm{C}$. They measured the resulting dislocation loop distributions using TEM. We modeled their data using a similar approach to $\{311\}$ defects. The parameters for $\{311\}$ defects were from previous work [25]. It can be argued that C_{ss} for loops should be just C_{I}^*, since an infinite size perfect loop is nothing but an extra plane in silicon. For partial loops C_{ss} should be slightly higher, but small changes in C_{ss} had no significant effect in our simulation results. Initial damage conditions were obtained as described in Section 2.2.2, where the amorphization threshold has been adjusted to get the correct dose of interstitials in loops.

Our results show that we were able to correctly model the evolution of the system and transformation of $\{311\}$ defects into dislocation loops (Fig. 5.3). We were also able to get the correct Ostwald ripening behavior (Fig. 5.4). Similar matches for data from Lui *et al.* [35] that included longer anneals which led to substantial loop dissolution (Fig. 5.5).

The relatively slow dissolution rate of dislocation loops stems from the facts that they can grow very large and C_{ss} for loops is close to C_{I}^*. This results in C_n^* for loops approaching C_{I}^*, so that they sustain only a small super-saturation of interstitials. Since these loops are deep in the substrate and sustain only a minimal super-saturation, the flux to the surface is small and thus dissolve they slowly.
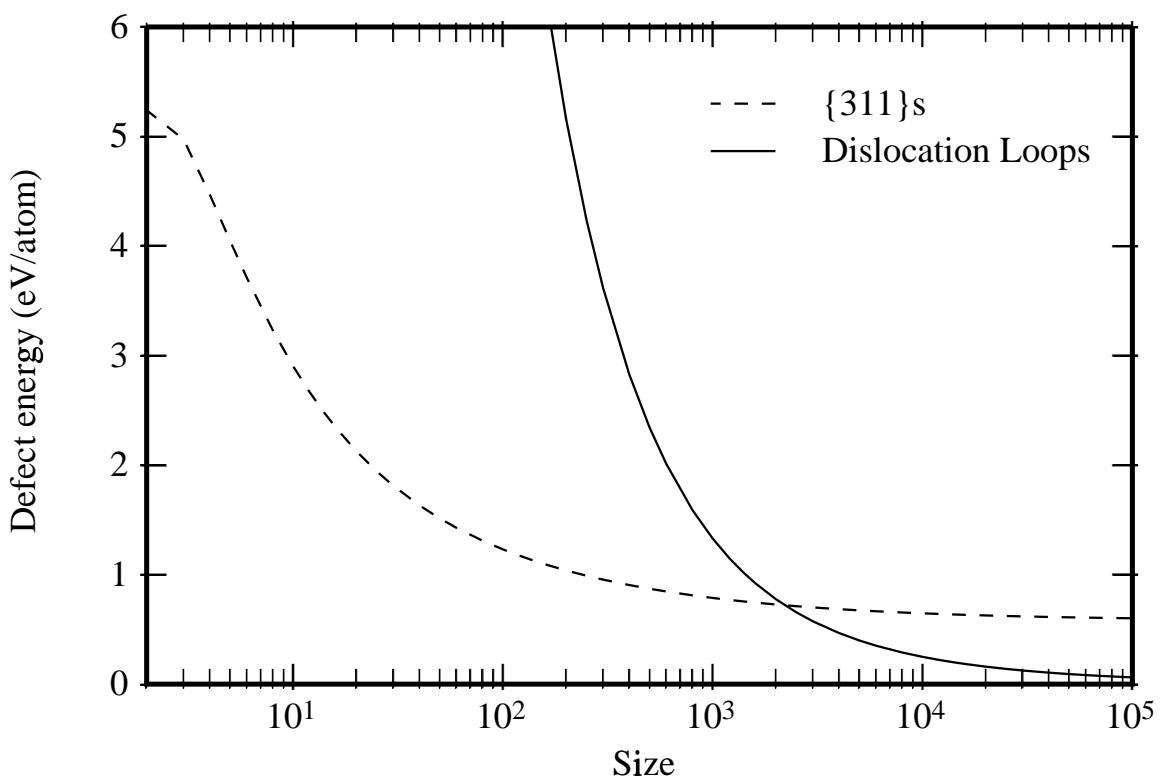
Figure 5.1: {311} defect and dislocation loop energy as a function of defect size. The loops are more stable at larger sizes.
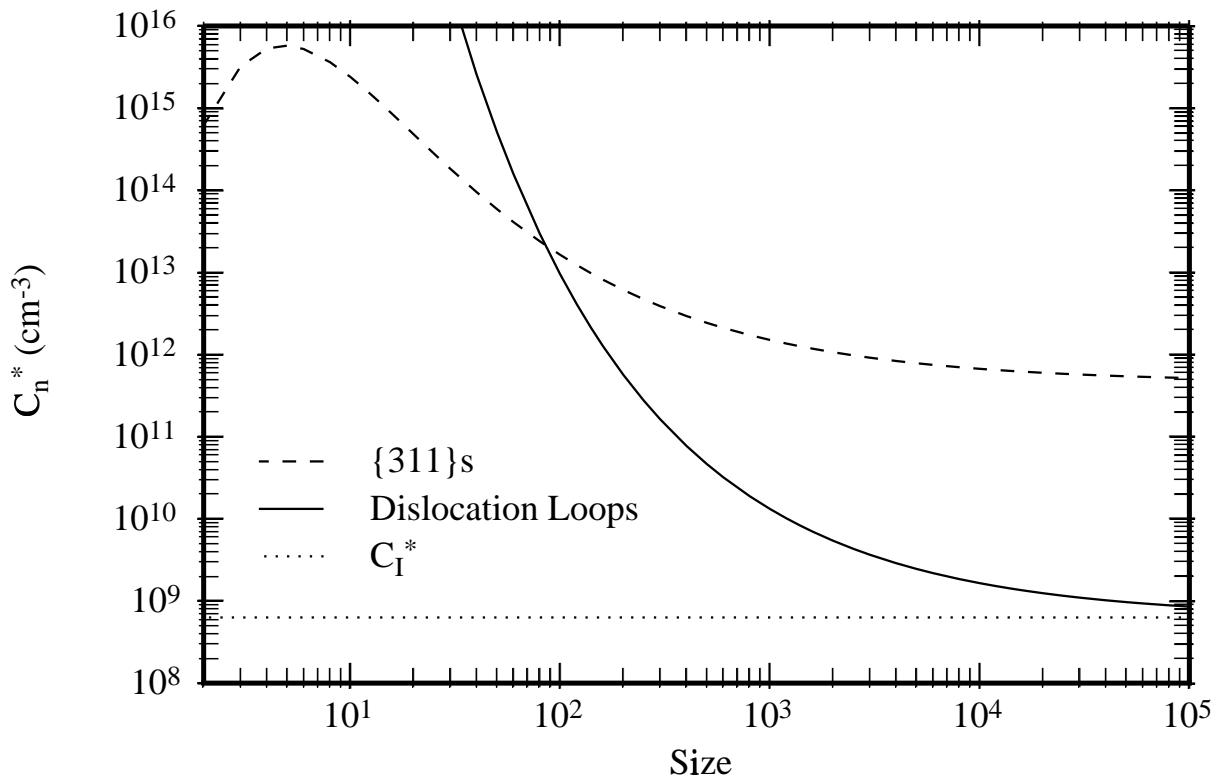
Figure 5.2: {311} defect and dislocation loop C_n^* as a function of defect size.
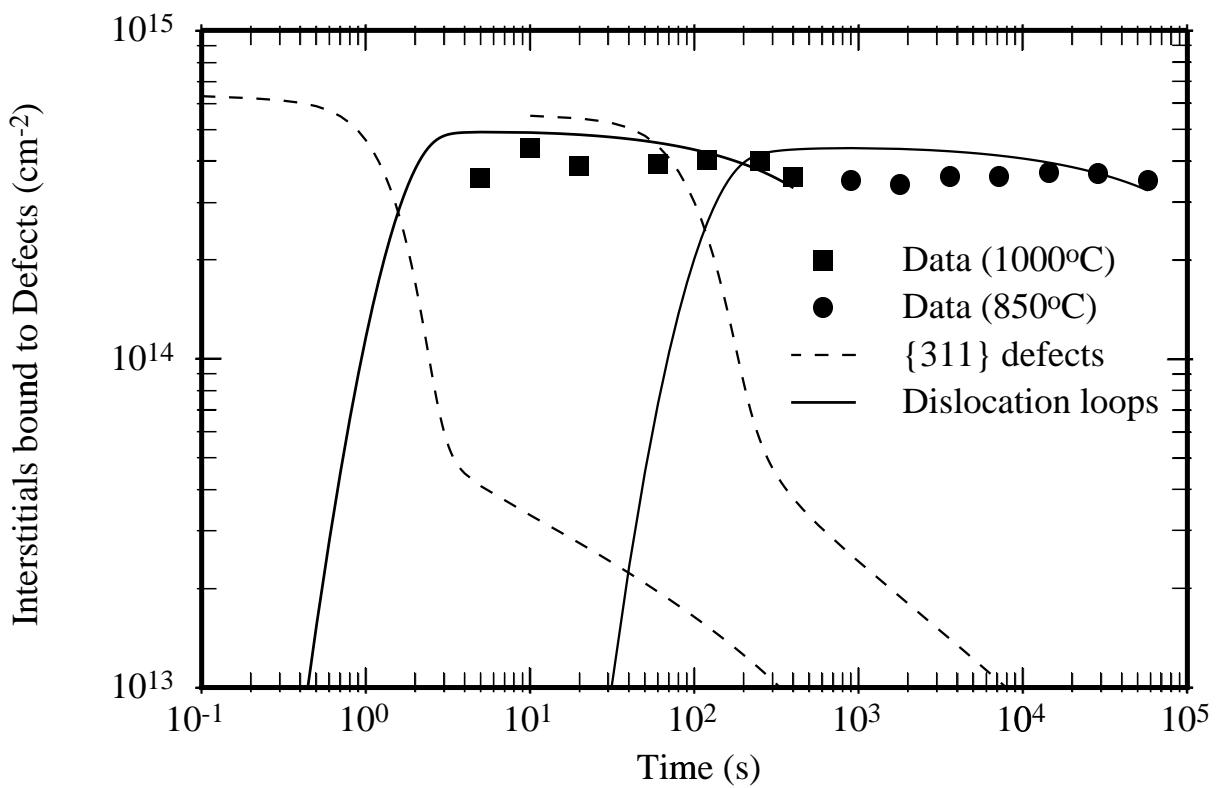
Figure 5.3: Evolution of density of interstitials in extended defects (m_1) and comparison to model. Data from Pan *et al.* [42] for $1 \times 10^{16}\,\text{cm}^{-2}$ Si implant at $50\,\text{keV}$.
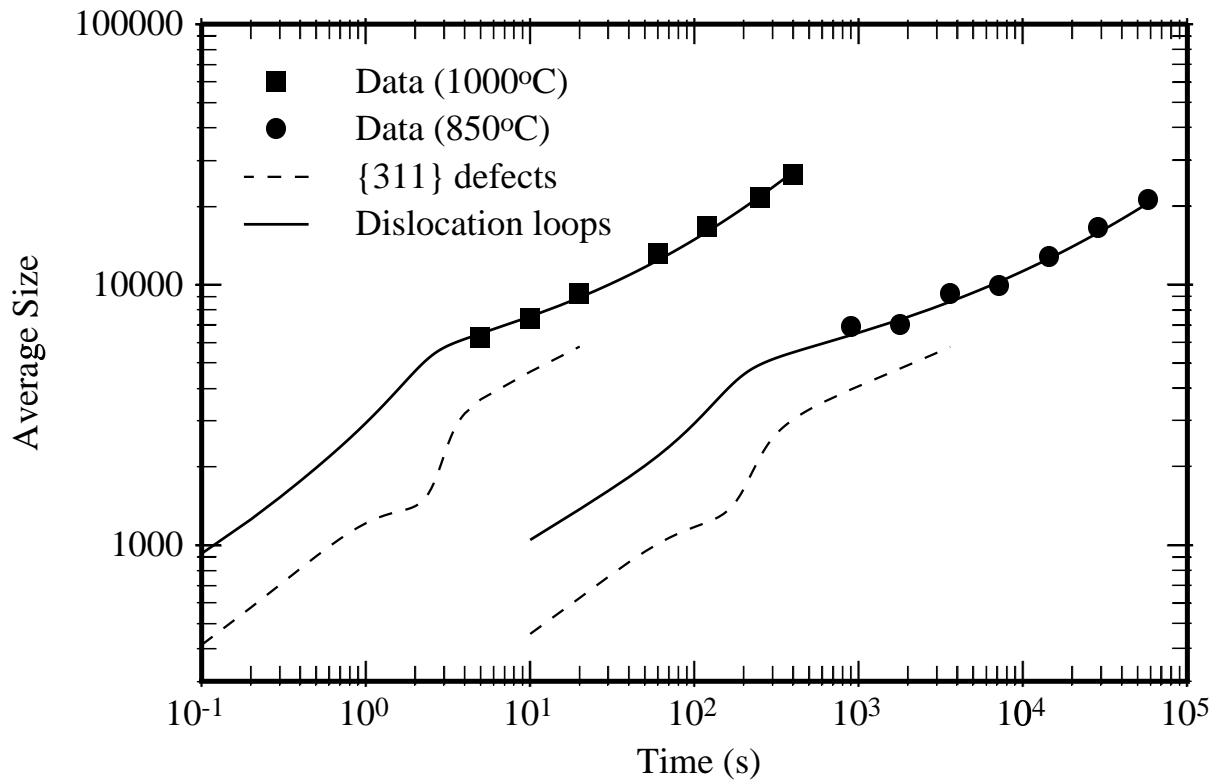
Figure 5.4: Evolution of average defect size (m_1/m_0) for $1 \times 10^{16}\,\text{cm}^{-2}$ Si implants at $50\,\text{keV}$ and comparison to data from Pan *et al.* [42]
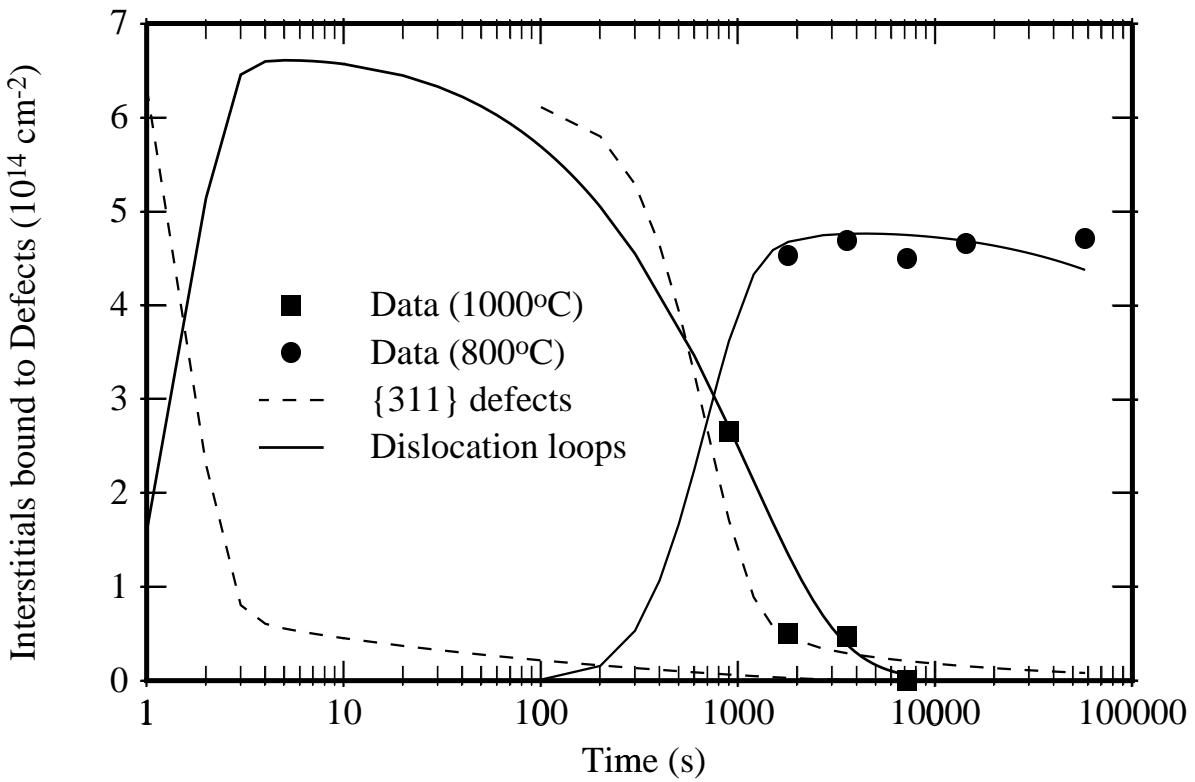
Figure 5.5: Evolution of density of interstitials in dislocation loops (m_1) and comparison to model. Data for $1 \times 10^{15}\,\mathrm{cm}^{-2}$ Si implant at $50\,\mathrm{keV}$.

5.2 Analytical loop model

Although the model presented in the previous section gives good predictions of loop evolution, it is computationally expensive. Therefore, we seek to find an analytical model for loop evolution based on the analytical model for $\{311\}$ defects (AKPM). The approach we take is similar: We assume that $\{311\}$ defects transform into dislocation loops by an unfaulting reaction once they reach a critical size. We can note the following points for the functions that are involved in AKPM:

- Loops have a lower solid solubility than $\{311\}$ defects, typically around C_I^*. Therefore, we have to set the solid solubility of the $\{311\}$ defects/dislocation loop distribution to C_{ss}^{loop}. Since the γ_i are inversely proportional to the solid solubility they have to be multiplied by the difference for smaller sizes.

- To ensure $\lim\limits_{n \leftarrow \infty} \gamma_1 = 1$, we need a functional change after the $\{311\}$/loop crossover point (n_{crit}).

- The γ_i have to be continuous at the $\{311\}$/loop crossover point (n_{crit}).

To understand what type of function this restrictions give, we proceed as earlier: We use ΔG_n^{exc} for dislocation loops (which is identical to ΔG_n^{exc} for $\{311\}$ defects at sizes smaller than n_{crit}), and a log-normal distribution function; and find the corresponding γ_i as we did for $\{311\}$ defects by Eq. 3.17. The results are shown in Fig 5.6, together with analytical functions that capture the behavior of γ_1.

48
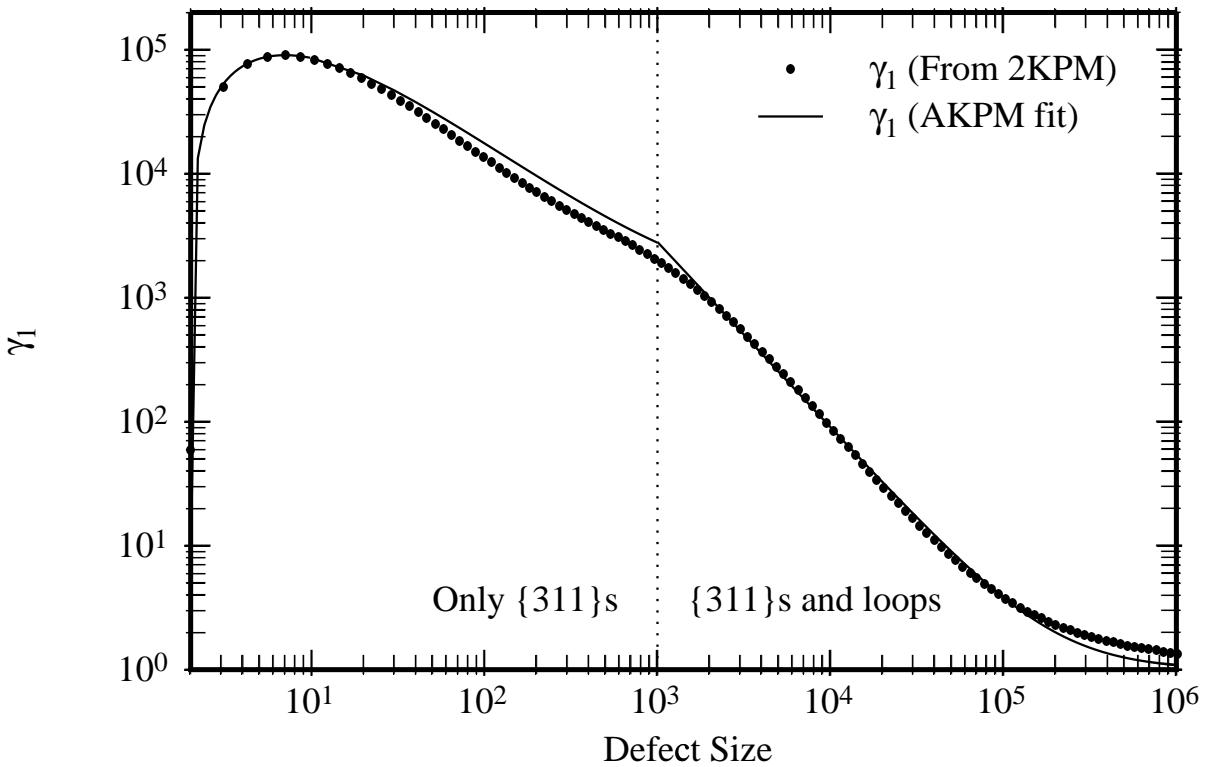
Figure 5.6: The γ_1 function for dislocation loops at as derived from $\Delta G_n^{\mathrm{exc}}$ for dislocation loops and a log-normal closure assumption.

We find a set of γ_i functions to be used with AKPM by extending the set of functions we used for $\{311\}$ defects:

$$
\gamma_0 = \begin{cases} \dfrac{C_{\mathrm{ss}}^{\{311\}}}{C_{\mathrm{ss}}^{\mathrm{loop}}} \dfrac{K_1}{\hat{m}_1 - 1} & \text{for } \hat{m}_1 < n_{\mathrm{crit}} \\[2ex] K_3 \left(\dfrac{1}{\hat{m}_1 - 1}\right)^{\alpha} & \text{for } \hat{m}_1 > n_{\mathrm{crit}} \end{cases}
\tag{5.2}
$$

$$
\gamma_1 = \begin{cases} \dfrac{C_{\mathrm{ss}}^{\{311\}}}{C_{\mathrm{ss}}^{\mathrm{loop}}} \dfrac{\hat{m}_1 - 2}{\hat{m}_1 + K_0} \left(1 + \dfrac{(K_0 + 2)K_2}{\hat{m}_1 + K_0}\right) & \text{for } \hat{m}_1 < n_{\mathrm{crit}} \\[2ex] 1 + K_4 \left(\dfrac{K_0 + 2}{\hat{m}_1 + K_0}\right)^{\alpha} & \text{for } \hat{m}_1 > n_{\mathrm{crit}} \end{cases}
\tag{5.3}
$$

where K_3 and K_4 are chosen such that continuity of γ_0 and γ_1 are ensured (Fig. 5.7). In our simulations, we have used a cross-over point of $n_{\mathrm{crit}} = 1000$ and left α as a fitting parameters. Please note that n_{crit} should not be interpreted as "the point where $\{311\}$ defect to dislocation loop transformation happens," but rather "the size below which no $\{311\}$ defect to dislocation loop transformation happens." The transformation will happen at any size greater than n_{crit}.

We again compare our model against data from Pan *et al.*[42]. As one can readily observe, a good match can be found (Fig. 5.8 and Fig. 5.9). Since this model can't distinguish between the interstitials contained in dislocation loops and the interstitials contained in $\{311\}$ defects, we can't plot them separately. However, to obtain an idea on how the $\{311\}$ defects would evolve, we can turn off the

49
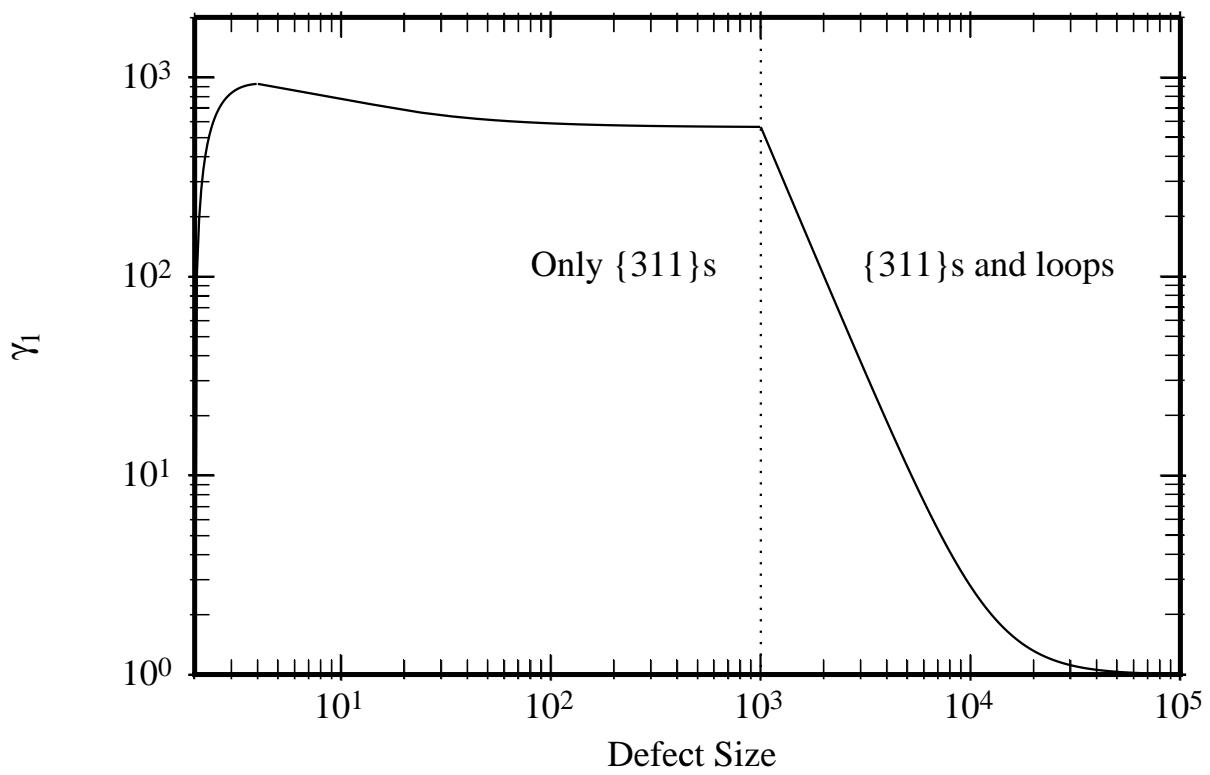
Figure 5.7: The γ_1 function for dislocation loops at 1000°C for the AKPM. For $\hat{m}_1 < n_{\text{crit}}$, γ_1 is identical to that for $\{311\}$ defects, except for a multiplier to account for differences in solid solubility.
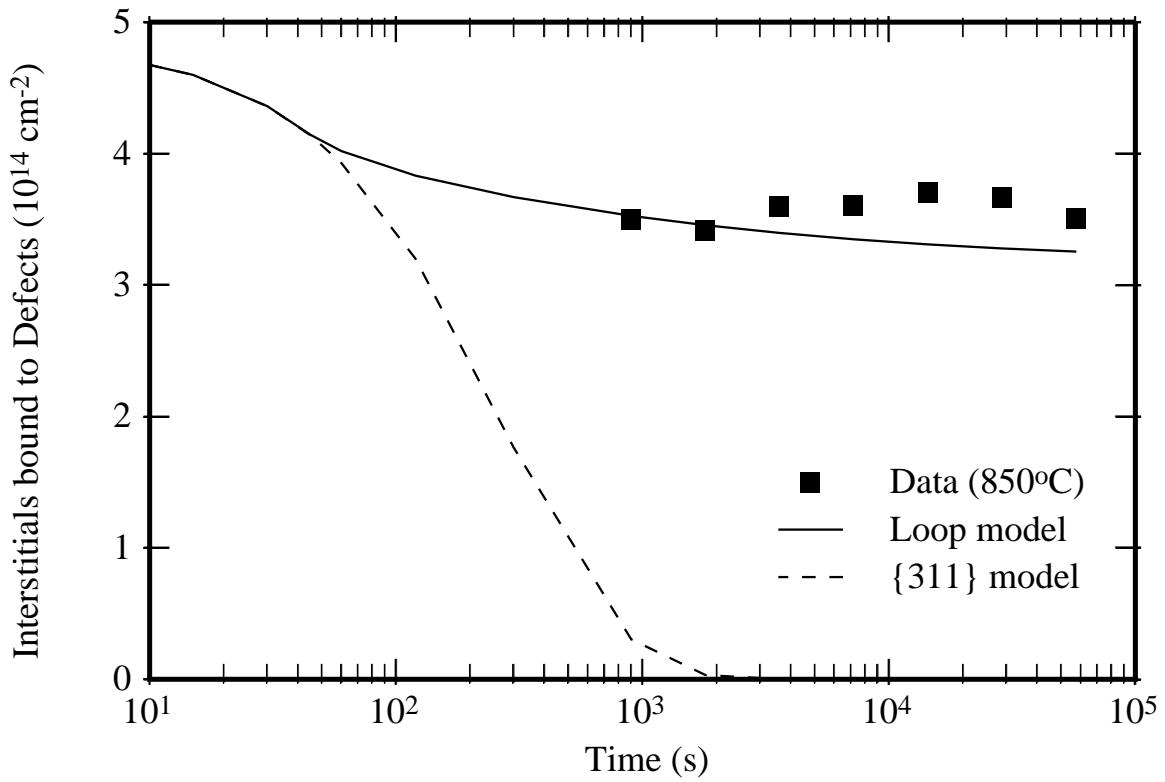
Figure 5.8: Evolution of total number of interstitials stored in dislocation loops and $\{311\}$ defects for the AKPM. Data for $1 \times 10^{16}\,\text{cm}^{-2}$ Si implant at 50 keV with anneal at 850°C.
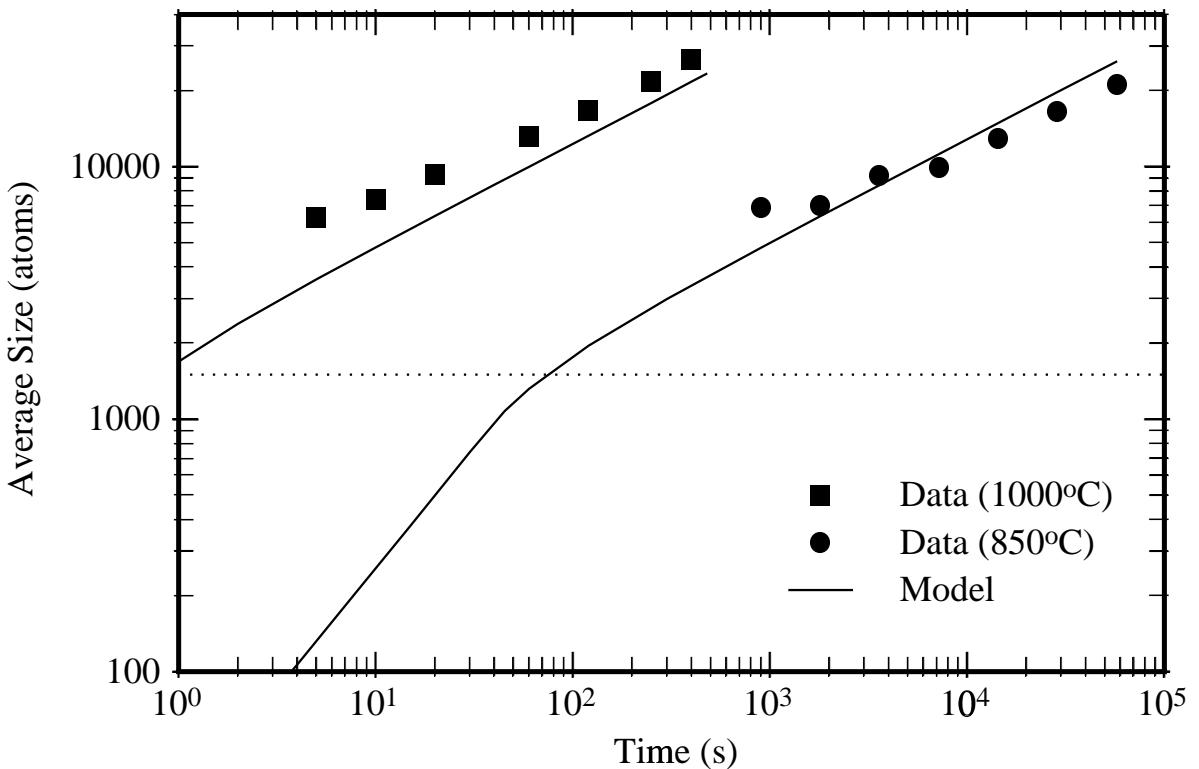
Figure 5.9: Evolution of average defect size for 1×10^{16} cm^{-2} Si implants at 50 keV from AKPM.

loop portion of the model and plot $\{311\}$ defects in the absence of loops (Fig. 5.8). The model also gives a good fit to the Ostwald ripening process of dislocation loops (Fig. 5.9).

5.3 Simulating TED

We have applied our loop model to TED conditions to predict dopant movement of a buried marker layer due to an amorphizing implant. To this end, we have used data from Chao [6] and Huang [32]. Chao also had data for non-amorphizing implants, and for those implants the model predicts that dislocation loops will never form in agreement with experiment.

Our results show that we were able to predict TED behavior over a large range of implant doses (Fig. 5.10). Although the fact that a 1×10^{15} cm^{-2} implant causes less TED than a 1×10^{14} cm^{-2} implant may seems a little paradoxical in the first look, it is very reasonable when we consider that most of the implant damage anneals out by epitaxial regrowth for amorphizing implants.

5.4 Modeling heterogeneous nucleation

The model we demonstrated in the preceding sections assumed that the sole mechanism of dislocation loop formation was through transformation from $\{311\}$ defects, and that the $\{311\}$ defects grow to a certain size (n_{crit}), after which it becomes energetically favorable to transform into a dislocation loop. Moreover, we assumed that the nucleation of $\{311\}$ defects, and hence formation of dislocation

51
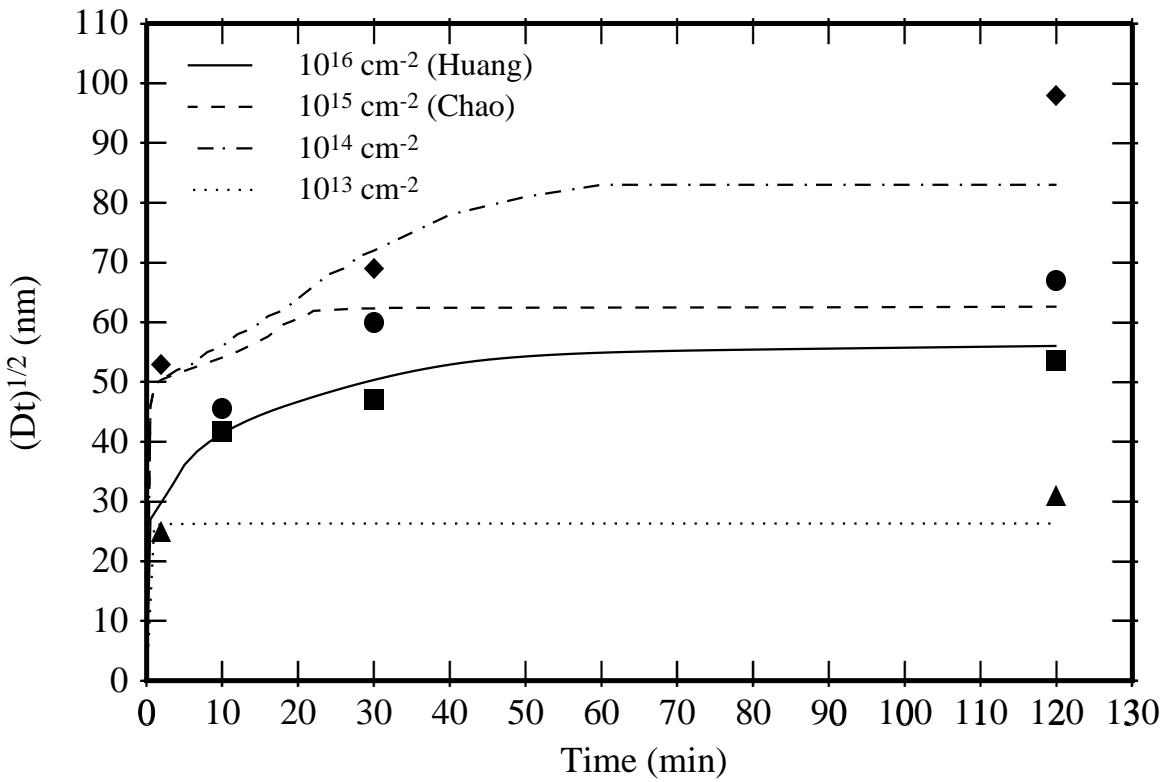
Figure 5.10: Prediction of TED using FKPM for amorphizing and non-amorphizing implants. Data for 50 keV Si implants with annealing at 750°C.

loops is a *homogeneous* process. That is, in the wafer, there is no preferred site for {311} defect/loop formation and these defects will form anywhere when there is enough driving force to form these defects.

However, experimental observations by Pan *et al.* revealed that after annealing an amorphizing implant, there exists also loops that are in size much smaller n_{crit} [41]. Although our previous model doesn't rule out this possibility, it is very unlikely that a small {311} defect will transform into a dislocation loop since it is energetically unfavorable. Pan *et al.* concluded that these loops must have nucleated directly from the matrix.

But why do we observe loops that nucleate directly without {311} defects if we have an amorphizing implant, and observe only {311} defects if we have a non-amorphizing implant? The answer may be *heterogeneous nucleation* with the amorphous / crystalline interface acting as a nucleation site for dislocation loops. Therefore, we can have dislocation loops that are much smaller than {311} defects, since they have formed by nucleation assisted by the amorphous/crystalline interface.

We now seek ways to extend our model to include this capability. One way of accomplishing this goal is to have two separate distributions of extended defects. The first distribution would be the distribution for {311} defects and dislocation loops that were formed by transformation from {311} defects, which is the distribution we considered in previous section. The second distribution would be for dislocation loops that formed heterogeneously at the amorphous/crystalline interface. We can deal with the heterogeneous nature of the second distribution by lowering the formation energy of these extended defects around the amorphous/crystalline interface. A simple way of achieving this goal is depicted in Fig 5.11. Since we can't see small size defects, the determination of how $\Delta G_n^{\mathrm{exc}}$,
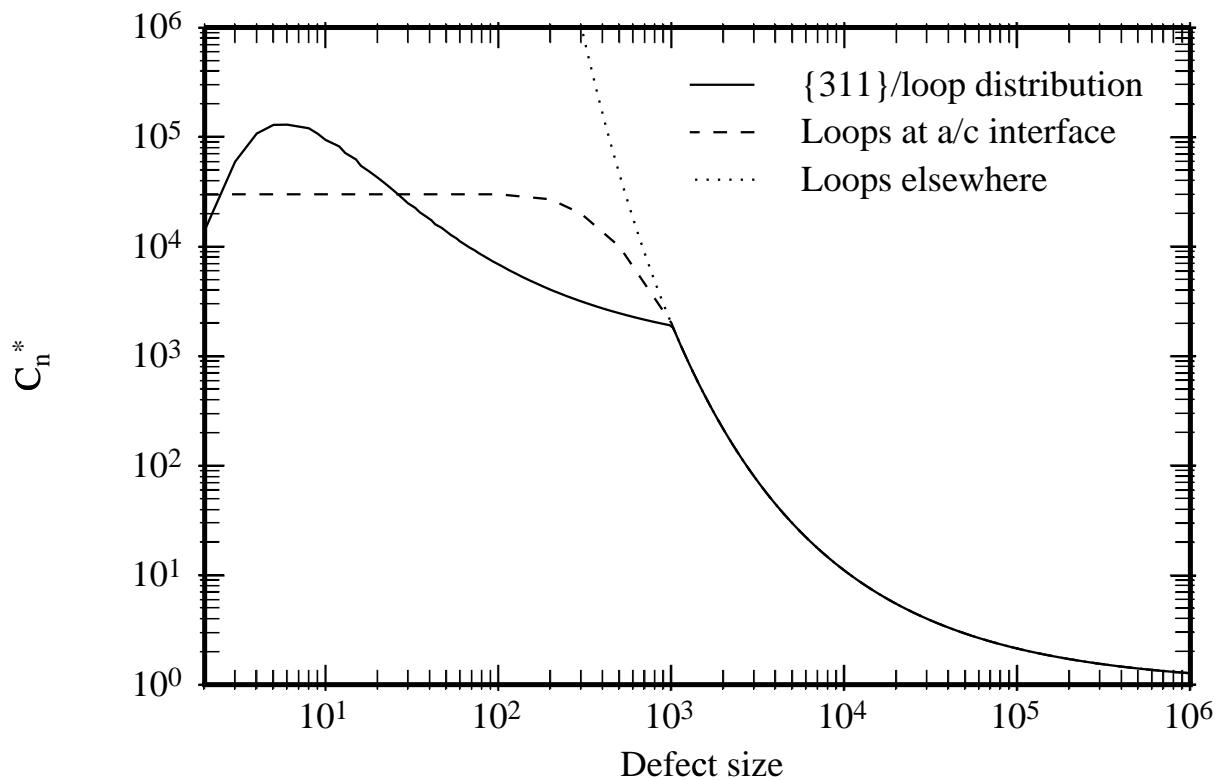
Figure 5.11: Distribution of C_n^* for heterogeneous nucleation. Note that C_n^* will be different for the pure loop distribution based on spatial location.

and hence C_n^* looks like at small sizes will have to depend heavily on atomistic calculations.

One issue here is the "thickness" of the heterogeneous nucleation region. An initial approximation could be the roughness of a/c interface. However, the regions where this nucleation effects the point defect concentrations can grow to the maximum loop size.

5.5 Summary

In summary, we were able to model the formation and evolution of dislocation loops by extending our model for {311} defects to a system with two distributions and accounting for the transfer between {311} defects and dislocation loops. We also developed a computationally efficient version of this model, based on AKPM.

The loop model extends our TED prediction capability to amorphizing doses. We were able to obtain good TED predictions for a large range of implant doses.

Chapter 6

Software Development Efforts

In order to carry out the simulations described in the preceding chapters, we have developed a multi-purpose partial differential equation solver, DOPDEES, which is capable of solving initial value problems in one spatial dimension using a finite differences method. The system of partial differential equations is specified using a "dial-an-operator" paradigm, and the program uses Tcl (a re-usable and extendible command language developed at UC Berkeley [38, 54]) as a front end. DOPDEES has commands for structure generation and modification, as well as features that make simulation of time-varying parameters (e.g. temperature ramps) possible. The solver is fast and suitable for use as a process simulator and model test bed in 1-D.

Process Modeling Modules (PMM) is a framework for platform-independent scriptization of commonly encountered models in the process modeling community. PMM frees the user from the burden of specifying all equations and parameters for commonly known models, but still retains the power to specify arbitrary equations and models. It also provides a framework for transferring models directly from the university to the industry, without the need for a vendor to implement those models in a commercial process simulator.

6.1   DOPDEES

The shrinking dimensions of VLSI devices leads to more complex phenomena becoming important during fabrication. This requires a flexible environment for developing process models. The system should not restrict the user to predefined models, but rather should enable implementation of any system of continuum equations. DOPDEES is such an effort.

DOPDEES is a multi-purpose PDE initial value solver in one spatial dimension that uses a "dial-an-operator" paradigm for specification of the equation system [37]. The primary aim of the code is rapid development of continuum models and it may be used for a variety of systems. It is intended to be easy to use and easy to extend with new operators.

DOPDEES can be used in any system where the user wants to obtain solutions for coupled partial differential equations (PDEs). The program was originally written to solve diffusion/reaction problems and this is why it comes with operators suited for such systems. However, if the operators or functions the user needs are not included, it is relatively easy to add them. Another positive feature is that the user is able to select the integration engine, as different systems benefit from different nu-
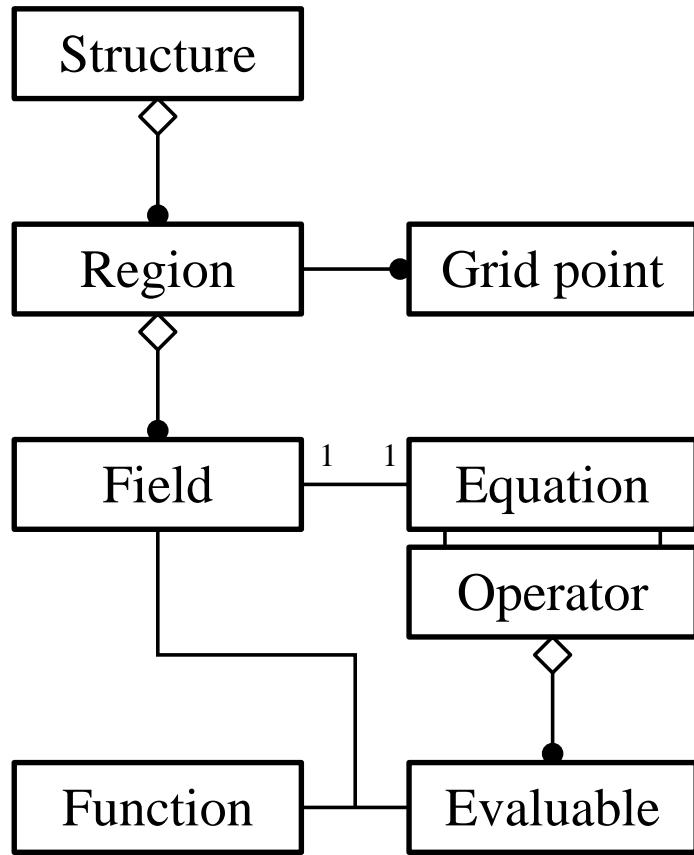
Figure 6.1: A structure in DOPDEES consists of regions, which each have a number of fields (solution variables) and a grid structure. Each field is associated with an equation of the type $\partial f / \partial t = \sum \mathrm{op}_i$.

merical algorithms which associated trade-offs in speed and stability. There are also commands for grid generation and result extraction. The user interface of DOPDEES is in Tcl, which provides for powerful input scripting.

DOPDEES solves a given set of partial differential equations. The (one dimensional) space is assumed to be divided into chunks called *regions*, and it is assumed that different equations need to be solved in different regions (Fig 6.1). The solution variables are called *fields*, and it is assumed that for all fields equations of the type $\partial f / \partial t = \ldots$ exist that describe the PDEs. A field specified in one region doesn't exist in others, unless explicitly specified. Actually, the only communication between regions happens through boundary transfers.

The right hand sides of the partial differential equations are specified as a sum of *operators*: $\partial f / \partial t = \sum \mathrm{op}_i$ This approach is called *dial-an-operator*, since the user can choose the operators on the right hand side. The operators can make use of *functions*, which can be defined in terms of fields and defined parameters as well as other functions.

DOPDEES actually discretizes the user-specified partial differential equations and then solves the resulting set of ordinary differential equations (ODE) using a standard ODE solver, or solver "engine" (Fig. 6.2). This considerably reduces the code development time, while the use of well-known, bug-free code leads to stability in the program.

DOPDEES supports time-varying parameters, which enables the user to simulate systems like
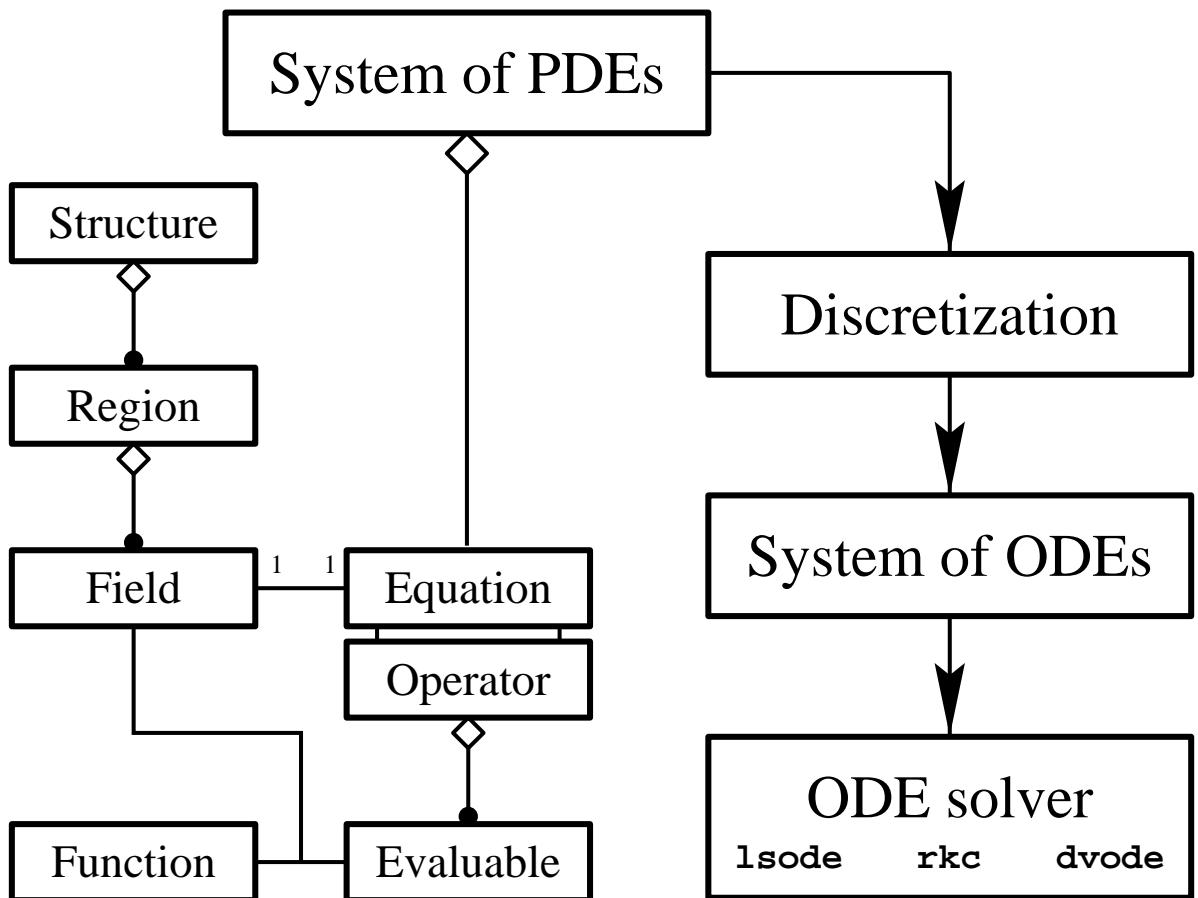
Figure 6.2: DOPDEES handles PDEs by discretizing them using finite differences and feeding them into a standard ODE solver.

temperature ramps. The parameters and fields are handled alike using the same functions, the only difference being that a parameter is a single valued quantity in a region, whereas fields have different values at each spatial grid point. When functions are defined, the resulting quantity is single valued if all arguments are single valued, otherwise it is assumed to be multi-valued. This eliminates the need for writing separate functions for parameters and fields, but still leads to efficient execution.

6.2   Process Modeling Modules (PMM)

The concept of Process Modeling Modules (PMM) developed from our realization that there was a gap to be filled between a process modeling software like SUPREM and a partial differential equation (PDE) solver like DOPDEES or Àlamode. Process simulators are not flexible enough to provide choice over the equations to be solved for; they are hard-coded and user control is limited to a fixed set of models and parameter values. On the other hand, when using a general PDE solver, it is necessary to specify every single equation and parameter in all input decks, even if some of the equations and parameters are considered to be well-known. In addition to the overhead involved, this may also lead to inconsistencies between users, or groups of users.

Thus, one form of software provides almost no flexibility, while the other requires the same work to be done over and over, often leading to errors. We attack this dilemma by writing reusable *modules* that can be incorporated into input decks of PDE solvers. This approach retains the flexibility of a PDE solver, while providing reasonable defaults for models and parameters.

Several standard models have been implemented in PMM, as well as many models that have been developed at Boston University. Fig 6.3 shows available models as well as their interdependencies. PMM (Process Modeling Modules) uses a hierarchical model description, such that models can include other models, and ensures inter-operability of models by consistency checks. Currently, PMM includes a collection of modules frequently encountered in VLSI process modeling:

- Dopant diffusion, simple and coupled with point defects.

- Point defect diffusion, generation and recombination.

- Dopant-dopant pairing.

- Two-stream diffusion in polysilicon.

- Clustering of point defects and precipitation of dopants.

PMM model descriptions are independent of the PDE solver used, thus providing a mechanism for transfer of models between simulation packages. In addition to DOPDEES, PMM has been interfaced with the Àlamode solver [55], which is part of the SUPREM OO7 system. We have also published a white paper describing the common scripting platform [56]. The TCAD software vendor Avant! Corp. shows an effort to integrate PMM with their new process simulator. We believe that the use of the PMM concept will speed model development and facilitate transfer of those models between groups of users. The most direct impact would be rapid transfer of models from university research groups to industry, without the need to wait for implementation by commercial software vendors.
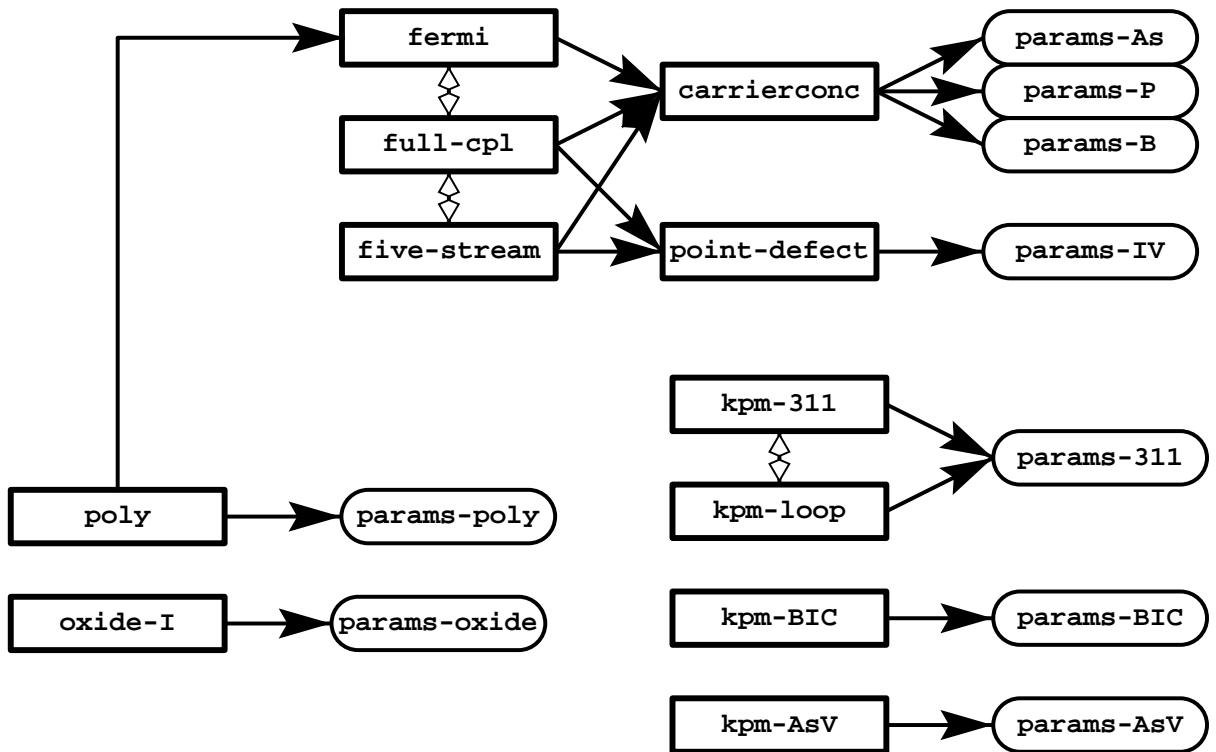
Figure 6.3: Models implemented in PMM and their interdependencies. Modules can inherit parameters from lower level modules and do consistency checks.

6.3 Simulation of dopant diffusion

As an example we will consider diffusion of two dopants, boron and arsenic, in silicon. The diffusivity of both boron and arsenic are dependent on the local Fermi level, and therefore they can affect each others diffusion through the net dopant concentration. At high concentrations, arsenic is know to become immobile and electrically inactive. We will consider a simple model where the effect of point defect interactions is not taken into account (the Fermi model) and the deactivation of arsenic is assumed to happen abruptly above the solid solubility. More rigorous models exists both for diffusion and deactivation and have been implemented in DOPDEES/PMM framework. Under conditions where the point defect concentrations are close to their equilibrium values, this model should provide reasonable results.

The set of PDEs in our system can be formulated as follows:

$$\frac{\partial C_{\mathrm{B}}}{\partial t} = \vec{\nabla} D_{\mathrm{B}} \left(\vec{\nabla} C_{\mathrm{B}} - C_{\mathrm{B}} \vec{\nabla} \ln(n/n_i) \right) \tag{6.1}$$

$$\frac{\partial C_{\mathrm{As}}}{\partial t} = \vec{\nabla} D_{\mathrm{As}} \left(\vec{\nabla} C_{\mathrm{As}}^{\mathrm{act}} + C_{\mathrm{As}}^{\mathrm{act}} \vec{\nabla} \ln(n/n_i) \right) \tag{6.2}$$

$$C_{\mathrm{As}}^{\mathrm{act}} = \min(C_{\mathrm{As}}, C_{\mathrm{ss}}) \tag{6.3}$$

$$\frac{n}{n_i} = \left(\frac{C_{\mathrm{As}}^{\mathrm{act}} - C_{\mathrm{B}}}{2n_i} \right) + \sqrt{\left(\frac{C_{\mathrm{As}}^{\mathrm{act}} - C_{\mathrm{B}}}{2n_i} \right)^2 + 1} \tag{6.4}$$

58

The diffusivities of boron and arsenic are assumed to depend on n/n_i in a standard manner. In addition to the silicon region, we also have an oxide region on top of the structure and boron is assumed to segregate preferentially to the oxide. Figure 6.4 shows the script used in DOPDEES for model definition. Note that the operators need to specify to which field (i.e., equation) they belong to. Using PMM greatly simplifies the input file since it calls the pre-defined Fermi module (Fig. 6.5). Note that the user can still specify an arbitrary set of PDEs, for this case PDEs for boron segregation to and diffusion in the oxide, when using PMM modules. This ensures maximum flexibility while simplifying the input. Figure 6.6 shows the initial and final doping profiles in the structure.

```
set TEMPK [unit 900 C]

# Silicon atom concentration
set CSi [unit 5e22 cm-3]
# "Average" lattice spacing in Si
set ASi [expr pow($CSi,-0.333333)]

# Define operators
region select Oxide

# Diffusion of boron in oxide
set DB_Ox [arrhenius 1.83e-2 3.82 cm2/s]
op diff CB $DB_Ox CB

region select Silicon

# Active arsenic concentration
set CSS_As [arrhenius 2.22e22 0.47 cm-3]
set CAs_act [func min CAs $CSS_As]

# Carrier concentration in silicon
set NI [arrhenius [expr 3.9e16*pow($TEMPK,1.5)] 0.605 cm-3]
set nni [func carrierconc [func sum $CAs_act [func prod -1 CB]] $NI]

# Diffusion of boron in Silicon
set DB_0 [arrhenius 0.037 3.46 cm2/s]
set DB_P [arrhenius 0.76  3.46 cm2/s]
set DB [func diffusivity $nni $DB_0 0 $DB_P 0]
op diff CB $DB CB

# Drift of boron
op diff CB [func prod -1 $DB CB] [func log $nni]

# Diffusion of arsenic
set DAs_0 [arrhenius 0.0666 3.44 cm2/s]
set DAs_M [arrhenius 12.8 4.05 cm2/s]
set DAs [func diffusivity $nni $DAs_0 $DAs_M 0 0]
op diff CAs $DAs $CAs_act

# Drift of arsenic
op diff CAs [func prod $DAs $CAs_act] [func log $nni]

# Segregate boron to the oxide
set mseg [arrhenius 1126 0.91]
set Ktr [func div [func sum $DB_0 $DB_P] $ASi]
op transfer Oxide CB CB [func div CB $mseg] CB $Ktr

# Run the simulator.
solver run 0 [unit 30 min]
```

Figure 6.4: DOPDEES input script for the solving the equation system for co-diffusion of boron and arsenic.

```
set TEMPK [unit 900 C]

# Define operators
region select Oxide

# Diffusion of boron in oxide
set DB_Ox [arrhenius 1.83e-2 3.82 cm2/s]
op diff CB $DB_Ox CB

region select Silicon

module fermi -sss -suprem -debug

# Segregate boron to the oxide
set mseg [arrhenius 1126 0.91]
set Ktr [func div [func sum $D(B,0) $D(B,P)] $ASi]
op transfer Oxide CB CB [func div CB $mseg] CB $Ktr

# Run the simulator.
solver run 0 [unit 30 min]
```

Figure 6.5: DOPDEES input script for the solving the same equation system, but with the Fermi model implemented using a PMM script.
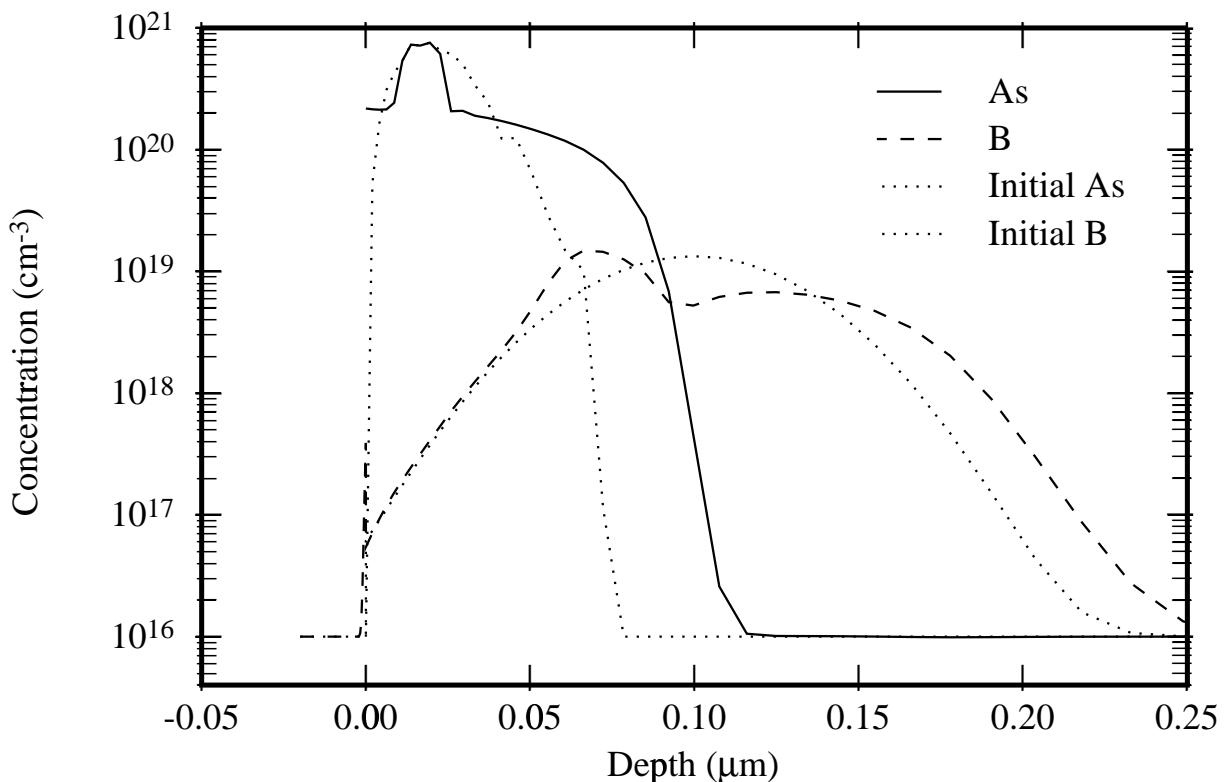
Figure 6.6: The initial dopant profiles and final profiles after a 30 min anneal at 900°C according to simulation using the Fermi model.

Chapter 7

Summary and Future Directions

7.1 Modeling and experiments

Our aim in this work was to understand the physical processes occurring under Transient Enhanced Diffusion (TED) conditions, express them in a mathematical model, integrate this model into a diffusion equation solver and quantitatively match the experimental observations.

To this end, we have developed a solid physical model (KPM) for the evolution of extended defects ({311} defects and dislocation loops) which are observed under TED conditions. We have also developed different versions of KPM that have applicability under different circumstances, and have an associated range of computational efficiency. The full set of models developed in this work gives the user the ability to make appropriate trade-offs between accuracy and computational time.

We have applied KPM to {311} defects that are observed under non-amorphizing implant conditions and we were able to get a good agreement with the available experimental data. We have then used this model to predict TED behavior based on marker layer experiments and we found good agreement for the magnitude of TED, as well as the time energy and dose dependence. To extend the model to dislocation loops, we assumed that dislocation loops form by unfaulting of {311} defects as observed experimentally. We accounted for this transformation in our model and we were able to obtain a good match to the experimental data without any modifications in the {311} defect model. We also indicated how the same model could be used for heterogeneous nucleation.

Note that we have only dealt with silicon implants and marker layer experiments in this work. A natural extension of our work is to extend it to dopant implants, which are used for making real devices. One of the phenomena that becomes important under these conditions is the decreased solid solubility of boron, which has been attributed to formation of boron-interstitial clusters (BICs). Modeling BICs with a comprehensive, yet computationally efficient model remains still a challenge at this point, although several researchers have made substantial progress in this field in recent years.

One important fact is that the TED predictions strongly depend on point defect properties, especially the $D_I C_I^*$ product. All the results obtained in this work would be different if we used a different value of $D_I C_I^*$. Although work has been done to measure point defect properties at higher temperatures, the extrapolation to lower (TED) temperatures is error prone. Obtaining accurate values for point defect parameters either through experiments or through *ab-initio* calculations is essential.

7.2 Software development

Our work also involved in developing a computer software that is capable of solving the models that we have postulated. To this end, we have developed DOPDEES, a one-dimensional multi-purpose partial differential equation initial value solver. To enable faster technology transfer, we have also developed Process Modeling Modules (PMM) which consists a set of scripts that encapsulate the models that we have developed in a ready to use form.

Although DOPDEES/PMM framework is good for model development/testing, it has limited applicability in a production environment, primarily due to its 1-D nature. One commercial TCAD software vendor (Avant! Corp.) has developed a similar framework (Taurus PMEI) that can be used in 1, 2 and 3 dimensional problems. The models that we implemented under the DOPDEES/PMM framework will be ported to Taurus PMEI framework for wider use within the industry.

Appendix A

Calculation of the Kinetic Precipitation Rate

In this appendix, we derive the kinetic precipitation rate for various precipitate shapes. To this end, we solve the steady state diffusion field around a precipitate, calculating the flux at the interface following the technique used by Dunham [12]. We start with the following definitions:

D: Diffusivity of solute atoms.

k: Surface reaction rate ($k^{-1} = 0$ if the reaction is diffusion limited).

A_n: Surface area of a size n precipitate.

r_n: Radius of the sphere.

R_n: Radius of the disc.

b: Reaction distance (one lattice spacing).

C_n^{int}: Concentration at the surface of a size n precipitate.

C_n^*: Concentration that would be in equilibrium with a size n precipitate.

$\tilde{C}$: $C - C^\infty$.

c^s: Concentration at the surface of a sphere.

Our basic equation is flux in to the surface = amount of material consumed:

$$A_n D \left. \frac{dC}{dr} \right|_{r=\text{surface}} = A_n k (C_n^{\text{int}} - C_n^*) \tag{A.1}$$

We will execute the following steps for each precipitate shape:

1. Write down $\tilde{C}(r)$ as a function of c^s (sum over spheres for using r rather than b).

2. Write down $\tilde{C}_n^{\text{int}}$ as a function of c^s (set $r = r^{\text{int}}$ in the previous step).

3. Take the derivative of $\tilde{C}(r)$ with respect to r and evaluate at the interface.

4. Solve for c^s from step 1 and substitute into above to find R^{eff}.

5. Write down λ_n.

A.1 Spherical defects

1.
$$\tilde{C}(r) = c^s \frac{r_n + b}{r} \tag{A.2}$$

2.
$$\tilde{C}_n^{\text{int}} = c^s \tag{A.3}$$

3.
$$\left. \frac{d\tilde{C}}{dr} \right|_{r=r_n+b} = -\frac{c^s}{r_n + b} \tag{A.4}$$

4.
$$\left. \frac{d\tilde{C}}{dr} \right|_{r=r_n+b} = -\frac{\tilde{C}_n^{\text{int}}}{r_n + b} \qquad \Rightarrow R^{\text{eff}} = r_n + b \tag{A.5}$$

5.
$$D\lambda_n = \frac{A_n}{\frac{R^{\text{eff}}}{D} + k^{-1}} = \frac{DA_n}{R^{\text{eff}} + Dk^{-1}} \tag{A.6}$$

If the system is diffusion limited this reduces to:

$$\lambda_n = \frac{A_n}{R^{\text{eff}}} \tag{A.7}$$

If not we have

$$\Lambda = \frac{D}{k} \Rightarrow \lambda_n = \frac{A_n}{R^{\text{eff}} + \Lambda} \tag{A.8}$$

For the sphere, $A_n = 4\pi(r_n + b)^2$, hence:

$$\lambda_n = \frac{4\pi(r_n + b)^2}{(r_n + b) + \Lambda} \cong 4\pi(r_n + b) \tag{A.9}$$

A.2 Disc-shaped defects:

1.
$$\tilde{C}(r) = c^s \ln(8R_n/r) \tag{A.10}$$

2.
$$\tilde{C}_n^{\text{int}} = c^s \ln(8R_n/b) \tag{A.11}$$

3.
$$\left. \frac{d\tilde{C}}{dr} \right|_{r=b} = -\frac{c^s}{b} \tag{A.12}$$

4.
$$\left. \frac{d\tilde{C}}{dr} \right|_{r=b} = -\frac{C_n^{\text{int}}}{b\ln(8R_n/b)} \qquad \Rightarrow R^{\text{eff}} = b\ln(8R_n/b) \tag{A.13}$$
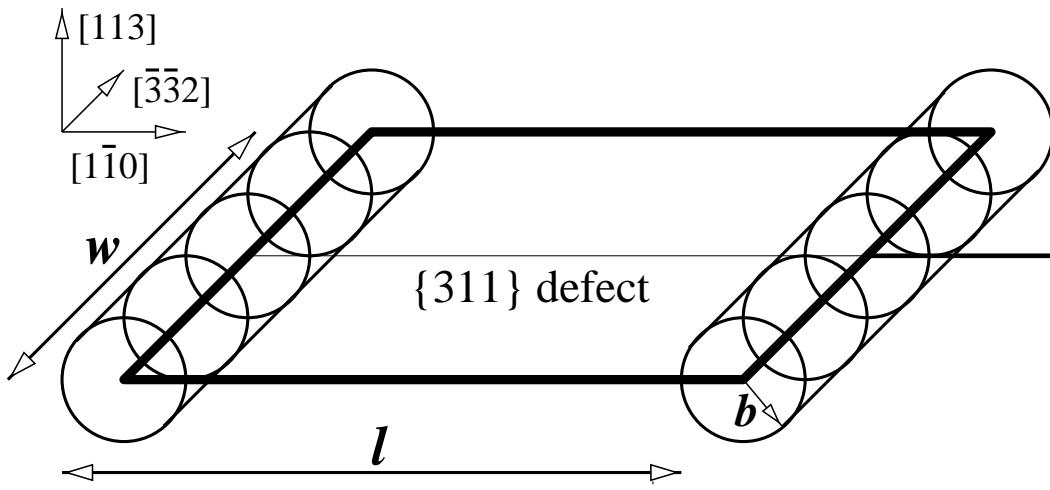
Figure A.1: Division of the capture cross-section of a {311} defect into spheres of equal area.

5.

$$\lambda_n = \frac{A_n}{R^{\text{eff}} + \Lambda} \cong \frac{A_n}{R^{\text{eff}}} \qquad (A.14)$$

For the disc (torus) $A_n = 4\pi^2 R_n b$, so we get:

$$\lambda_n \cong \frac{4\pi^2 R_n}{\ln(8R_n/b)} \qquad (A.15)$$

A.3 {311} defects:

We assume that {311} defects are planar with a rectangular shape and grow primarily in their length.[50] The capture cross-section of a {311} defect is assumed to be cylindrical regions of radius b with half-spheres at each end (Fig. A.1), where b is the silicon lattice spacing. In order to find the diffusion field around a {311} defect, we divided this region into spheres of radius b which have a total surface area equal to that of the sum of the two cylinders and four half-spheres. We then added up the steady-state diffusion fields of these spheres to find the concentration at a distance r along the mid-line of the width of a {311} defect:

1.

$$
\begin{aligned}
\tilde{C}(r) &= 2\sum_{i=1}^{N/2} \frac{c^s b}{\sqrt{r^2 + \left(i\frac{w}{N}\right)^2}} + 2\sum_{i=1}^{N/2} \frac{c^s b}{\sqrt{(l+r)^2 + \left(i\frac{w}{N}\right)^2}} \\
&= 2\int_0^{w/2} \frac{c^s b}{\sqrt{r^2 + y^2}} \frac{N}{w} dy + 2\int_0^{w/2} \frac{c^s b}{\sqrt{(l+r)^2 + y^2}} \frac{N}{w} dy \\
&= 4\int_0^{w/2} \frac{c^s}{\sqrt{r^2 + y^2}} dy + 4\int_0^{w/2} \frac{c^s}{\sqrt{(l+r)^2 + y^2}} dy \\
&= 4c^s \left[\ln\left(\frac{\frac{w}{2} + \sqrt{r^2 + (\frac{w}{2})^2}}{r} \right) + \ln\left(\frac{\frac{w}{2} + \sqrt{(l+r)^2 + (\frac{w}{2})^2}}{l+r} \right) \right]
\end{aligned}
$$

66

2.

$$\tilde{C}_n^{\text{int}} = 4c^s \left[\ln\left(\frac{w}{2} + \sqrt{b^2 + (\frac{w}{2})^2}\right) - \ln(b) + \ln\left(\frac{w}{2} + \sqrt{(l+b)^2 + (\frac{w}{2})^2}\right) - \ln(l+b) \right] \quad \text{(A.17)}$$

3.

$$\left.\frac{d\tilde{C}}{dr}\right|_{r=b} = -2c^s w \left[\frac{1}{b\sqrt{b^2 + (\frac{w}{2})^2}} + \frac{1}{(l+b)\sqrt{(l+b)^2 + (\frac{w}{2})^2}} \right] \quad \text{(A.18)}$$

4.

$$R^{\text{eff}} = \frac{\left[\ln\left(\frac{w}{2} + \sqrt{b^2 + (\frac{w}{2})^2}\right) - \ln(b) + \ln\left(\frac{w}{2} + \sqrt{(l+b)^2 + (\frac{w}{2})^2}\right) - \ln(l+b) \right]}{\frac{w}{2}\left[\frac{1}{b\sqrt{b^2 + (\frac{w}{2})^2}} + \frac{1}{(l+b)\sqrt{(l+b)^2 + (\frac{w}{2})^2}} \right]}$$

$$= \frac{\left[\ln\left(1 + \sqrt{1 + (\frac{2b}{w})^2}\right) - \ln(\frac{2b}{w}) + \ln\left(1 + \sqrt{1 + (\frac{2(l+b)}{w})^2}\right) - \ln(\frac{2(l+b)}{w}) \right]}{\left[\frac{1}{b\sqrt{1 + (\frac{2b}{w})^2}} + \frac{1}{(l+b)\sqrt{1 + (\frac{2(l+b)}{w})^2}} \right]}$$

$$\text{(A.19)}$$

5.

$$\lambda_n = \frac{A_n}{R^{\text{eff}} + \Lambda} \cong \frac{A_n}{R^{\text{eff}}} \quad \text{(A.20)}$$

For the $\{311\}$ defect $A_n = 4\pi bw + 8\pi b^2$, so we get:

$$\lambda_n \cong \frac{4\pi b(w + 2b)}{R^{\text{eff}}} \quad \text{(A.21)}$$

Appendix B

BU Parameter Set

In this section we want to list all the parameters used in this thesis.

```
#----------------------------------------------------------------------
# PMM -- Process Modeling Modules (for DOPDEES and Alamode)
# (c) 1997 Alp H. Gencer                            alp@bu.edu
# $Id: params-BU.tcl,v 1.2 1997/09/16 16:53:44 alp Exp alp $
#----------------------------------------------------------------------
# You may use this software if you own a licence to use DOPDEES or
# Alamode. You must not modify this software in any way. Details of
# license can be found at http://engc.bu.edu/~alp/pmm
#----------------------------------------------------------------------

# Atom concentration in Si
param CSi [unit 5e22 cm-3]
# Lattice spacing of Si
param ASi [expr pow([param CSi],-0.33333)]
param pi4a [expr [param ASi]*4*3.1415927]
# Intrinsic electron concentration in Si
param n_i [func prod [arrhenius 3.9e16 0.605 cm-3] \
[func power $TEMPK 1.5]]
# A minimum concentration for VLSI
param Cmin [unit 1e8 cm-3]

# Dopant charges
param Cnet_coeff_P 1
param Cnet_coeff_As 1
param Cnet_coeff_B -1


#----------------------------------------------------------------------
# Parameters for arsenic.
#----------------------------------------------------------------------

# Solid solubility of As
param Css_As [arrhenius 2.22e22 0.47 cm-3]

# Diffusivity of As
param Diff_0_As [arrhenius  1 4.09 cm2s-1]
param Diff_m_As [arrhenius 19 4.09 cm2s-1]
param Diff_p_As 0
param Diff_d_As 0

# Fractional interstitialcy component
param Fi_0_As 0.3
param Fi_m_As 0.5
param Fi_p_As -100  ; # Irrelevant
param Fi_d_As -100  ; # Irrelevant
```

68

```
# High concentration diffusivity effects for As
param Hcd_pre_As [arrhenius 418 1.96 cm2s-1]
param Hcd_pow_As 4.5

# Coupling with point defects
param Kpair_I_As [arrhenius [expr 1/[param CSi]] -0.3]]
param Kpair_V_As [arrhenius [expr 1/[param CSi]] -1.2]


#-----------------------------------------------------------------------
# Parameters for phosphorus.
#-----------------------------------------------------------------------

# Solid solubility of P
param Css_P [arrhenius 2.9e22 0.45 cm-3]

# Diffusivity of P
param Diff_0_P [arrhenius 1.0 3.58 cm2s-1]
param Diff_m_P [arrhenius 1.0 3.58 cm2s-1]
param Diff_d_P 0
param Diff_p_P 0

# Fractional interstitial component
param Fi_0_P 0.999
param Fi_m_P 0.001
param Fi_d_P -100  ; # Irrelevant
param Fi_p_P -100  ; # Irrelevant

# High concentration diffusivity effects for P
param Hcd_pre_P [arrhenius 3.53e4 1.65]
param Hcd_pow_P 4.5

# Coupling with point defects
param Kpair_I_P [arrhenius [expr 1/[param CSi]] -0.5]
param Kpair_V_P [arrhenius [expr 1/[param CSi]] -1.0]


#-----------------------------------------------------------------------
# Parameters for B
#-----------------------------------------------------------------------

# Solid solubility of B
param Css_B [arrhenius 9.2e22 0.73 cm-3]

# Diffusivity of B
param Diff_0_B [arrhenius 0.30 3.57 cm2s-1]
param Diff_p_B [arrhenius 1.8  3.57 cm2s-1]
param Diff_m_B 0
param Diff_d_B 0

# Fractional interstitialcy component
param Fi_0_B 0.999
param Fi_p_B 0.999
param Fi_m_B -100  ; # Irrelevant
param Fi_d_B -100  ; # Irrelevant

# No high concentration diffusivity effects for B
param Hcd_pre_B   0
param Hcd_pow_B   1

# Coupling with point defects
param Kpair_I_B [arrhenius [expr 1/[param CSi]] -0.5]
param Kpair_V_B [arrhenius [expr 1/[param CSi]] -0.1]


#-----------------------------------------------------------------------
# Parameters for interstitials and vacancies.
#-----------------------------------------------------------------------

# Point defect properties
param DCstar_I_887 [unit 4.70e4 cm-1s-1]
param DCstar_I_E   [unit 4.95 eV]
param DCstar_V_887 [unit 1.05e5 cm-1s-1]
```

```
param DCstar_V_E    [unit 3.80 eV]


# Diffusivities
param Diff_0_I_887 [unit 1.05e-6 cm2s-1]
param Diff_0_I_E    [unit 1.77 eV]
param Diff_0_V_887 [unit 4.6e-6 cm2s-1]
param Diff_0_V_E    [unit 1.8 eV]


# Multiplied DV by 1e4


# Charge state info
param Kchg_m_I [arrhenius 5.68 0.5]
param Kchg_p_I [arrhenius 5.68 0.26]
param Kchg_m_V [arrhenius 5.68 0.145]
param Kchg_p_V [arrhenius 5.68 0.455]


# I-V recombination
param KR_E 0.2; # almost diffusion limited


# Surface recombination length
param Surfrec_I [unit 10 A]
param Surfrec_V [unit 10 A]


#----------------------------------------------------------------------
# Dopant-dopant pairing. Parameters from Wittel.
#----------------------------------------------------------------------


# Which pairs have been defined
set PAIRS {{B P} {B As}}


# Paring coefficients
param Kpair_B_P   [arrhenius [expr 1.0/2.86e26] -1.8 cm-3]
param Kpair_B_As [arrhenius [expr 1.0/2.22e26] -1.8 cm-3]


#----------------------------------------------------------------------
# {311} defect and dislocation loop formation parameter.
#----------------------------------------------------------------------
# Solid solubility of I in 311s for sss model
# Calibrated to Packan's TED data. See Packan-TED.
param Css_311_sss [arrh887 1350 -0.5]


# Solid solubility of I in 311s for analytic model
# Calibrated to Eaglesham's {311} data. See Eaglesham-311.
param Css_311_anl [arrh887 1700 -1.25]
param K311_anl_0  -0.62
param K311_anl_1  0.79
param K311_anl_2  4.39


# Parameters for the 3KPM model (a_i)
param K311_3KPM_0 3.855
param K311_3KPM_1 15.906
param K311_3KPM_0 -1.420


# Minimum concentrations
param MI_0_min [unit 1.00e4 cm-3]
param MI_1_min [unit 2.01e4 cm-3]
param MI_2_min [unit 4.05e4 cm-3]


#----------------------------------------------------------------------
# Interstitial segregation and diffusion in oxide.
# References:
# - Diffusivity from ...
# - segregation coefficient from A. Agarwal (BU).
#----------------------------------------------------------------------


# Diffusivity of I in oxide
param Diff_Ox_I [arrhenius 13 4.5 cm2s-1]


# Segregation coeff.
param Mseg_Ox_Si_I [arrhenius 0.806 2.11]
```

70

Bibliography

[1] A.M. Agarwal and S.T. Dunham. "Consistent quantitative models for the spatial extend of point defect interactions in silicon". *J. Appl. Phys.* **78**, 5313 (1995).

[2] R. Angelucci, F. Cembali, P. Negrini, M. Servidori, and S. Solmi. "Temperature and time dependence of dopant enhanced diffusion in self ion implanted silicon". *J. Electrochem. Soc.* **134**(12), 3130 (1987).

[3] R. Angelucci, P. Negrini, and S. Solmi. "Transient enhanced diffusion of dopants in silicon induced by implantation damage". *Appl. Phys. Lett.* **49**(21), 1468 (1986).

[4] J.P. Biersack and W. Ecstein. *Appl. Phys. A* **34**, 73 (1984).

[5] H. Bracht, N.A. Stolwijk, and H. Mehrer. "Properties of intrinsic point defects in silicon determined by zinc diffusion experiments under non-equilibrium conditions". *Phys. Rev. B* **52**(23), 16542 (1995).

[6] H.S. Chao. "Physics and modeling of ion implantation induced transient enhanced difusion in silicon". Ph.D. thesis, Stanford University (1997).

[7] S. Chaudhry, J. Lui, M.E. Law, and K.S. Jones. "Evolution of dislocation loops in silicon in an inert ambient (Part 2)". *Solid State Electronics* **38**(7), 1313 (1995).

[8] I. Clejan and S.T. Dunham. "A reduced moment based model for precipitation kinetics and application to dopant deactivation in silicon". *J. Appl. Phys.* **78**(12), 7327 (1995).

[9] N.E.B. Cowern, K.T.F. Janssen, and H.F.F. Jos. "Transient diffusion of ion implanted B in Si: Dose, time and matrix dependence of atomic and electrical profiles". *J. Appl. Phys.* **68**(12), 6191 (1990).

[10] N.E.B. Cowern, G.F.A. van de Walle, P.C. Zalm, and D.W.E. Vandenhoudt. "Mechanisms of implant damage annealing and transient enhanced diffusion in Si". *Appl. Phys. Lett.* **65**(23), 2981 (1994).

[11] S.T. Dunham. "A quantitative model for the coupled diffusion of phosphorus and point defects in silicon". *Electrochemical Soc.* **139**, 2628 (1992).

[12] S.T. Dunham. "Growth kinetics of disk-shaped extended defects with constant thickness". *Appl. Phys. Lett.* **63**(4), 464 (1993).

[13] S.T. Dunham. "Modeling of dopant diffusion during annealing of sub-amorphizing implants". In **Materials Synthesis and Processing Using Ion Beams**, Materials Research Soc., (1994).

[14] S.T. Dunham. "Modeling of the kinetics of dopant precipitation in silicon". *J. Electrochem. Soc.* **142**, 2823 (1995).

[15] S.T. Dunham and A.M. Agarwal. "Spatial variations in point defect concentrations and their impact on submicron device structures". In **ULSI Science and Technology**, Electrochemical Soc., 235 (1995).

[16] S.T. Dunham, I. Clejan, and A.H. Gencer. "Accurate and efficient modeling of nucleation and growth processes". *Mat. Sci. Eng. A* **238**(1), 152 (1997).

[17] D.J. Eaglesham, P.A. Stolk, H.J. Gossmann, and J.M. Poate. "Implantation and transient B diffusion in Si: The source of the interstitials". *Appl. Phys. Lett.* **65**(18), 2305 (1994).

[18] P.M. Fahey, P.B. Griffin, and J.D. Plummer. "Point defects and dopant diffusion in silicon". *Reviews of Modern Physics* **61**(2), 289 (1989).

[19] R. Fair. "Point defect charge state effects on transient diffusion of dopants in Si". *J. Electrochem. Soc.* **137**(2), 667 (1990).

[20] A.H. Gencer, S. Chakravarthi, I. Clejan, and S.T. Dunham. "Fundamental modeling of transient enhanced diffusion through extended defect evolution". In **Defects and Diffusion in Silicon Processing**, Materials Research Soc., (1997).

[21] A.H. Gencer, S. Chakravarthi, and S.T. Dunham. "Physical modeling of transient enhanced diffusion and dopant deactivation via extended defect evolution". In **Proceedings of International Conference on Simulation of Semiconductor Processes and Devices (SISPAD)**, IEEE Electron Devices Society, 77 (1997).

[22] A.H. Gencer and S.T. Dunham. "Modeling of dislocation loop growth and transient enhanced diffusion in silicon for amorphizing implants". In **Microstructure Evolution During Irradiation**, Materials Research Soc., (1996).

[23] A.H. Gencer and S.T. Dunham. "Modeling of evolution of {311} defects and prediction of transient enhanced diffusion". In **TECHCON '96 Proceedings**, Semiconductor Research Corporation, (1996).

[24] A.H. Gencer and S.T. Dunham. "Modeling of transient enhanced diffusion based on evolution of {311} defects". In **Process Physics and Modeling in Semiconductor Technology**, Electrochemical Soc., 155 (1996).

[25] A.H. Gencer and S.T. Dunham. "A predictive model for transient enhanced diffusion based on evolution of {311} defects". *J. Appl. Phys.* **81**(2), 631 (1997).

[26] A.H. Gencer and S.T. Dunham. "DOPDEES/PMM: A system for portable model description". In **Proceedings of the First International Conference on Modeling and Simulation of Microsystems, Semiconductors, Sensors and Actuators (MSM)**, (1998).

[27] A.H. Gencer and S.T. Dunham. "Modeling and simulation of transient enhanced diffusion and extended defect kinetics". In **TECHCON '98 Proceedings**, Semiconductor Research Corporation, (1998).

[28] A.H. Gencer and S.T. Dunham. "Moment-based modeling of extended defects for simulation of TED: What level of complexity is necessary?". In **Silicon Front-End Technology-Materials Processing and Modeling**, Materials Research Soc., (1998).

[29] M.D. Giles. "Transient phosphorus diffusion below the amorphization threshold". *J. Electrochem. Soc.* **138**(4), 1160 (1991).

[30] M.D. Giles. "Transient phosphorus diffusion from silicon and argon implantation damage". *Appl. Phys. Lett.* **62**(16), 1940 (1993).

[31] P.B. Griffin, R.F. Lever, P.A. Packan, and J.D. Plummer. "Doping and damage dose dependence of implant induced transient enhanced diffusion below the amorphization threshold". *Appl. Phys. Lett.* **64**(10), 1242 (1994).

[32] R.A. Huang. "Experimental investiagtion and modeling of the effects of high-dose ion implantation damage on boron diffusion in silicon". Ph.D. thesis, Stanford University (1994).

[33] K.S. Jones, J. Lui, L. Zhang, V. Krishnamoorthy, and R.T. DeHoff. "Studies of the interactions between {311} defects and type I and II dislocation loops in Si implanted silicon". *Nuc. Inst. and Meth. B* **106**, 227 (1995).

[34] H. Kinoshita, G.Q. Lo, and D.L. Kwong. "Diffusion modelling of ion implanted boron in Si during rta: correlation of extended defect formation and annealing with the enhanced diffusion of boron". *J. Electrochem. Soc.* **140**(1), 248 (1993).

[35] J. Lui, M.E. Law, and K.S. Jones. "Evolution of dislocation loops in silicon in an inert ambient (Part 1)". *Solid State Electronics* **38**(7), 1305 (1995).

[36] M. Miyake and S. Aoyama. "Transient enhanced diffusion of ion implanted boron in Si during rapid thermal annealing". *J. Appl. Phys.* **63**(5), 1754 (1988).

[37] B.J. Mulvaney, W.B. Richardson, and T.L. Crandle. *IEEE Trans. Comp. Aided Des.* **8**, 336 (1989).

[38] J.K. Osterhout. *Tcl and the Tk toolkit*. Addison Wesley (1994). ISBN 0–201–63337–X.

[39] P.A. Packan. "Physical modeling of transient diffusion effects in silicon due to surface oxidation and ion-implantation". Ph.D. thesis, Stanford University (1991).

[40] P.A. Packan and J.D. Plummer. "Transient diffusion of low-concentration B in Si due to ^{29}Si implantation damage". *Appl. Phys. Lett.* **56**(18), 1787 (1990).

[41] G.Z. Pan and K.N. Tu. "Transmission electron microscopy on {113} rodlike defects and {111} dislocation loops in silicon-implanted silicon". *J. Appl. Phys.* **82**(2), 601 (1997).

[42] G.Z. Pan, K.N. Tu, and S. Prussin. "Size distribution of end-of-rage dislocation loops in silicon-implanted silicon". *Appl. Phys. Lett.* **68**(12), 1654 (1996).

[43] A. Parisini and A. Bourret. "Diamond hexagonal silicon phase and {311} defects: Energy calculations and new defect models". *Phil. Mag. A* **67**(3), 605 (1993).

[44] H. Park and M. Law. "Effects of low dose Si implantation damage on diffusion of phosphorus and arsenic in Si". *Appl. Phys. Lett.* **58**(7), 732 (1991).

[45] H. Park and M. Law. "Point defect based modelling of low dose silicon implant damage and oxidation effects on phosphorus and boron diffusion in silicon". *J. Appl. Phys.* **72**(8), 3431 (1992).

[46] J.M. Poate, D.J. Eaglesham, and G.H. Gilmer. "Ion implantation and transient enhanced diffusion". In **IEDM Technical Digest**, IEEE, 77 (1995).

[47] S. Prussin, G.Z. Pan, and P.F. Zhang. "Role of dose, dose rate and anneal temperature on end-of-range dislocation loops". In **Electrochemical Soc. Proceedings**, Electrochemical Soc., 379 (1996).

[48] C.S. Rafferty, G.H. Gilmer, M. Jaraiz, D. Eaglesham, and H.J. Gossmann. "Simualtion of cluster evaporation and transient enhanced diffusion in silicon". *Appl. Phys. Lett.* **68**, 2395 (1996).

[49] M. Servidori, R. Angelucci, F. Cembali, P. Negrini, S. Solmi, P. Zaumsteil, and U. Winter. "Retarded and enhanced dopant diffusion in silicon related implantation induced excess vacancies and interstitials". *J. Appl. Phys.* **61**(5), 1834 (1987).

[50] S. Takeda, M. Kohyama, and K. Ibe. "Interstitial defects on {311} in Si and Ge: line defect configuration incorporated with a self interstitial atom chain". *Phil. Mag. A* **70**(2), 28 (1994).

[51] Al Tasch. *UT-Marlowe User's Manual*. University of Texas at Austin version 4.1 edition (1997).

[52] R.H. Thompson, V. Krishnamoorthy, J. Lui, and K.S. Jones. "Type II dislocation loops and their effect on strain in ion implanted silicon as studied by high resolution x-ray diffraction". In **Proc. of MRS Meeting**, Materials Research Soc., 378 (1995).

[53] O. Vancauwenberghe, N. Herbots, and O. Hellman. *J. Vac. Sci. Tech. B* **9**, 2027 (1991).

[54] B.B. Welch. *Practical programming in Tcl and Tk*. Prentice Hall (1995). ISBN 0–13–182007–9.

[55] D. Yergeau. *Alamode — A Layared Modeling Environment* (1996).

[56] D. Yergeau, R. Dutton, A.H. Gencer, and S.T Dunham. "A model implementation environment to support rapid prototyping of new TCAD models: A case study for dopant diffusion". Technical report SEMATECH (1997).

[57] L.H. Zhang and K.S. Jones. "Transient enhanced diffusion without {311} defects in low energy B implanted silicon". *Appl. Phys. Lett.* (1995). in press.

[58] H. Zimmermann and H. Ryssel. "Gold and platinum diffusion: The key to the understanding of point defect behavior in silicon". *Applied Physics A* **55**, 121 (1992).

CURRICULUM VITAE

EDUCATION

- **Ph.D. in Electrical Engineering**   **1999**
  Boston University, Department of Electrical and Computer Engineering, Boston, MA.

- **Master of Science in Electrical Engineering**   **1995**
  Boston University, Department of Electrical, Computer and Systems Engineering, Boston, MA.
  GPA: 4.00/4.00.

- **Bachelor of Science in Electrical Engineering**   **1993**
  Boğaziçi University, Department of Electrical and Electronics Engineering, Istanbul, Turkey.
  GPA: 3.92/4.00 (High Honors).

- **Bachelor of Science in Physics**   **1993**
  Boğaziçi University, Department of Physics, Istanbul, Turkey. GPA: 3.92/4.00 (High Honors).

- **Abitur**   **1989**
  German High School, Istanbul, Turkey.

EXPERIENCE

- **Avant! Corporation,** Lincoln, MA   **1998–present**
  Applications Engineer at the TCAD Business Unit.

- **Boston University,** Boston, MA   **1994–1998**
  Research Assistant for Assoc. Prof. Scott Dunham in the Department of Electrical and Computer Engineering.

- **Boston University,** Boston, MA   **1993–1994**
  Teaching assistant for Prof. T.D. Moustakas in the Department of Electrical and Computer Engineering.

- **Konda Research Inc.,** Istanbul, Turkey   **1991–1993**
  IT consultant and application developer (part-time).

- **Siemens AG,** Munich, Germany   **1991**
  Summer Intern at the Department of Corporate Research and Development.